Effects of Phase Composition and Microstructure on the Dielectric Strength of Thermally Sprayed Alumina Layer in Coating-Based Resistive Heating Systems

Morvarid Mohammadian Bajgiran

A Thesis
In the Department
Of
Mechanical, Industrial and Aerospace Engineering

Montréal, Québec, Canada

Presented in Partial Fulfillment of the Requirements
For the Degree of
Master of Applied Science (Mechanical Engineering) at
Concordia University
Montréal, Québec, Canada

CONCORDIA UNIVERSITY

School of Graduate Studies

This is to certify that the thesis prepared

By: Morvarid Mohammadian Bajgiran

Entitled: Effects of Phase Composition and Microstructure on the Dielectric Strength of Thermally Sprayed Alumina Layer in Coating-Based Resistive Heating Systems

And submitted in partial fulfilment of the requirements for the degree of

Master of Applied Science (Mechanical Engineering)

Complies with the regulations of the University and meets the accepted standards with respect to originality and quality.

Signed by the final Examining Committee:

_____ Chair

Dr. Ali Dolatabadi

_____ Internal Examiner

Dr. Ali Dolatabadi

_____ External Examiner

Dr. Sana Jahanshahi Anbuhi

_____ Thesis Co-Supervisor

Dr. Christian Moreau

_____ Thesis Co-Supervisor

Dr. André McDonald

Approved by: _____

Dr. Mamoun Medraj, Graduate Program Director

September 1, 2020 _____

Dr. Mourad Debbabi

Dean of Gina Cody School of Engineering & Computer Science

Abstract

Effects of Phase Composition and Microstructure on the Dielectric Strength of Thermally Sprayed Alumina Layer in Coating-Based Resistive Heating Systems

Morvarid Mohammadian Bajgiran

Concordia University, 2020

Heated surfaces are required in many applications ranging from home scientific equipment to home appliances. Conventional heating solutions mainly include utilization of coiled wire elements that are typically installed in the vicinity of the surfaces that require heating. However, based on the physical location and geometry of these conventional heating elements, they have limited performance and cannot achieve their maximum efficiency. Utilizing thermal spraying techniques is a possible approach that can circumvent some of the shortcomings of previous heating systems. Electrical heating elements can be directly deposited on surfaces as a possible way to overcome geometric limitations and minimize air gaps and thermal contact resistance between the heating system and the surface to be heated.

This thesis investigated the microstructure of various heating systems fabricated by using several thermal spraying techniques, namely, suspension plasma spraying (SPS), flame spraying (FS), high velocity oxy-fuel (HVOF), and air plasma spraying (APS). SPS and FS techniques were utilized to deposit alumina as an intermediary dielectric layer in metal-alumina composite heating element coatings. HVOF and APS processes were used for the fabrication of a nickel-20chromium (Ni-20Cr) metal heating element layer. The resultant microstructure and phase composition of the

alumina layers were evaluated by using scanning electron microscope images (SEM), Raman spectroscopy, and X-ray diffraction (XRD) analysis. Dielectric breakdown voltage tests were conducted on selected heating systems and the performance of the alumina layer individually and within the heating system was examined.

The advantages and disadvantages of using each of the thermal spraying processes and the impact of various spraying parameters on the microstructure of the developed systems were studied. In the FS-sprayed alumina, large pores were detected that were randomly distributed in the coatings which led to the penetration of the top heating element layer. Partial melting of the alumina powder particles was observed in the FS alumina samples that led to formation of two different alumina phases in each particle. Dense, cauliflower-like, and porous structures were seen in SPS-sprayed alumina coatings that consequently, resulted in various proportions of the alumina phases in each coating.

It was found that microstructural and phase content characteristics are both influential components in determining the dielectric properties of the sprayed alumina coatings. Dielectric strength of single layered samples (only alumina) was much higher compared to multi-layered samples. The results suggest that the types of alumina phases present in the coatings and microstructural features such as air gaps and interconnected cracks can negatively affect the final electrical properties of the alumina layer in the heating system.

List of Publications and Conference Contributions

1. M. Mohammadian Bajgiran, M. Rezvani Rad, A. McDonald, C. Moreau, "Effects of Phase Composition and Microstructure on the Breakdown Voltage of Thermally Sprayed Alumina Layers in Coating-Based Resistive Heating Systems", *Journal of European Ceramic Society*, Under Review, 2020
2. M. Rezvani Rad, M. Mohammadian Bajgiran, C. Moreau, A. McDonald, "Fabrication of thermally sprayed coating systems for mitigation of ice accumulation in carbon steel pipes and prevention of pipe bursting", *Surface and Coatings Technology*, (2020): 126013.
3. M. Rezvani Rad, M. Mohammadian Bajgiran, C. Moreau, A. McDonald, "Microstructural and performance analyses of thermal-sprayed electric resistance heating systems deposited onto steel pipes as de-icing elements", in: International Thermal Spray Conference, May 26-29, 2019 (Yokohama, Japan), ASM International, (2019), # 47189, 6 pages on compact disk.
4. Morvarid Mohammadian Bajgiran, Milad Rezvani Rad, André McDonald, Christian Moreau, "On Reliability of Thermally-Sprayed Alumina Dielectric Layers in a Multi-layered Coating-based Heating System", in: Proceedings of the Joint Canadian Society for Mechanical Engineering and CFD Society of Canada International Congress 2019, June 2-5, 2019 (London, ON, Canada), The Canadian Society for Mechanical Engineering, (2019), 8 pages on compact disk.

Acknowledgment

First and foremost, I would like to express my sincere gratitude to my supervisors, Dr. Christian Moreau and Dr. André McDonald for believing in me and for giving me the opportunity to be a part of their research group. I am grateful for their continuous support and encouragement during the course of my master's program. I have immensely learned from not only their invaluable scientific input and academic advice, but also from their aspiring life lessons, creativity, compassion and commitment. It has been a great privilege to work with them and to learn from them. I wish to thank Dr. Milad Rezvani Rad, my great colleague, who acted as an equal supervisor for me. He always helped me through difficulties of the research and we managed to have a great teamwork experience even though we were students of two different universities.

I am grateful to Dr. Fadhel Ben Ettouil for his tireless technical support, invaluable advice, and guidance through every single step of the experimental work. I would like to thank him for always being available to answer my most basic questions with patience. I would like to thank Dr. Ali Dolatabadi for his constant encouragement and support in celebrating every success or even small achievements. I would like to thank Dr. Jean-Michel Lamarre for his assistance and guidance regarding electrical testing of the coating systems.

I wish to thank my great friends at Concordia University and the entire Thermal Spray Laboratory group members for the great teamwork and their priceless friendship. Special thanks to Armin, Hediyeh, Navid, Alexandre, Hafez, Elnaz, Behrad, Nima, Masiar, Fabian, for helping me throughout my master's program.

I extend my appreciation to Natural Sciences and Engineering Research Council of Canada (NSERC) Green Surface Engineering for Advanced Manufacturing (Green-SEAM) Network for

the financial support and for providing a great platform to showcase our research work and to connect with many industries and universities from around the world.

Last, but certainly not the least, my most heartfelt thanks goes to my parents, Mahtab and Farrokh, my sister Mojgan, my brothers Amir, Hamid, Farshad, and Fariborz for supporting me with their unconditional love and for beliving in me every single step of my journey. I am very lucky to be part of this great family. This accomplishment would not have been possible without their ever-lasting support and invaluable care.

Table of Contents

List of Figures

List of Tables

List of Abbreviations

Abbreviation	*Meaning*
APS	Atmospheric Plasma Spray
ACBD	Alternating Current Breakdown
BDS	Breakdown Dielectric Strength
CLSM	Confocal Laser Scanning Microscopy
CS	Cold Spray
CVD	Chemical Vapor Deposition
DBV	Dielectric Breakdown Voltage
D-Gun	Detonation Gun
DS	Dielectric Strength
EDX	Energy-Dispersive X-ray Spectroscopy
FESEM	Field Emission Scanning Electron Microscopy
FRPC	Fiber-Reinforced Polymer Composite
FS	Flame Spray

HVAF	High Velocity Air-Fuel
HVOF	High-Velocity Oxygen Fuel
HVSFS	High-Velocity Suspension Flame Spraying
PTA	Plasma Transferred Arc
SD	Standard Deviation
SEM	Scanning Electron Microscopy

List of Symbols

Symbol	Meaning
D_{10}	10% of particles are smaller or equal to this particles size
D_{50}	50% of particles are smaller or equal to this particles size
D_{90}	90% of particles are smaller or equal to this particles size
ε_r	Dielectric constant
ρ	Electrical (volume) resistivity
λ	Wavelength
$\tan \delta$	Dissipation Factor
α-Al_2O_3	Corundum/ Alpha-alumina
γ–Al_2O_3	Gamma-alumina

Chapter 1. Introduction

1.1. Background and Motivation

Over the past century, thermal spraying has been greatly refined and optimized to serve as an approach to design and modify the surface properties and characteristics of components. Thermal spraying, as demonstrated in Fig. 1-1, is generally defined as a deposition process in which an energy source is used to heat the initial feedstock material (which can be in the form of suspension, powder, wire, or rod) to form molten droplets , which are accelerated towards the substrate by using a gas stream or compressed air depending on the thermal spray process being used [1, 2]. One of the main advantages of thermal spraying is its flexibility in the choice of materials. To satisfy the needs of certain fields and applications and by considering the intrinsic properties of each material, proper materials can be determined for the manufacturing process. In fact, it is mentioned in another general definition for thermal spraying processes by R. Tucker [3] that any material which is capable of melting without going through chemical oxidation and decomposition is suitable to be used in thermal spraying.

The interaction between a component and its surrounding environment plays a crucial role in determining its lifetime, performance, and efficiency. The surface of the component is where any possible interaction takes place and requires further protection. For instance, offshore

structures face corrosive environments in which the combination of salt and humidity damages the structure's surface and in some more severe cases weakens the whole structure [4]. As another example, unprotected components in turbine blades when exposed to high-temperature conditions would get severely damaged or have their properties changed to an extent where it will no longer satisfy the expected demands [5]. One successful strategy is to cover the surface of these components with a relatively thin layer of material (when compared to the dimensions of the bulk material) that has the necessary properties to face the expected environmental condition [6]. Following the examples above, corrosion-resistant zinc and zinc-aluminum are used to coat offshore structures [7], and yttria-stabilized zirconia (YSZ), with low thermal conductivity and good mechanical properties is commonly used to protect the surface of turbine blades [8].

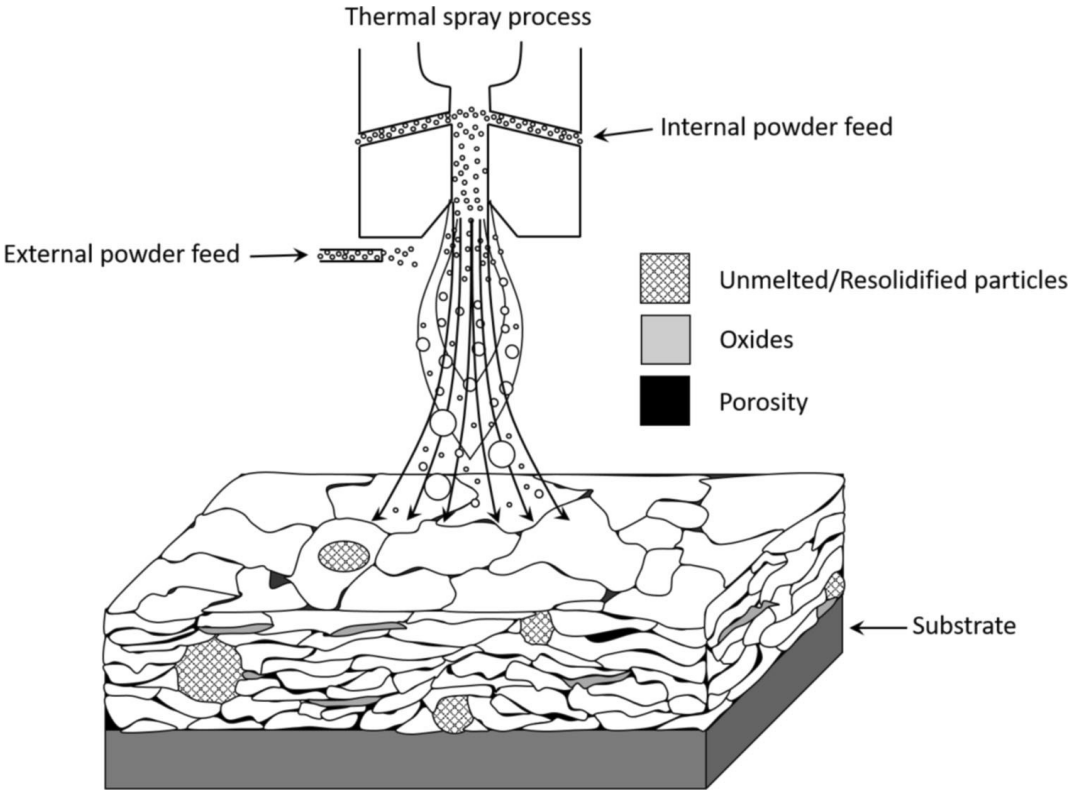

Figure 1-1 Schematic view of a thermal spray process. The powder feeding could be conducted by either radial or axial injection [9].

The emergence of coatings and the advantages of combining the bulk properties of a substrate material with additional benefits of another material on the surface, eliminated limitations of individual materials and gave rise to broader design possibilities in many cutting-edge fields. Thermal spraying is commonly used to protect against numerous surface degradation mechanisms, including wear and erosion [10], corrosion and oxidation [11], high temperatures [12], and in biomedical applications [13], as electronics [14], and as abradable coatings [15]. To date, the potential range for thermally sprayed coatings is expanded which is mainly followed by the recent equipment and process developments.

Thermal spray coatings with an additional functionality beyond their classical properties (i.e., decoration and protection), are of great interest due to the possibilities opened for many applications [16]. Depending on the actual application of the coated substrate, this additional functionality can vary. Conventional examples of functional coatings are self-cleaning, antistatic, anti-reflective and anti-bacterial coatings, while properties like durability, reproducibility, easy application and cost effectiveness, and environmental friendliness are typically expected from conventional coatings [17].

Heated surfaces are being used in many processes and systems. Coiled wire elements are the conventional heating solutions which are generally being used in routine domestic and commercial applications [18]. However, these electrical elements have limited effectiveness due to (1) the air gap and/or a high insulator thickness between the to-be-heated surface and the heater which limits the heat transfer response time and efficiency (2) certain geometries are hard to achieve in space-limited applications or where miniaturization is needed [19]. One possible solution to these problems is to use thermally spray resistive heating elements directly on the surface to be heated (from now on known as the substrate) to try to overcome the above-mentioned

limitations as much as possible. Direct deposition of the heating system maximizes the heat transfer by minimizing the presence of air gap between the layers. In addition, this process is much faster and can adapt to any randomly shaped surfaces [20].

As represented in Fig. 1-2, the electrical conductivity of the substrate determines the configuration of the heating system. Direct deposition of the coating heating element on a non-conductive substrate has been reported [21], but, for cases in which the substrate is electrically conductive, direct deposition of the heating element onto the substrate is not suitable because it leads to short circuit between the heating element and the conductive substrate. Therefore, an intermediary layer with dielectric properties is required to prevent such undesirable phenomenon, while still allowing for heat transfer through the layers. In this regard, alumina is widely used as an electrical insulator in heating systems thanks to its dielectric properties [22].

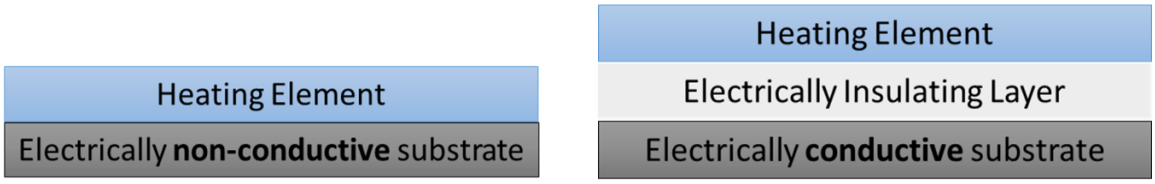

Figure 1-2 Schematic of two different types of coating-based heating systems.

1.2. Electric Resistance Heating Systems

Electric resistance heating systems generate heat based on Joule heating, also known as ohmic or resistive heating. Joule heating is defined as the heat produced in an electrical conductor as a result of the passing of electrical current [23]. When an electric current flows through a conductive material, the material exhibits resistance towards the current which leads to energy dissipation in the form of heat. This phenomenon is a controllable way to produce heat and can be

used in a large scale [24]. Nowadays, electric resistance heating systems are widely being used in industrial and domestic sectors. As an example, electric heating systems that are based on conventional heat tracers has been suggested as an efficient approach to control the temperature in water and high viscosity fluid distribution pipes. Heat tracers protect pipelines against freezing conditions in cases where process steam and waste heat are not accessible [25]. As compared to low-pressure steam system, electric heat tracing method provides a cleaner heat source when applied in large scale and it can control temperature more precisely [24, 26].

Electric resistance heating systems are also used for de-icing of structures such as power transmission and distribution lines during ice storms where ice can reach thicknesses of many tens of millimeters [27]. They can be used as a novel and environmentally friendly technique to deice and melt snow and prevent many traffic accidents and personal injuries caused by ice formation on roads [28]. Wind turbines when in operation may face severe icing that can bring about energy losses, safety threats and mechanical and electrical failures [29]. Resistance heating is proposed as one of the ways to mitigate or prevent ice formation on wind turbines and can provide a more efficient energy distribution on the blade compared to hot air system [30].

Thermal-sprayed coatings as resistive heating systems have been proposed as an alternative to the conventional resistive heaters in recent times and have attracted considerable interest in the recent years. Development of thermal sprayed coatings for heating applications has received an increasing attention in the recent years. A growing body of literature regarding the fabrication of such heating systems has been documented, starting more than two decades ago with the work done by Younis, *et al.* [31] and has been extensively studied during the past decade for various applications, materials and geometries [19–21, 32–34].

1.3. Thermal Spray Processes for Electric Heating System Fabrication

Over the past two decades, thermal spraying has been proposed as an alternative approach to produce electric resistance heating systems directly onto the to-be-heated surface. Thermal spray provides an elegant way to circumvent difficulties caused by conventional heating solutions such as the air gap and/or high insulator thickness between the to-be-heated material and the heater and the fact that they are limited to certain shapes and sizes [19]. Among many methods of surface engineering, thermal spray processes are known to be cost-effective, versatile, and efficient.

Thermal spray encompasses several film deposition techniques in which a high-temperature, high-velocity gas or plasma stream is used to melt and accelerate the feedstock materials toward a substrate leading to formation of thin splats on the substrate [11]. The feedstock is typically in powder, wire, or rod form. Upon deposition, the splats undergo extremely high cooling rates of around 10^6 K/s [35]. The desired coating thickness is obtained by successive impact of the molten or semi-molten droplets on the surface of the substrate. Numerous process parameters affect the coating deposition, surface morphology, resultant microstructure, and characteristics [36]. Different subclasses of thermal spray processes include flame spray (FS), plasma spray, wire-arc spray, high velocity oxy-fuel (HVOF), and cold spray. A comparison between gas temperature and velocity range in different thermal spray techniques is shown in Fig. 1-3.

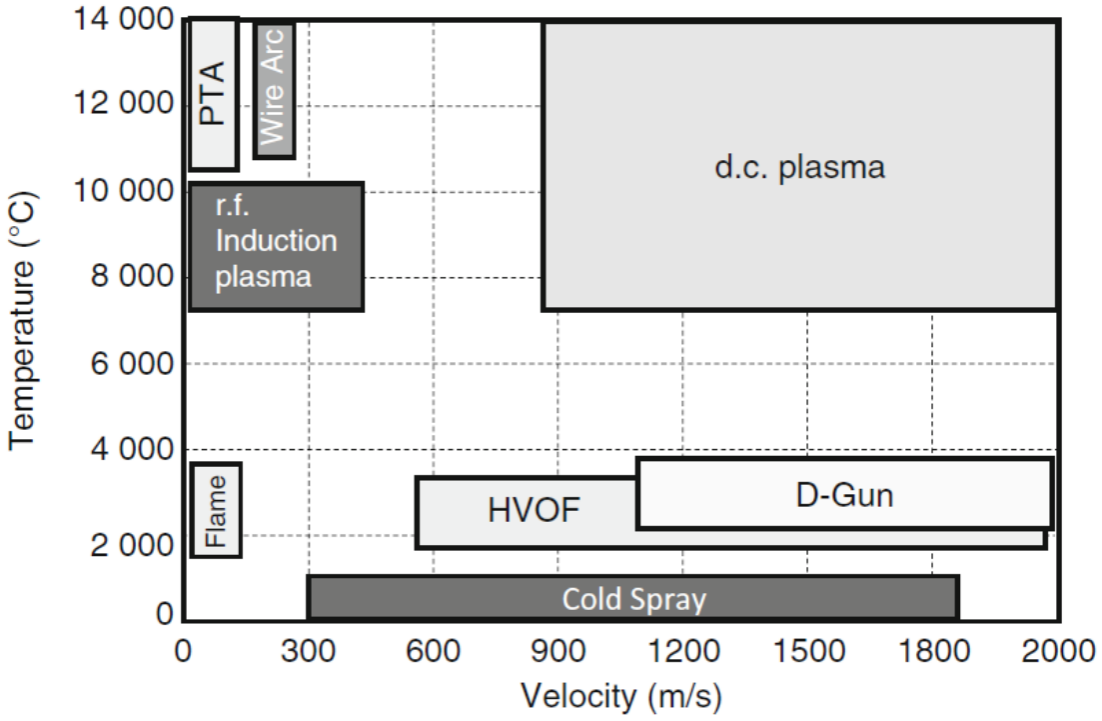

Figure 1-3 Gas temperatures and velocities obtained with different thermal spray techniques [37].

Atmospheric plasma spraying (APS), is one of the most important and widely used types of thermal spraying. One of the main advantages of APS is its versatility as a wide variety of materials can be deposited on different substrate materials [167]. Also, when compared to other surface modifications processes, APS is relatively cost efficient which has made it a great candidate to produce functional coatings in the industry [163, 168]. Moreover, the APS process exhibits limited impact on the substrate after deposition which is due to its low heat input when in application [169]. The APS powder feedstock size ranges from a few tens to a few hundreds of micrometers. Using APS to spray particles smaller than 10 µm may cause difficulties such as clogging and limitations in terms of fine particles penetration into the high-speed plasma jet [174]. Suspension plasma spraying (SPS), is a relatively new spraying technique that allows the

deposition of submicron and nano-scaled materials in the form of a suspension. A schematic of the SPS process is shown in Fig. 1-4.

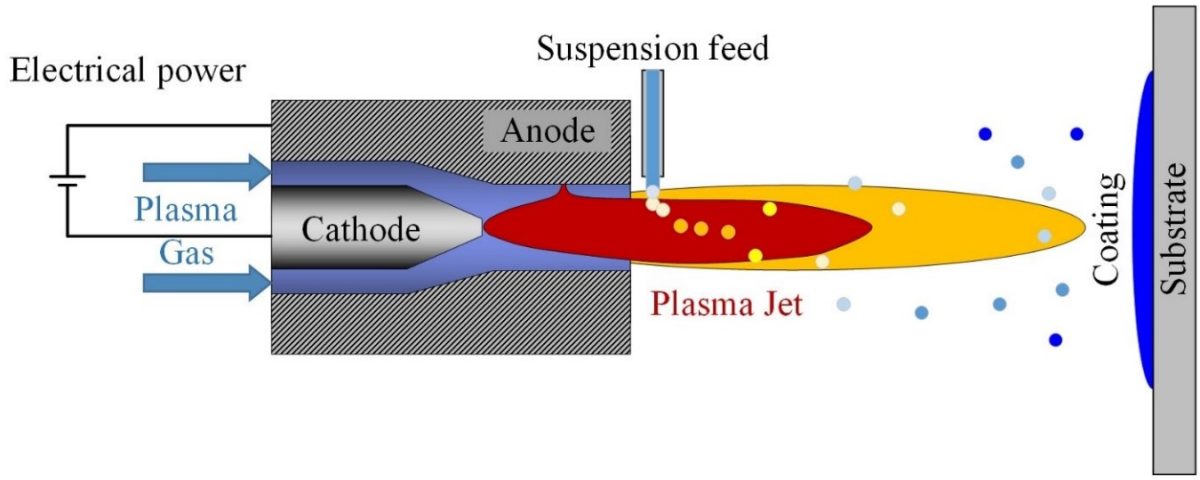

Figure 1-4 A schematic of suspension plasma spray technique [38].

The SPS spray system is the same as the one employed in the APS process. However, the powder carrier used in SPS is a liquid phase (mostly ethanol, water, or mixture of both), instead of air which makes the deposition of submicron-sized particles possible. Fine particles tend to agglomerate and sediment in the liquid carrier; therefore, to overcome this problem, it is suggested to add an appropriate dispersing agent to help stabilize the suspension [39]. As shown in Fig. 1-5, the suspension undergoes one or multiple breakup and atomization phases after being injected into the plasma plume and creates aggregates of powder. Depending on the spraying parameters these fine particles, fully or partially melt and impact onto the substrate [40].

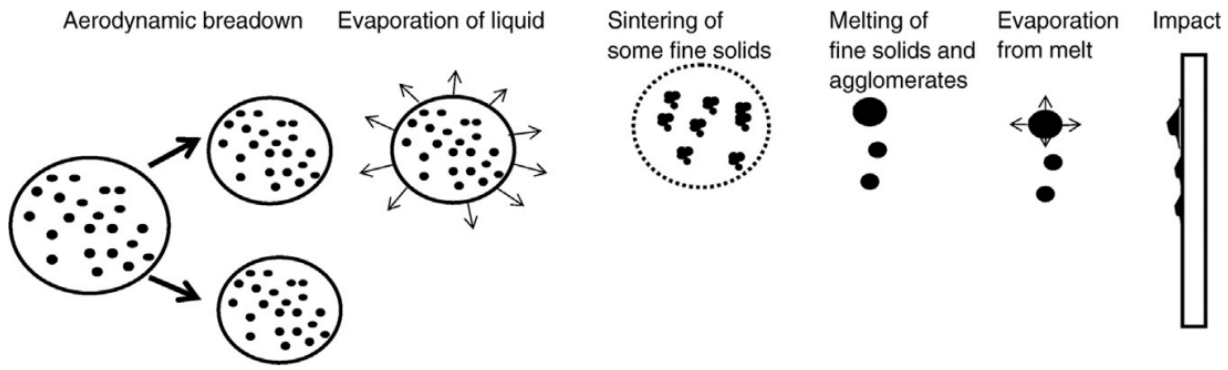

Figure 1-5 Transformation of suspension droplet during spraying [41].

A wide variety of microstructures and coatings can be produced by using both APS and SPS processes. It has been reported in several studies that up to nearly fifty different parameters control the plasma spraying processes and each set of parameters can result in a unique microstructure [36, 39, 40]. One main feature proposed by the SPS process is the likelihood of creating columnar structures. VanEvery, *et al.* [42] first proposed an explanation for formation of these specific structures during the SPS process. It was reported that the plasma drag forces control the droplet inertia of powder particles that are relatively small. Then, drag forces trigger the generation of another velocity component that is along the surface of the substrate in addition to the velocity component that is perpendicular to the substrate surface.

Additionally, columns develop when the peaks of the asperities on the substrate block the path of the oblique droplet trajectories near the substrate surface and prevent them from reaching the valleys downstream of the asperities during spreading. It has been repeatedly reported that SPS-sprayed columnar structures, similar to coatings produced by electron beam physical vapor deposition (EB-PVD), are more strain tolerant compared to other types of microstructures [43,44]. Furthermore, it was found that the microstructure types vary depending on the size of the impacting

particle ranging from planar (same as APS) to columnar [42]. Figure 1-6 schematically shows different acquired microstructures as the particle size reduces.

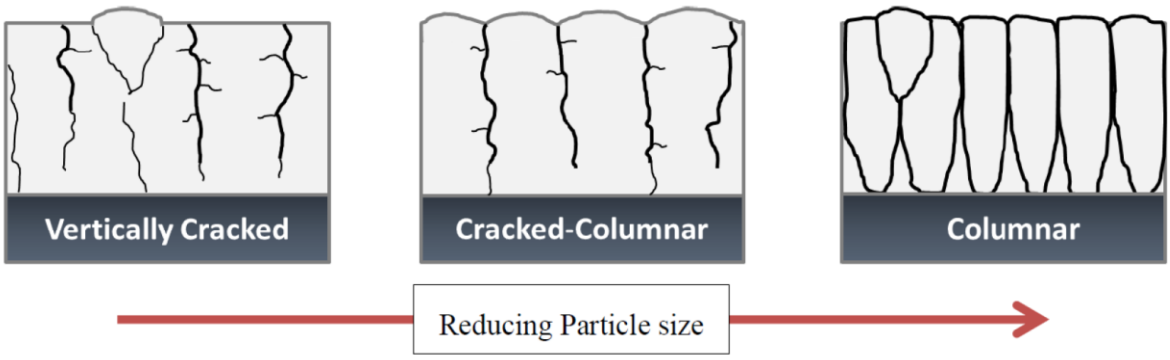

Figure 1-6 Change of microstructure with particle size reduction [45].

Flame spraying (FS) is known to be one of the first and most cost-effective thermal spraying techniques in which a high temperature flame is used to melt the powder feedstock by means of the chemical energy generated from combustion of the fuel gas in oxygen [44, 45]. At the same time, an expanding gas flow is produced in combination with additional gases that creates the required jet applied to accelerate the materials towards the substrate. In the FS process, oxygen and fuel enter the torch axially, generating a combustion flame. The coating material (in the form of powder, wire or rod) by using a carrier gas is introduced into the combustion flame [48]. A schematic of the flame spraying technique in shown in Fig. 1-7. To improve the initial design of flame spraying, several variations have been developed to incorporate different flame temperatures and particle velocities such as detonation gun (D-Gun) spraying, high velocity oxy-fuel (HVOF) spraying, high velocity air-fuel (HVAF) spraying, and suspension/solution high-velocity oxy-fuel spraying [6].

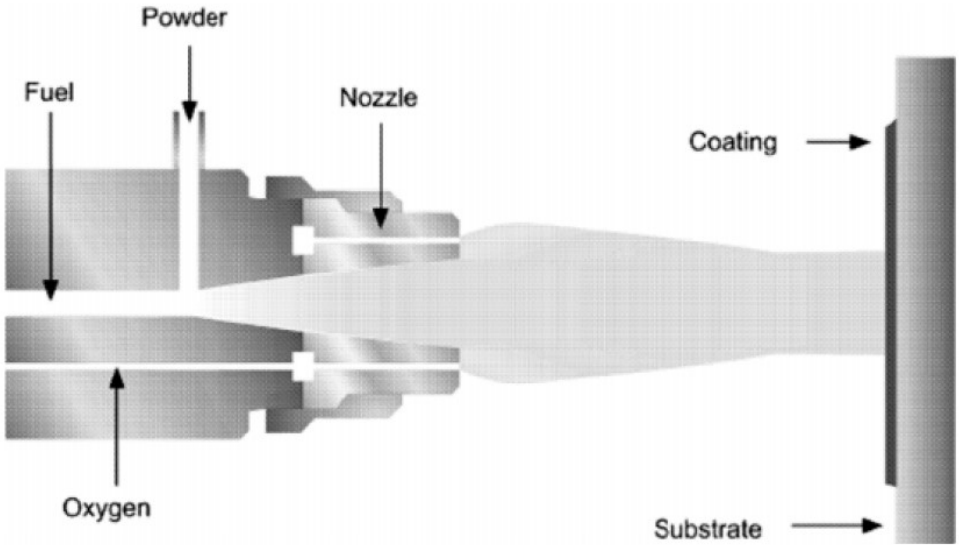

Figure 1-7 A schematic of flame spray technique [48].

High velocity oxy-fuel (HVOF), also known as one of the improved versions of the flame spraying process, was first introduced at the beginning of 1980s. HVOF process, compared to APS process, is capable of depositing a low-oxide content coating at higher particle velocity and relatively lower temperature [1, 44, 47]. Like FS process, in a HVOF process, a mixture of oxygen and fuel is introduced into a combustion chamber. Then the mixture goes through ignition followed by combustion. Fuel can be either in the form of gas or liquid such as hydrogen, propylene, propane, acetylene, kerosene, etc. The exhausted gas is then accelerated in a converging-diverging nozzle and is introduced into the atmosphere at a supersonic velocity ranging from 500 to 1200 m/s. The pressure in the combustion chamber (typically 0.3 to 1) determines the final gas velocity [1, 44]. Powder feedstock used in the HVOF process is normally between 5 to 45 μm which can be injected into the gas either radially or axially by means of a carrier gas (typically nitrogen or argon). High density and high adhesion strength are main characteristics of a HVOF-sprayed coating [1].

1.4. Pipes Failure Due to Ice Accumulation

Freezing and bursting of fluid transport pipes is a pervasive phenomenon that brings about serious and costly damage to the environment. Bulging and rupture of pipes has been observed in systems that are exposed to temperatures below the freezing point of the enclosed liquid. It was reported that the failure occurs where water is entrapped between plugs of ice [50]. Internal pressurization due to ice accumulation was found to be not only restricted to metallic pipes and it has also been seen in plastic piping systems [51]. Over the last decade, $450 million/year damage cost was estimated only in the United States due to damages that stemmed from frozen pipes [52].

As stated by the Insurance Information Institute (I.I.I.) [53], freezing of enclosed liquid in pipes is one of the main problems that happen during winter. Financial losses are not the only detrimental effects caused by frozen pipes. The well-being of the workers in the field are also at risk as the pressurized pipes can in some cases result in explosive ruptures [54]. Given the severity and prevalence of the damage caused by freezing of pipes, an efficient heating system is required to mitigate or prevent the ice accumulation and to protect the piping systems appropriately when exposed to frigid environments. It should be noted that ice formation in water pipes imposes severe elastic and plastic deformation to the pipe structure during application. Hence, the developed heating systems are prone to mechanical failures such as delamination and cracking. In metallic pipes, the heating layer and the dielectric layer need to get mechanically and physically optimized to keep the risk of any type of failure in the piping systems as low as possible.

1.5. Objectives

Despite extensive research conducted in thermal spraying of alumina and its dielectric nature, the obtained results were mainly limited to the performance of single-layered alumina coatings. Limited research has been done on the microstructural characteristics and phase composition of alumina coatings used as insulating layers within coating-based heating systems. That said, the overarching objective of this study is to assess the influence of microstructural characteristics, phase composition, and the deposition of a second metallic layer on the dielectric strength of alumina as an intermediary layer. The sub-objectives of this study were to:

(1) fabricate the alumina samples by two thermal spraying processes, namely, flame spraying and suspension plasma spraying. Flame spraying is considered a low-cost, flexible technique that can potentially be used on site. Suspension plasma spraying has the advantage of fabricating coatings with different microstructures such as dense, porous, and columnar. The columnar structure was specifically of interest since it has been frequently reported in the literature as a more strain tolerant microstructure. This characteristic is of interest as it can be a beneficial feature for alumina layers that are exposed to internal pressurization when applied on water pipes.

(2) study and compare the microstructure of the top heating element deposited by air plasma spraying (APS) and high velocity oxy-fuel (HVOF) processes and to assess the influence of the heating element layer on the mechanical and electrical reliability of the dielectric alumina layer.

(3) study the phase composition of specific regions of the alumina coatings and better understand the phase transformation of the initial alumina powder after deposition by performing X-ray diffraction (XRD) and Raman spectroscopy.

(4) measure and compare the surface roughness and adhesion strength of the deposited alumina layers to study the reliability aspects related to the morphological features of alumina coatings.

1.6. Thesis Outline

The present thesis document has five chapters and the following structure:

Chapter 2 contains a comprehensive literature review on thermally sprayed resistive heating systems, the function of each layer in the heating system and the proper materials and their desired properties are fully discussed. Chapter 3 focuses on the fabrication of multi-layered coating-based heating systems and the experimental procedure is explained in detail. Chapter 4 presents the obtained results and the findings are discussed. The coating characterization and the data extracted are presented, and further observations are performed. As a final point, the conclusions of the work and suggestions for future research are specified in Chapter 5.

Chapter 2. Literature Review

2.1. Coating-Based Resistive Heating Systems

Over the past century, thermal spray has been greatly refined and optimized and has become an essential component of today's industry. Nowadays, thermal spray is known to be a reliable and cost-effective method capable of producing a variety of coatings with the desired thickness and material. In the recent years, thermally sprayed coatings as electric resistance heating systems have attracted increasing attention; however, usage of thermal-sprayed coatings in electronics goes back to five decades ago where arc plasma spraying (APS) was used to fabricate planar ferrite microwave integrated circuits (MIC's) [55]. In the literature there are many studies showing the feasibility of using thermal spray techniques to create electrical components ranging from insulators, conductors, and resistors. For instance, Smyth and Anderson [56] studied the effect of spraying parameters on the physical and electrical properties of film resistors. It was found that APS process can be an alternative method to fabricate cheap resistors and conductors with satisfactory long-term stability.

Later on, Younis, *et al*. [31] proposed air plasma sprayed resistance heaters. The metal film heater was made of molybdenum and a plasma-sprayed ceramic film was used to isolate the metallic layer from the faceplate. The proposed system was able to generate heat fluxes up to 7.2 MW/m^2 over an area of 10.3 cm^2 showing the possibility of using thermal-sprayed coating as heating systems. It is worth mentioning that the direct deposition of the films onto the substrate

significantly minimizes the thermal contact resistance between the top and bottom layer which leads to a more efficient heating elements compared to when the heater is being mechanically attached to the surface [32]. Furthermore, the application of thermal spray techniques in meso-electronics fabrication was studied by Sampath, *et al.* [57]. It was reported that electrical components such as insulators, conductors, and resistors can be produced by deposition of a multi-layered system of ceramics and metals with the right electrical properties.

The production of a thermally sprayed resistive layer is reported by Russegger [58] that corresponds to a specific shape. The electrically conductive layer was first deposited evenly on a non-conductive substrate. Then, certain parts of the deposited layer were removed by using a laser beam to fabricate complex patterns of the resistive heating layer. Brook-Levinson, *et al.* [59] used plasma spraying and flame spraying to fabricate heating elements by using a metallic powder that contained boron as a feedstock. It was found that during the spraying process, the structure of the powder particles transformed, and the liquid particles were coated with a layer of boron oxide. An electrically insulating layer was applied to the target substrate before applying the metallic powder and the top pore of the insulating layer was impregnated by a silicon organic compound. Care was taken to adjust the thickness of the insulating layer to optimize the transfer of thermal energy between the top heating layer and the substrate.

The performance of a heating system mainly depends on the electrical resistance of the metallic alloy used as the heating elements layer, the substrate material, and its electrical conductivity. Given the high thickness required to achieve the desired electrical resistance for heating purposes, thermal spraying techniques are preferred over vapor deposition processes [32]. It is well established that the electrical conductivity of the substrate material affects the configuration of the heating system. In cases where the substrate is electrically conductive, an

intermediary ceramic layer is required to prevent short circuit and leakage of current between the top conductive heating layer and the substrate. Hence, a multi-layered heating system usually consists of two main layers, namely the heating element (usually a metallic alloy) and the electrically insulating layer (usually a ceramic material with high dielectric strength).

2.2. Deposition of Metallic Alloy Coatings as a Heating Element

There are several previous studies that have investigated the potential application of thermal spraying processes in manufacturing heating systems. Processes including air plasma spray (APS), vacuum plasma spray (VPS), and high-velocity oxygen fuel (HVOF), wire arc, combustion spray, and wire flame spray and materials such as molybdenum (Mo), nickel (Ni), nickel-20 wt.% chromium (Ni-20Cr), nickel-5 wt.% aluminum (Ni-5Al), iron-13 wt.% chromium (Fe-13 Cr), and Iron-chromium-aluminum (FeCrAl) have been reported for usage in the heating element layer [19, 20, 31–33, 51, 52].

In a study done by Michel, *et al.* [32], resistance heating elements were produced by using APS, VPS, HVOF thermal spray techniques with the aim of producing easily controlled and uniform heat flux. More consistent coatings with properties closer to that of the bulk material were obtained from the HVOF and VPS processes. The material used in the heating element layer was reported to be a nickel-chromium alloy (Ni80-Cr20) which was deposited onto a ceramic electrically insulating layer (alumina) to stop the current flow between the heating layer and the electrically conductive copper substrate.

The required thickness for the alumina layer was found to be around 100 µm for HVOF and 200 µm for APS to better isolate the heating element from the substrate. A schematic view of the produced heating system can be used in Fig. 2-1. The heat generation of the proposed heating

systems were tested under different electric currents and values as high as 10.6 MW/m^2 and 17.2 MW/m^2 were obtained for HVOF and VPS coatings, respectively. Delamination of the heating element layer from the ceramic layer was observed at high-level electric currents that might have been caused by the mismatch between the thermal expansion coefficient [32].

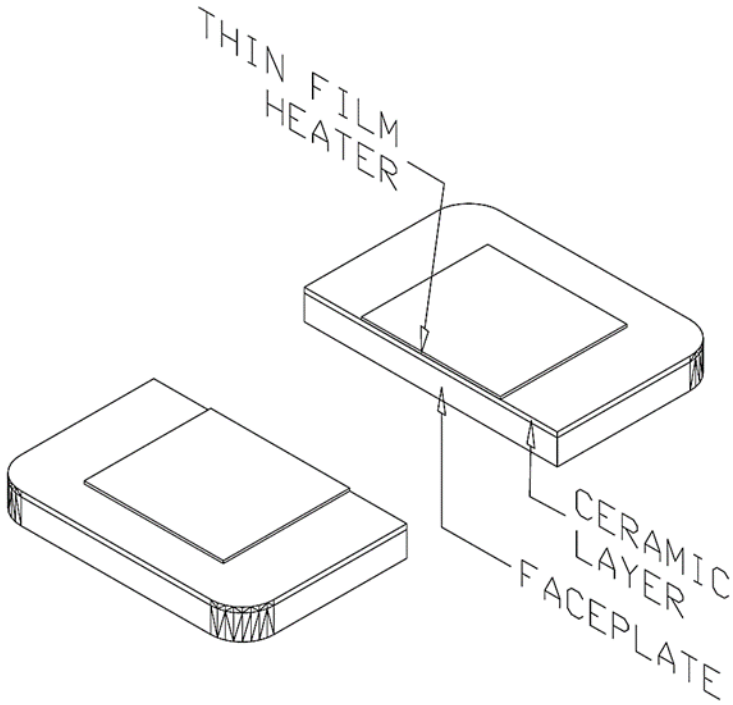

Figure 2-1 Schematic view of the deposited multi-layered heating system [32].

In another study done by Killinger, *et al.* [33], a multi-layered heating system was produced by using APS process. The heating system was consisted of nickel-chromium (Ni-20Cr) as the heating element layer, alumina as the electrically insulating layer and glass ceramic/stainless steel as the substrate. The microstructure and electric properties of each essential component were investigated. The thickness of the alumina and Ni-20Cr layers were reported to be 200 and 30-50 μm, correspondingly. It was found that deposition of a thicker Ni-20Cr coating would be

challenging as the residual tensile stresses can reach very high values causing delamination of the metallic layer. Micrographs of the deposited heating system can be seen in Fig. 2-2.

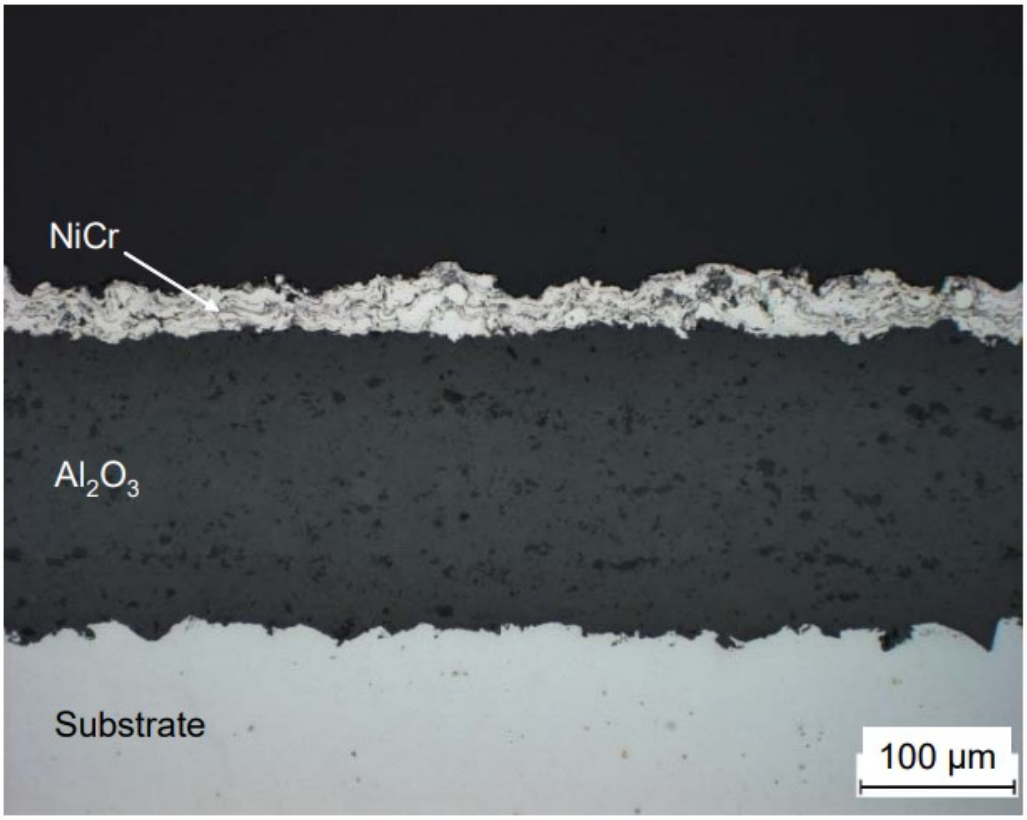

Figure 2-2 Micrograph obtained from the produced metal-ceramic composites. Ni20Cr/Al_2O_3 on a stainless steel substrate [33].

Air plasma sprayed resistance heaters were designed in both planar and cylindrical geometries by Prudenziati, *et al.* [61]. As shown in Fig. 2-3, heating elements made of Ni, Ni-20Cr, and Ni-5Al were fabricated in the shape of meanders by engraving metal masks. The developed self-regulated heaters were able to consistently function at temperatures as high as 600°C over a long period of time. These heating elements could also be used as a smart sensor for reading the heater temperature directly without the need to install a separate temperature sensor as

the heaters' electrical resistance was highly dependent on temperature. That said, the proposed heating system can also be used in high-temperature operating sensors field.

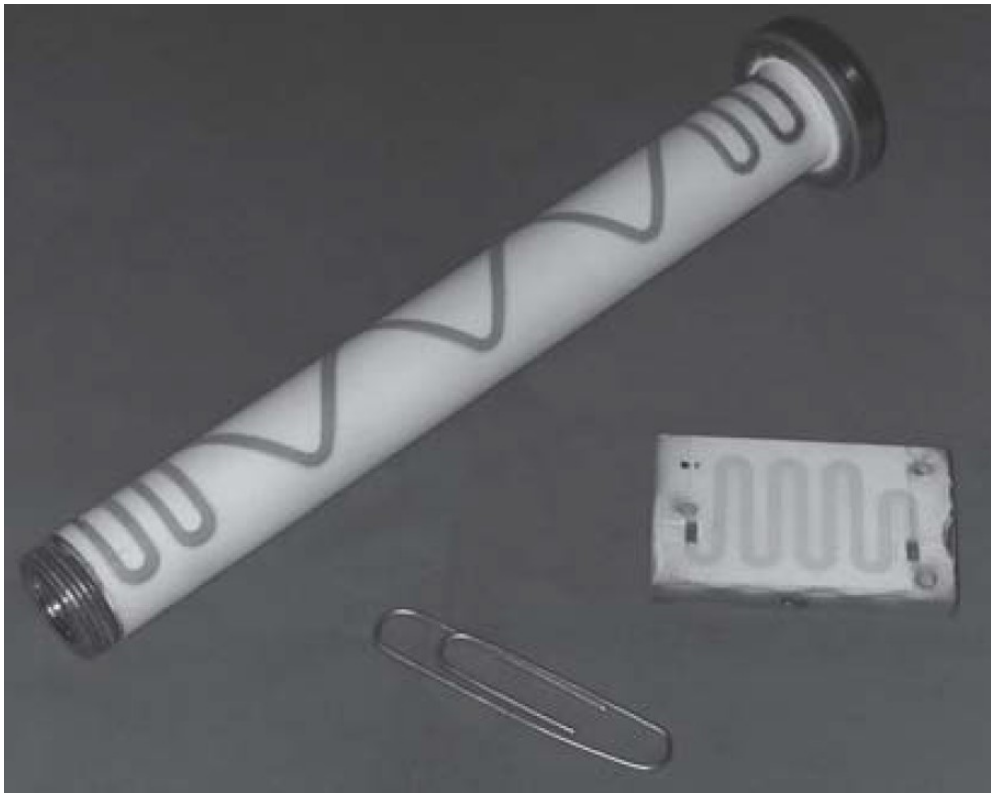

Figure 2-3 Developed air plasma sprayed cylindrical and planar heaters [61].

Lamarre, *et al.* [19] proposed a finite-element thermal analysis (FEA) to investigate the failure mechanisms of thermally sprayed resistive heating system at elevated temperatures. In this study, plasma spray process was used to deposit a 250-300 µm alumina coating on a metallic substrate. On top of the alumina layer, a 75-100 µm iron-based alloy (FeCrAl) was sprayed using a wire flame-sprayed method. The heating system configuration can be seen is Fig. 2-4. The cylindrical heater was kept at a constant temperature of 425°C for up to four months and its performance and microstructure were examined.

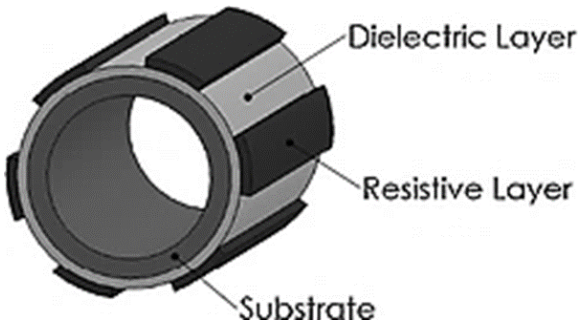

Figure 2-4 A schematic of a part of the proposed cylindrical heater. The layer thickness and size of each component is not up to scale [19].

Several experimental techniques were applied to measure physical properties (mechanical, electrical, and thermal) of the heating system and their values were directly used in the FEA to correspond to the simulation and actual performance of the heaters. Based on the results obtained from the simulation model, high-stress zones were indicated at the intersection of FeCrAl, alumina, and the ambient air matching the cracks observed in the obtained SEM images (Figure 2-5). It was concluded that by reducing the alumina thickness, the maximum stress can decrease, but it leads to an increase in the average stress in the alumina layer [19].

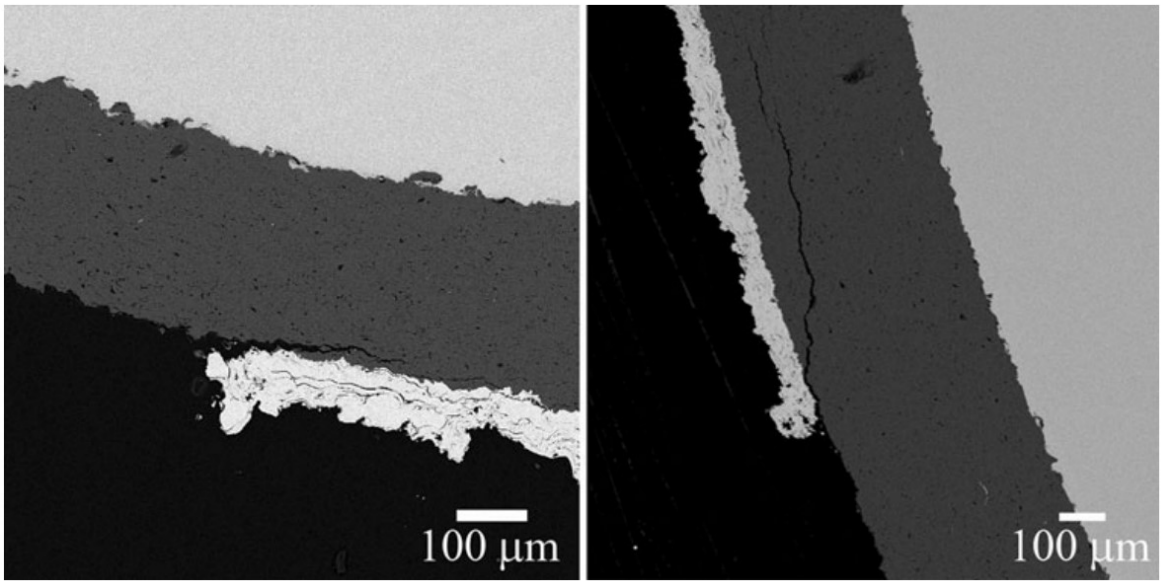

Figure 2-5 SEM images of the heaters after thermal testing. Cracks originated from the intersection of the resistive layer, the alumina layer, and the ambient air [19].

Lopera-Valle and McDonald [21, 53] first proposed flame-sprayed restive heating systems as a novel technique to eliminate ice formation on fiber-reinforced polymeric composite-based wind turbine blades. In this study, nickel-chromium-aluminum-yttrium (NiCrAlY) and nickel-chromium (NiCr) were deposited as the heating element layer onto an electrically non-conductive fiber-reinforced polymer composite (FRPC) substrate. The NiCrAlY and Ni-20Cr coatings had a thickness of 80 ± 15 µm (n = 20) and 100 ± 15 µm (n = 20), correspondingly. As it can be observed in Fig. (2-6), a layer of garnet sand was used as an intermediary layer between the FRPC and the metal alloy coating to prevent damaging the composite fibers during the deposition of high-temperature molten powder particles. It was found that by supplying a power as low as 2.5 W over 3 V, in a condition where no air was flowing over the sample, the FRPC's temperature was 15°C above the ambient temperature [21]. In another study done by the same authors [62], it was

reported that the coating-based de-icing system was reliably operating when the sample was exposed to forced convection and the ice formed on top of the composite was successfully melted.

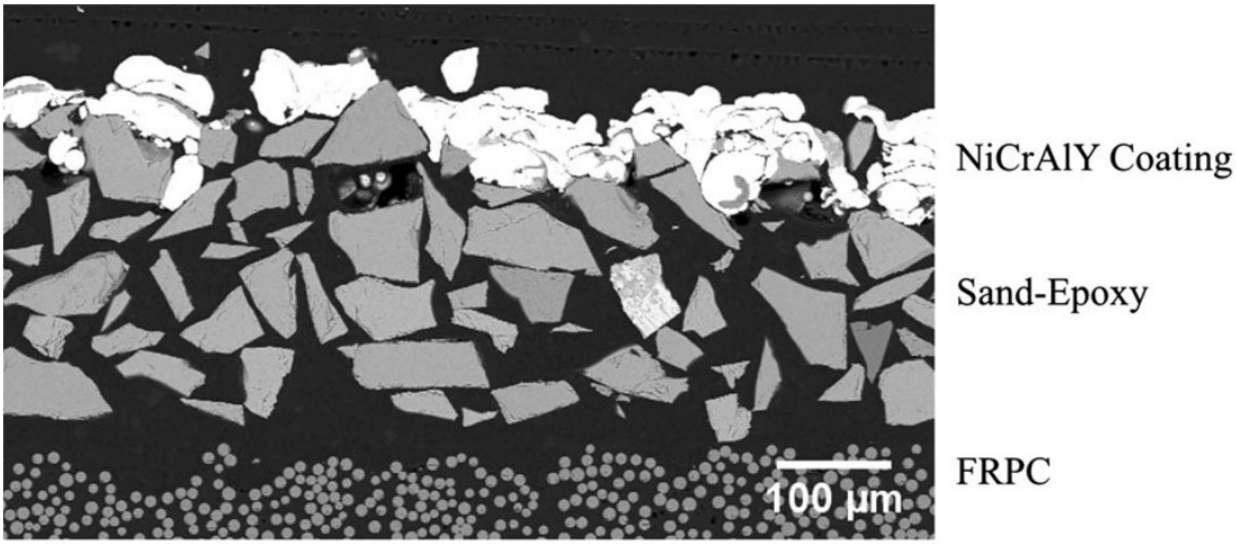

Figure 2-6 Cross-sectional SEM images taken from the coated FRPC samples [21].

Rezvani Rad and McDonald [63] studied the possibility of producing a thermally sprayed heating system on an electrically conductive low-carbon steel pipe. Nickel-50 wt.% (Ni-50Cr) was chosen to serve as the heating element layer. Intermediary alumina layer was deposited on to the pipe surface prior to deposition of the Ni-50Cr layer to provide an electrical insulation between the top heating element and the conductive substrate. The dielectric alumina layer also prevents the free electrons from passing through the low-carbon steel pipe with less electrical resistance compared to the deposited heating element. Figure 2-7 shows different parts of the developed heating system.

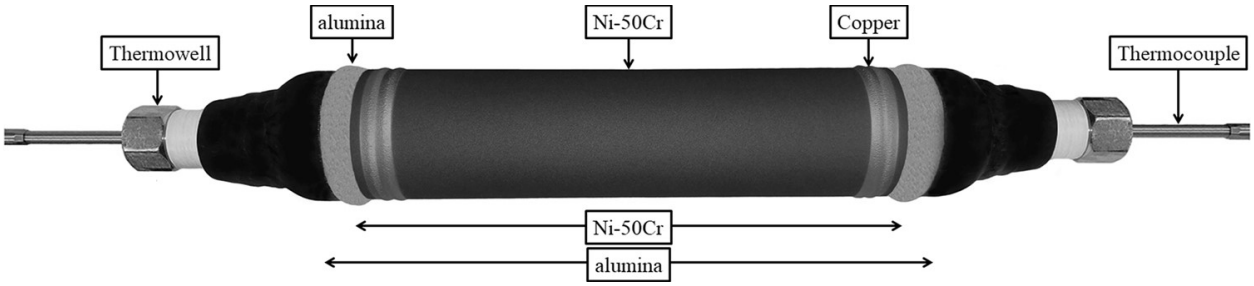

Figure 2-7 Multi-layered heating system developed by flame spraying [63].

2.3. Deposition of Ceramic Coatings as an Electrically Insulating Layer

2.3.1. Ceramics

In materials science, materials are often divided into distinct classes. Ceramics, metals, and polymers are the primary classes of solid materials which are based on the types of atoms involved and the bonding between them. *Ceramics* usually include "mixed" bonding (i.e., a combination of covalent, ionic, and sometimes metallic type bonding) and are usually consisted of arrays of atoms [64]. The fact that no discrete molecules exist in ceramics is a characteristic that distinguishes ceramics from molecular solids such as iodine crystals (composed of I_2 molecules) and paraffin wax (composed of long-chain alkane molecules). Even ice that often exhibits ceramic-like behavior contains discrete H_2O molecules proving that it is not a ceramic [65].

Ceramics are made of compounds of metals or metalloids and non-metals and they are often found in the form of oxides, nitrides, and carbides. Richerson [66] defines ceramics as materials that are not metal, plastic, or derived from plants or animals. Kingery, *et al.* [67] has given the most widely accepted definition of a ceramic which is: "A ceramic is a nonmetallic, inorganic solid.". Considering the above-mentioned definitions, a material stops being a ceramic when it melts. On the other hand, if some ceramics are cooled down, they become superconductors.

The glass that is being used in windows and optical fibers is also a ceramic. Glass has its own fixed shape and fulfills the standard definition of a solid, but it is usually a supercooled liquid which makes it clear that glasses are special ceramics. Therefore, it is not possible to define ceramics, or indeed any class of materials as there are always exceptions in terms of certain properties [28].

Specific properties are associated with ceramics although, as mentioned earlier, it can be challenging to have a unique definition for a whole class of material. However, the following properties are generally related to ceramics: 1. Brittleness 2. Poor electrical and thermal conduction. 3. Compressive strength. 4. Chemical insensitivity 5. Transparent [68].

Properties mentioned are in most cases different from those shown in metals and polymers. It should be noted that ceramics with atypical behavior are always possible to be found. Ceramics are used in diverse applications and it is mainly because of the wide range of properties that these materials possess. A detailed list of examples of specific ceramics and their applications can be seen in Table 2-1.

Table 2-1. Properties and applications for ceramics [68].

Property	***Example***	***Application***
Electrical	$Bi_2Ru_2O_7$	Conductive component in thick-film resistors
	Doped ZrO_2	Electrolyte in solid-oxide fuel cells
	Indium tin oxide (ITO)	Transparent electrode
	SiC	Furnace elements for resistive heating
	$YBaCuO_7$	Superconducting quantum interference devices (SQUIDs)
	SnO_2	Electrodes for electric glass melting furnaces
Dielectric	α-Al_2O_3	Spark plug insulator

	$PbZr_{0.5}Ti_{0.5}O_3$ (PZT)	Micropumps
	SiO_2	Furnace bricks
	$(Ba,Sr)TiO_3$	Dynamic random-access memories (DRAMs)
	Lead magnesium niobite (PMN)	Chip capacitors
Magnetic	γ-Fe O_3	Recording tapes
	$Mn_{0.4}Zn_{0.6}Fe_2O_4$	Transformer cores in touch tone telephones
	$BaFe_{12}O_{19}$	Permanent magnets in loudspeakers
	$Y_{2.66}Gd_{0.34}Fe_{4.22}Al_{0.68}Mn_{0.09}O_{12}$	Radar phase shifters
Optical	Doped SiO_2	Optical fibers
	α-Al_2O_3	Transparent envelopes in streetlamps
	Doped $ZrSiO_4$	Ceramic colors
	Doped (Zn, Cd) S	Fluorescent screens for electron microscopes
	$Pb_{1-x}La_x(Zr_zTi_{1-z})_{1-x/4}O_3$ (PLZT)	Thin-film optical switches
	Nd doped $Y_3Al_5O_{12}$	Solid-state lasers
Mechanical	TiN	Wear-resistant coatings
	SiC	Abrasives for polishing
	Diamond	Cutting tools
	Si_3N_4	Engine components
	Al_2O_3	Hip implants
Thermal	SiO_2	Space shuttle insulation tiles
	Al_2O_3 and AIN	Packages for integrated circuits
	Lithium-aluminosilicate glass ceramics	Supports for telescope mirrors
	Pyrex glass	Laboratory glassware and cookware

2.3.2. Oxide Ceramics

Ceramics can be classified into three separate material categories of oxides (e.g. alumina, zirconia, ceria, etc.), non-oxides (e.g. carbide, boride, nitride, etc.), and composite materials (e.g. combination of oxide and non-oxides). Oxide ceramics mainly contain simple oxides in their microstructure. Ceramics with complex oxides that are for instance formed by solid state reactions, and silicate ceramics are usually not known as oxide ceramics [69].

Aluminum oxide (Al_2O_3), commonly referred to as alumina, is known to be one of the most cost-effective ceramic materials and it is widely being used in structural engineering materials. Alumina's raw material can be easily found at a reasonable price which leads to the production of a high performance material with an affordable price [70]. Alumina's strong iono-covalent interatomic bonding is one of main reasons behind its desirable characteristics such as outstanding resistance to abrasion, wear, and corrosion [71,72]. Among oxide ceramics, alpha phase alumina (α-Al_2O_3) has the highest strength and stiffness [73]. It exhibits high thermal stability and high electrical resistance and it is also compatible with living tissues. α-Al_2O_3 is used in numerous applications such as polishing powder, material for crucibles, cutting tools, spark plugs and many more [65, 66].

Alumina is mostly produced from Gibbsite ($Al(OH)_3$) and boehmite (AlOOH) precursors. During the heat treatment process, aluminium hydroxides transform into metastable alumina structures, also known as transition alumina, prior to the production of thermodynamic stable alpha phase (α-$A1_2O_3$) [76]. Detailed transformation sequences of gibbsite to alpha alumina is shown in Fig. 2-8. Under a temperature range of 500-550 °C, boehmite transforms into γ-$A1_2O_3$ transition alumina through removal of structural water [77]. The γ-$A1_2O_3$ (monoclinic phase with d = 3.56

g.cm^{-3}) → α-$A1_2O_3$ (hexagonal phase with d = 3.98 g.cm^{-3}) transformation is accompanied by a volume reduction of about 10% leading to a huge increase in density [78].

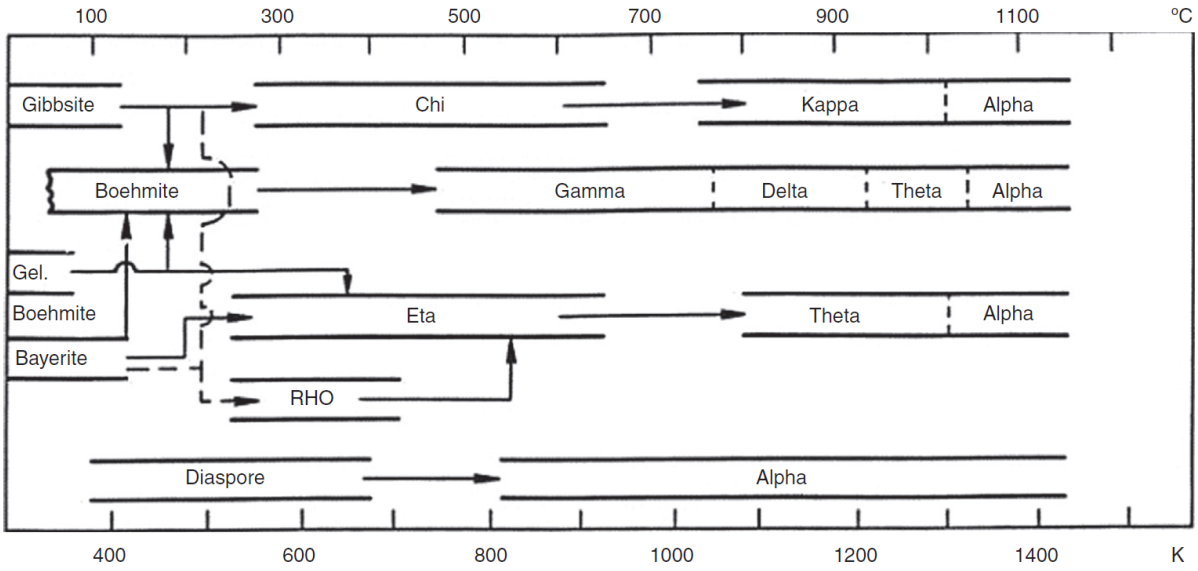

Figure 2-8 Transformation sequences of gibbsite ($Al(OH)_3$) to α-$A1_2O_3$ [77].

Alpha alumina, which is also known as corundum, is the most thermodynamically stable form of alumina between room temperature and its melting point at 2050 °C. As shown in Fig. 2-9, α-Al_2O_3 forms a lattice of hexagonally close-packed oxygen atoms with stacking order AB-AB…, and Al cations occupy two thirds of the octahedral sites and oxygen onions fill the remaining one third [69]. Corundum classifies in the rhombohedric system, space group $R\bar{3}c$. At room temperature the lattice parameters are, in hexagonal axes, a = 0.4759 nm and c = 1.2999 nm, with Z = 6 [79].

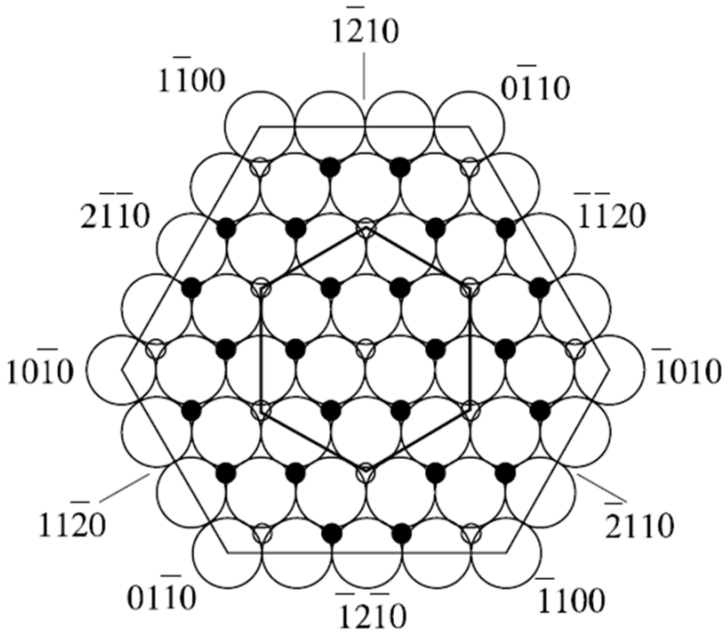

Figure 2-9 Structure of α-Al_2O_3, large circles represent the anions, the small full circles the cations, the small empty circles the vacant octahedral interstices.

2.3.3. Ceramic Insulators

Providing physical separation between conductors and mitigating or preventing the current flow between conductors are primary functions of an insulator in an electrical circuit. In addition, providing mechanical support, heat dissipation, thermal shock resistance, and a chemically stable environment for the conductors are few other responsibilities of an electrical insulator [80]. Ceramic materials such as glasses, porcelains, oxides, nitrides, and mica are classified as ceramic insulators. One of the main advantages of ceramics when being used as electrical insulators is their ability to withstand high temperatures without experiencing hazardous degradation in chemical, mechanical, or dielectric properties [81]. Ceramics can be advantageous where use specifications

like high electrical resistance, high dielectric strength, as well as relatively low dielectric constant and loss are required [82].

To determine the insulating characteristics of a material, properties such as relative dielectric constant (ε_r), electrical (volume) resistivity (ρ), the dissipation factor (tan δ), and the dielectric strength (DS). Relative dielectric constant (ε_r) is defined as a way to measure the ability of the material to store charge, relative to the permittivity or dielectric constant of vacuum (ε_0 = 8.85 $\times 10^{-12}$ F/m) [1]. The electrical resistivity (ρ) is a measure of the resistance that a unit cube of the material offers to current flow in a given field. The dissipation factor (tan δ) measures the energy loss per cycle, mostly in the form of heat [83]. Dielectric strength is defined as a measure of the maximum voltage gradient that can be applied across the dielectric without physical degradation of its insulating properties, leading to breakdown. The dielectric strength is not a true material property since it is significantly influenced by measurement conditions, sample size, and flaws within the ceramic.

Generally, ceramics materials that place in the following property criteria at 25°C are usually considered as good insulators [84]:

- Dielectric constant (ε_r) $\leq$30
- Electrical resistivity (ρ) $\geq 10^{12}$ (Ω-cm)
- Dissipation factor (tan δ) $\leq$0.001
- Dielectric strength (DS) $\geq$5.0 kV/mm
- Dielectric loss factor (ε''_r) $\leq$0.03

2.3.4. Application of Thermally sprayed Alumina as an Electrically Insulating Layer

Properties such as wear resistance, high temperature and chemical stability, high hardness as well as electrical insulation are few of the characteristics exhibited by oxide ceramics (e.g., Al_2O_3, Cr_2O_3, TiO_2, and ZrO_2) [85]. Thanks to the electrical insulating properties of these materials, they are widely being used in demanding conditions including harsh environments where exposure to mechanical or chemical stresses is high, on complex geometries, or where normal insulating materials such as polymers are not suitable [86]. Over the past years, the application of oxide ceramics as an intermediary layer in coating-based resistive heating systems has attracted a lot of attention [20, 32, 78]. Alumina is one of the materials that is widely being used as a suitable material for electrical insulating purposes because of its desired dielectric properties, low cost, and availability [79, 80].

Thermal spraying as a rapid and industrial manufacturing process to deposit electrical insulating coatings on large surfaces has been an interesting option for today's industry. Tesar, *et al.* [90] investigated the microstructure of alumina coatings deposited by using a high enthalpy hybrid water-stabilized plasma torch. Both columnar and well-sintered dense structures were observed in the deposited coatings. In another study Müller, *et al*. [91] conducted a comparison on microstructures of the alumina coatings that were produced by suspension plasma spraying and high-velocity suspension flame spraying (HVSFS) processes (Fig. 2-10). It was shown that relatively higher porosity values were acquired from SPS deposition compared to HVSFS method.

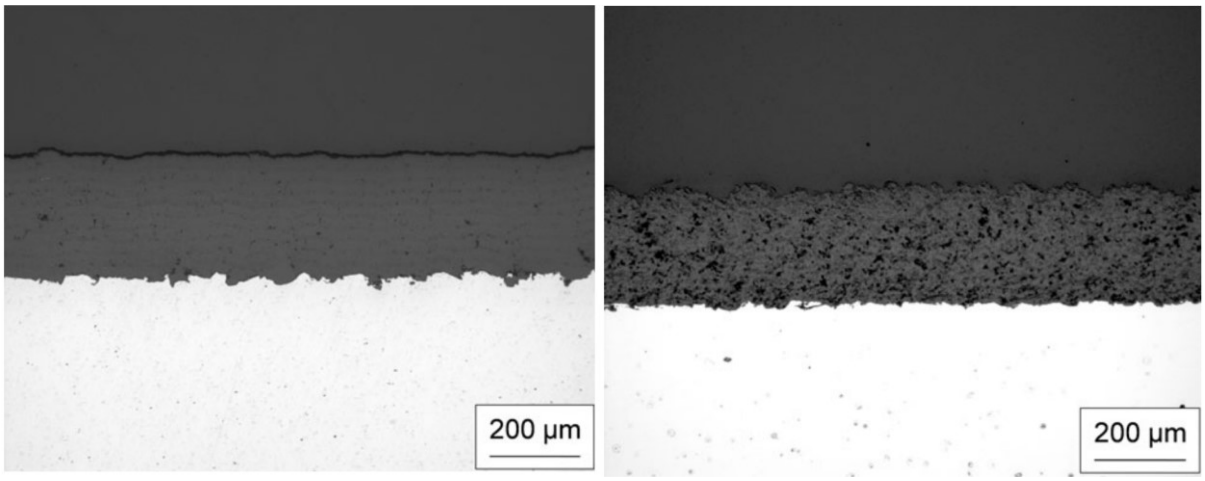

Figure 2-10 Light microscope cross-sectional images of HVSFS-sprayed and SPS-sprayed alumina coatings [91].

Electrical properties of thermally sprayed alumina is affected by several factors, namely humidity, temperature, applied pressure, phase composition, and microstructural characteristics [89,88,92–94]. In a study conducted by Pawlowski [95], the volume resistivity of plasma-sprayed alumina was reported to be within the range of 10^9 - 10^{10} Ω cm. The relative humidity and its impact on alumina's resistivity were investigated by Toma, *et al.* [89]. It was reported that when the relative humidity reached to 95%, alumina coating's resistivity dramatically decreased and resulted in deterioration of the coating. This deterioration was reported to be associated with the increase in surface conductance of the oxide layer caused by water accumulation on the coating's surface [92].

Niittymäki, *et al.* [96] further studied the effect of environmental factors such as humidity and temperature on electric properties of alumina coatings produced by several thermal spraying processes such as HVOF, APS, and FS. It was reported that when increasing the measurement temperature from 300 to 800 °C, the breakdown strength of the alumina coatings was adversely

affected and the values reported at elevated temperature were only 14% of that of reported at 20 °C. Moreover, it was found that high amount of relative humidity can decrease alumina's resistivity to $10^7 – 10^8$ Ω mm. In another study, the effect of applied pressure on surface resistivity of alumina coating was studied [88]. It was reported that when applying pressure on the alumina coating, its surface resistivity decreases. However, the value reported for resistivity was still higher than 10^6 Ω cm when exposed to pressures up to 250 MPa. Cross-sectional images of the studied coatings can be observed in Fig. 2-11.

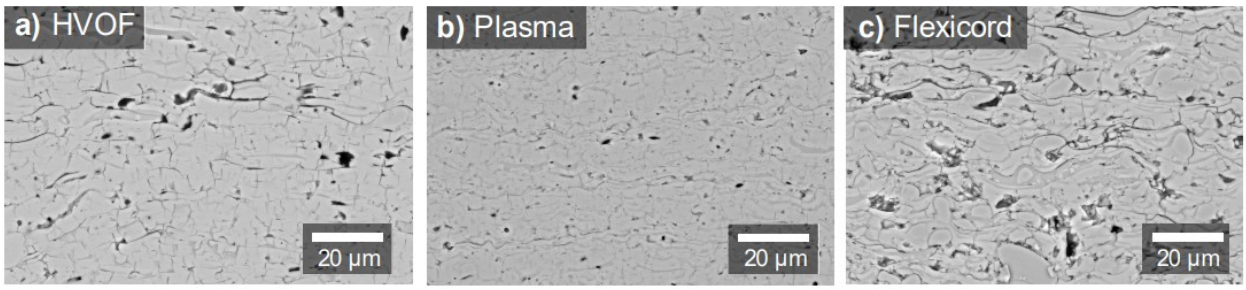

Figure 2-11 SEM/BSE images of the deposited coatings [96].

Phase transformation of alumina is another well-known factor determining the dielectric properties of thermal sprayed alumina coating. It should be noted that sintered alumina mainly consists of thermodynamically stable α-Al_2O_3 (Corundum) [97]; however, thermally sprayed alumina is reported to have high quantity of metastable phases (γ-Al_2O_3, δ-Al_2O_3, and θ-Al_2O_3) that exhibit significantly different properties compared to corundum [89]. Typical alumina feedstock powder used for thermal spraying mainly consists of α-Al_2O_3; however, during the spraying process, particles melt and transform into highly hygroscopic γ-phase [86, 89, 90]. Metastable phases strongly react with water and water vapor followed by a significant increase in alumina's dielectric constant which results in poor performance in humid environments. That said, type of the thermal spray process used, velocity, size, and temperature of the particles during and

after spraying determines the final phase composition and performance of the coating [100]. As reported by Niittymäki, *et al.* [96], high absorption of moisture in thermally sprayed alumina coatings is mainly caused of: (1) notable amount of γ-Al_2O_3 in the coatings giving a hygroscopic nature to the coatings and (2) lamellar microstructure of thermal spray coatings, consisting of amorphous and crystalline regions that can intensify the sensitivity of the coatings to moisture.

Rapid cooling of the molten alumina particles below the atomic rearrangement temperature results in formation of undesired phases before the stable phase of corundum [101]. According to a study done by McPherson [98], formation of the metastable phase happens during the cooling process of particles with a diameter less than 10 µm as these particles cooling rates are much higher compared to large particles. Larger particles are most likely to retain the α-Al_2O_3 or to get transformed into α-Al_2O_3 during solidification. Furthermore, the effect of α/γ phase on the dielectric properties of APS alumina was investigated by Gao, *et al.* [102]. A larger number of particles were melted at higher plasma arc currents that led to phase transformation of the initial stable powder to γ-Al_2O_3. As the ratio of the γ-Al_2O_3 increased, an increase in the dielectric constant was observed. Thus, there has been a continuous struggle to retain α-alumina to the greatest possible extent in thermally sprayed coatings [90].

The electrical properties of the alumina layer can also get affected by the different microstructural features obtained by using different thermal spray processes. Killinger, *et al.* [33] reported that breakthrough voltage and leakage current are two of the most important factors for characterizing the electrically insulating layer which are greatly influenced by the internal morphology of the coatings. A rise in the breakdown voltage values were observed as the coating's

thickness increased. A pin hole produced by the high-voltage breakdown within the alumina coating can be observed in Fig. 2-12.

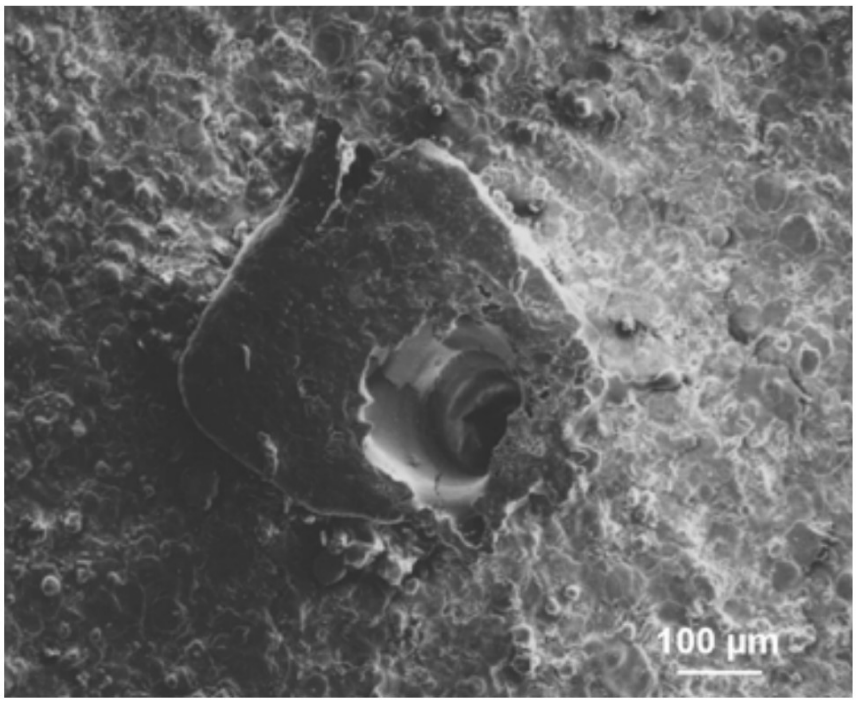

Figure 2-12 Pin hole formed due to high-voltage breakdown within the APS alumina coating [33].

HVOF-sprayed alumina coatings were reported to have better electrical resistivity compared to APS sprayed alumina which was mainly attributed to lower amounts of porosity, open pores, and defects observed within the HVOF alumina [89]. According to the study done by Kotlan, *et al*. [99], it was found that by increasing the spraying distance from 100 mm to 200 mm in the APS process, the alumina's final dielectric strength decreases from 16.6 kV/mm to 13.5 kV/mm. One way to justify this observation was to consider the well-established fact that higher stand-off distances, regardless of the type of material, reduces particle velocity and temperature forming a more porous structure [103].

Chapter 3. Experimental Procedure

In this chapter step by step experimental methodology is explained and the characterization methods employed to assess the properties of the prepared samples are thoroughly described. First, the type of substrates and their preparation method prior to the spraying process are introduced. Then, the powder feedstock that was utilized in each of the coating processes are presented. The spraying parameters and the chosen test conditions to produce the electrically insulating and the heating element coatings are discussed in detail. At last, each characterization method and their specifications are reported accordingly.

3.1. Substrate Preparation

Three different substrate dimensions were chosen for sample preparation: including

1. square-shaped substrates (also known as coupons) with 6-mm (0.25-inch) thickness, 25-mm (1-inch) length, 25 mm (1-inch) width,

2. rectangular-shaped substrates with 6-mm (0.25-inch) thickness, 75-mm (3-inch) length, 25 mm (1-inch) width,

3. rectangular-shaped substrates with 6-mm (0.25-inch) thickness, 150-mm (6-inch) length, 75-mm (3-inch) width.

Numerous coating systems with different spraying parameters were deposited to investigate the effect of each spraying condition in the electrical and microstructural properties of the coating systems. Steel plates of A36/44w mild steel hot rolled flat bar (Metal Supermarkets, Ottawa, ON, Canada) were water jet cut to produce the substrates with the desired dimensions. The employed substrates ready for coating spraying are shown in Fig. 3-1.

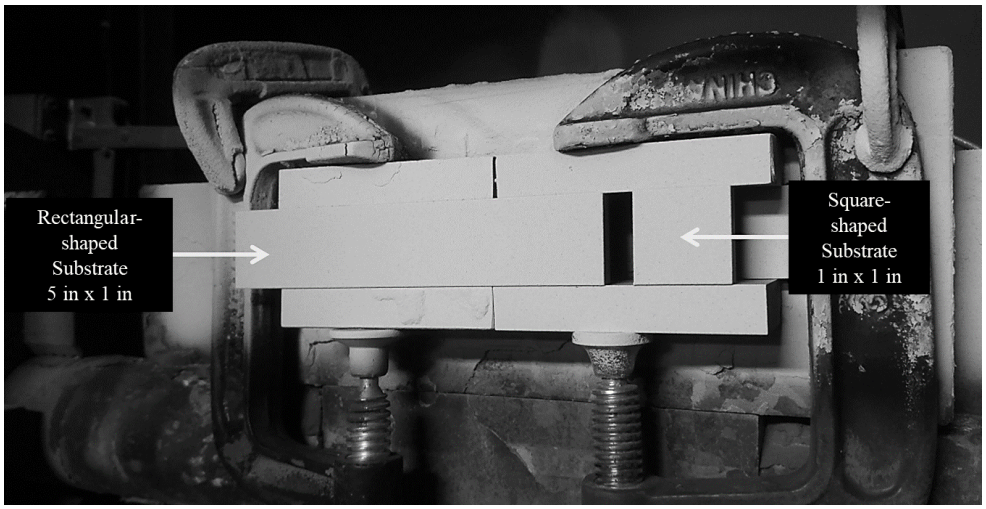

Figure 3-1 Steel substrates with two different dimensions used for preparing the coating systems.

Prior to spraying, in order to increase the surface roughness, substrates were grit blasted with #24 alumina grit (Manus Abrasive Systems Inc., Edmonton, AB, Canada) at an air pressure of 586 kPa (85 psig) for the flame spraying (FS) process. A finer #80 alumina grit (International Surface Technologies, Montreal, QC, Canada) at an air pressure of 689 kPa (100 psig) was used to grit blast the substrates before suspension plasma spraying (SPS). Choosing the right grit size is important as it affects the adhesion and interlocking between the powder particles and the substrate. All substrates were preheated by passing the flame/plasma over the samples several

times to decrease the tensile stresses that were generated during the cooling stage and solidification of the alumina molten droplets.

3.2. Feedstock powder

Various powder materials were utilized in this study to fabricate coatings by FS, SPS, and air plasma spraying (APS) processes. Pure alpha phase alumina powder was used in both FS and SPS processes. Depending on the deposition technique, appropriate particle size distribution was selected. Alumina (Al_2O_3, AMDRY 6060, Oerlikon Metco, Fort Saskatchewan, AB, Canada) powder feedstock with a size distribution of 5 to 45 µm (-45+5 µm) was used in the FS process. As shown in Fig. 3-2, the angular/blocky morphology of the powder is associated with their fabrication process which was fusing and crushing [104,105].

Finer alumina feedstock powder was chosen for the SPS process (Al_2O_3, VG-503#, ZiBo V.Gree Trading Co., Zibo, Shandong, China). The size distribution of the SPS alumina powders was (-6+0.2 µm) with nominal average particle size between 0.45 and 1 µm. SPS alumina powder size was chosen in such a way to prevent the sedimentation of particles due to the large size of particles and to prevent agglomeration of them due to the selection of too small particles. The employed powder feedstock is shown in Fig. 3-3.

Figure 3-2 Alumina feedstock used in the FS process [106].

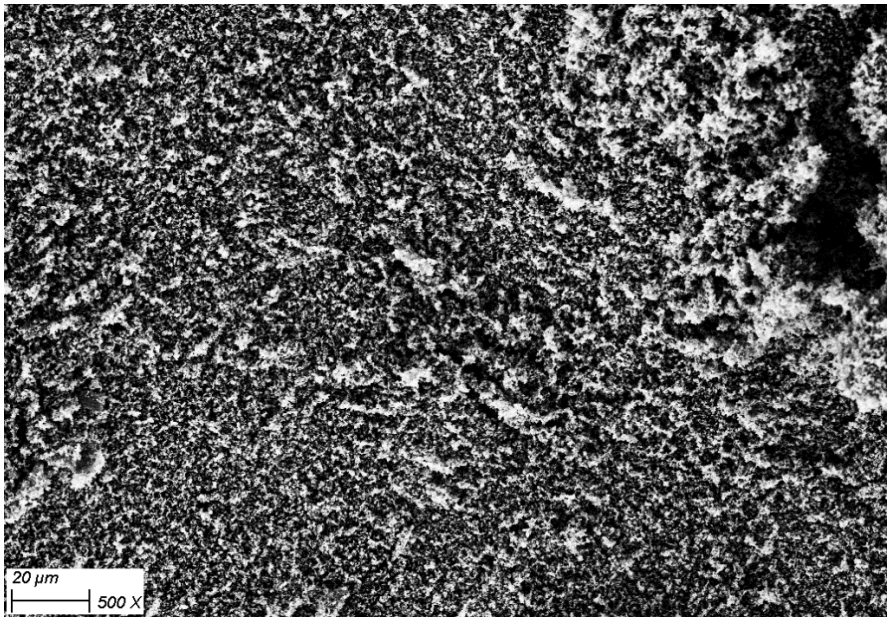

Figure 3-3 Alumina feedstock used in the SPS process [106].

As depicted in Fig. 3-4, commercially available Ni-20Cr powder (Metco 43VF-NS, Oerlikon Metco, Westbury, NY, USA) with size distribution of 5 to 45 µm (-45+5 µm) was used

as the resistive heating layer deposited onto FS and SPS alumina samples by air plasma spraying (APS) and high velocity oxy-fuel (HVOF).

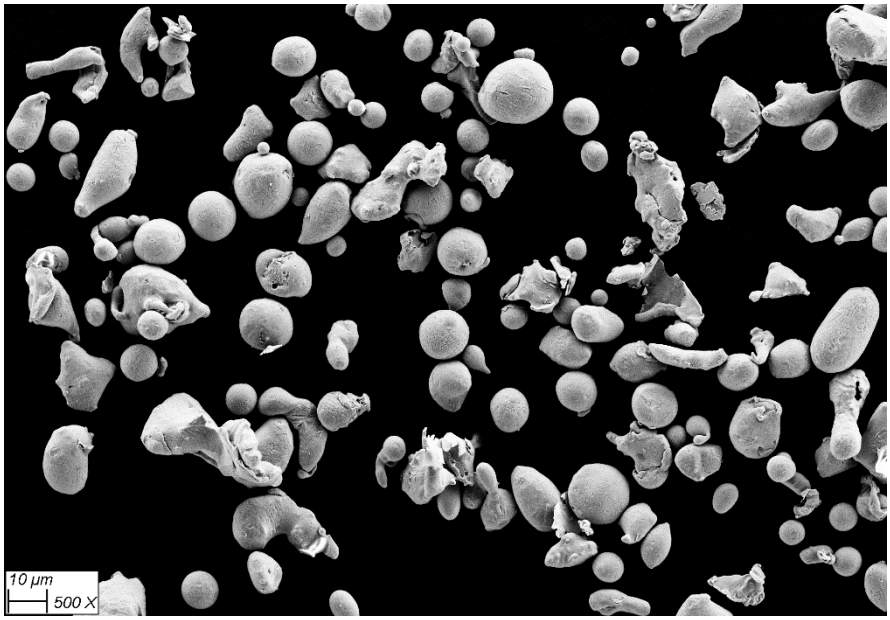

Figure 3-4 Ni-20Cr powder used in the HVOF and APS processes [106].

3.3. Deposition of Electrically Insulating Coatings

To deposit the alumina dielectric layer by using the FS process, two different spraying conditions with different oxygen to fuel ratios were chosen to investigate its impact on the final phase, microstructure, and electrical properties (Table 3-1). Alumina powder was consistently fed to the oxy-acetylene torch (6P-II, Oerlikon Metco, Westbury, NY, USA) by using a volumetric powder feeder (5MPE, Sulzer Metco, Westbury, NY, USA). Argon gas with a flow rate of 0.56 m^3/h (20 standard cubic feet per hour) was used to carry the powder particles. The motion of the FS torch was controlled with a programmable robot (HP-20, Motoman, Yaskawa Electric Corp., Waukegan, IL, USA) to ensure the consistency and repeatability of the spraying process. The FS

alumina samples were all fabricated at the University of Alberta and their microstructural characteristics are fully discussed in a study done by Rezvani Rad, *et al.* [106].

Table 3-1 Flame spraying parameters for deposition of alumina.

Parameters \ ***Coatings***	***FS (1)***	***FS (2)***
Acetylene flow [m^3/h]	1.3	1.5
Oxygen flow [m^3/h]	2.1	1.8
Argon pressure [m^3/h]	0.56	0.56
Flow meter reading (FMR)	100	100
Robot speed [mm/s]	100	100
Stand-off distance (SOD) [mm]	127	127
Number of passes	5	5
Air pressure [kPa]	34.5	34.5
Number of preheating passes	1	1

Three different spraying conditions were chosen for the deposition of alumina coatings using the SPS process. In this study, an ethanol-based suspension was prepared. To avoid settlement and improve particle dispersion, polyvinylpyrrolidone (PVP360, Sigma-Aldrich, Oakville, ON, Canada) was added to the suspension as a dispersant/surfactant. Two suspensions with solid contents of 10 wt.% and 25 wt.% and dispersing agent of 6 wt.% of the solid content were prepared. Both suspensions went through the same preparation steps.

The dispersant was first added to ethanol and was stirred for about five minutes to ensure complete dissolution of the agent before adding the alumina powder. Then, based on the solid content of each suspension, a determined amount of the alumina powder was slowly added to the stirring suspension. The suspension was sonicated with 50 W power during and after the addition of powder for approximately 20 minutes. Particle size distribution of the alumina suspension with 10 wt. % solid content is shown in Fig. 3-5. Particle size distribution widths of D_{10}, D_{50}, and D_{90} were reported to be 0.2, 0.5, and 1.5 µm, respectively.

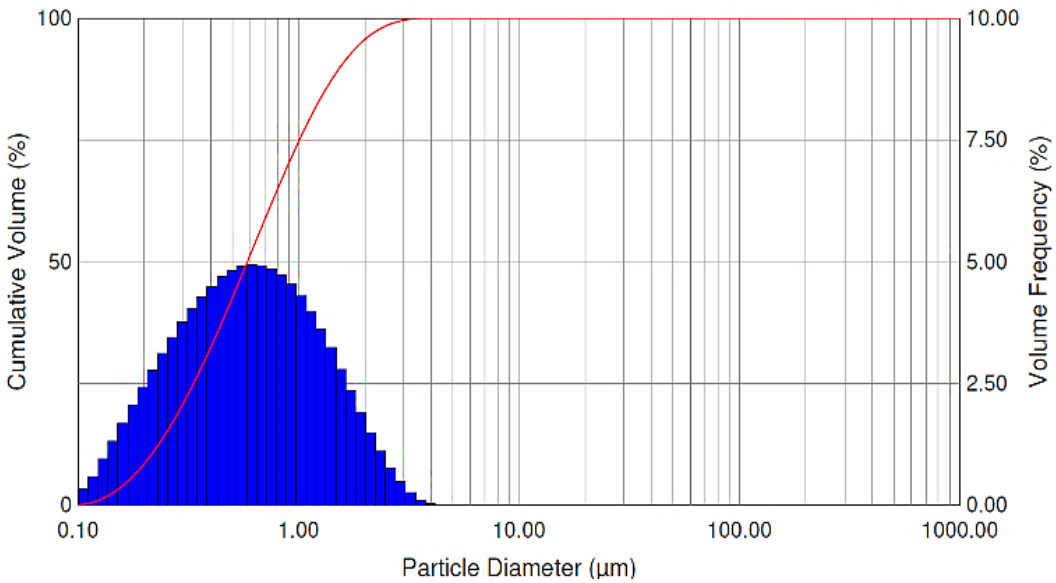

Figure 3-5 Particle size distribution of 10 wt.% alumina suspension.

Axial III plasma torch (Northwest Mettech, Vancouver, BC, Canada) was used for this process. Axial III plasma torch has three cathodes and three anodes that makes it possible to keep the arc fluctuation as low as possible and to have a complete axial projection of the suspension into the plasma. The injection system and the spraying process was automated to provide a constant feed rate. Mechanical stirring of the suspension was continued during the deposition process. Powers of 69 kW, 90 kW, and 111 kW were obtained from different mixtures of the plasma gases.

As shown in Fig. 3-6, coupon substrates were mounted on a rotating sample holder and were consistently air-cooled during spraying. Substrate temperature was monitored during the spraying process with a thermocouple (Nextel®-Covered Flexible Thermocouple Elements, St-Eustache, Canada) and a customized wireless setting. Controlling samples temperature was crucial to limit any kind of phase transformation and care was taken to keep the temperature below 500°C. The detailed SPS spraying parameters are shown in Table (3-2).

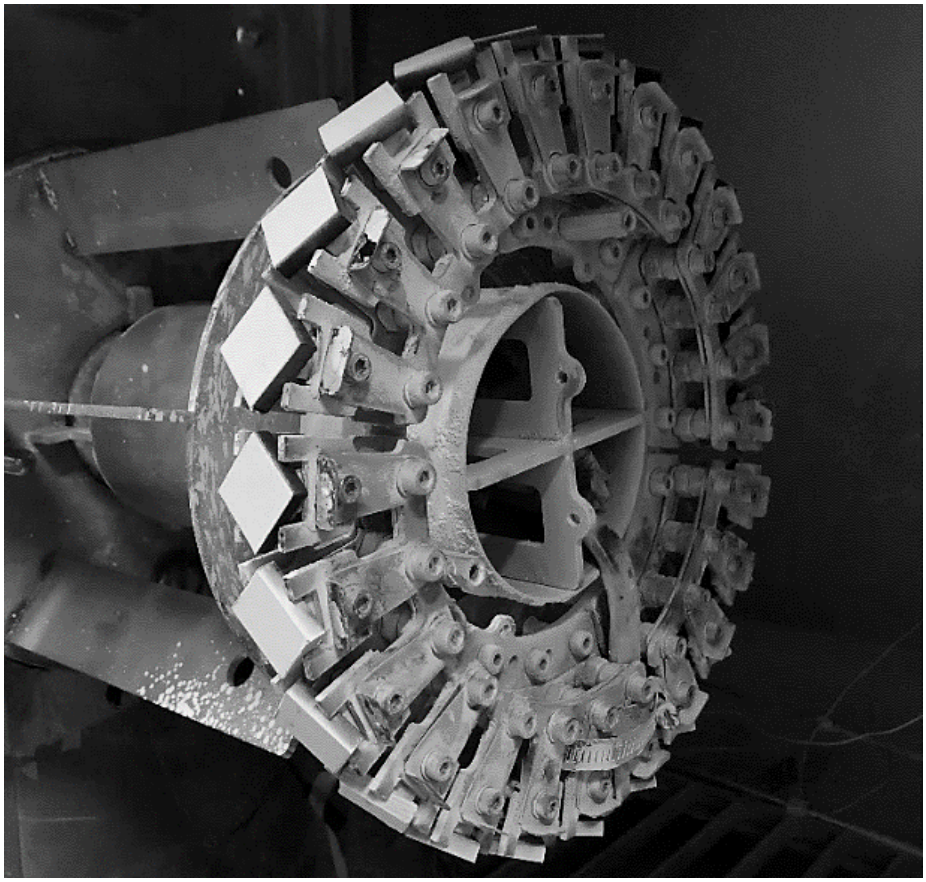

Figure 3-6 Fabricated alumina samples mounted on a rotating sample holder prior to Ni-20Cr deposition.

Table 3-2 Suspension plasma spraying parameters for deposition of alumina.

Parameters \ *Coatings*	*SPS (1)*	*SPS (2)*	*SPS (3)*
Total Gas Flow (TGF) [l/min]	230	280	180
Argon Volume [%]	80	40	45
Nitrogen Volume [%]	10	40	45
Hydrogen Volume [%]	10	20	10
Carrier (slpm)	15	15	15
Solution Feed Rate [ml/min]	45	100	45
Current (A)	180	180	180
Robot Speed [mm/s]	1000	1000	1000
Stand-Off Distance (SOD) [mm]	75	90	75
Number of Passes	30	4	28
Number of Preheating Passes	6	4	6
Power (kW)	69	111	90

3.4. Deposition of Heating Element Coatings

To deposit the resistive heating layer (Ni-20Cr) on the alumina coatings, two different thermal spraying techniques, namely HVOF and APS, were employed. The same Ni-20Cr powder was employed in both processes. The powder was fed to the HVOF gun (Water-cooled Diamond Jet, Oerlikon Metco, Westbury, NY, USA) by using a powder feeder (9MP-DJ, Oerlikon Metco, Westbury, NY, USA). As can be observed in Table (3-3), two spraying conditions with different ratios of oxygen to fuel were determined for this process. One ratio is set to be the exact

stoichiometric ratio of propylene combustion (4.7) and the other ratio was selected based on a lower oxygen/fuel ratio (3.5) to assess their impact on oxide content and microstructure of the fabricated coatings.

Table 3-3 HVOF spraying parameters for deposition of Ni-20Cr on flat samples.

Coatings / ***Parameters***	**HVOF (1)**	**HVOF (2)**
Propylene flow [SLM]	85	70
Oxygen flow [SLM]	300	330
Air pressure (gas carrier) [SLM]	355	355
Powder flow rate [SLM]	20	20
Robot speed [mm/s]	1000	1000
Stand-off distance (SOD) [mm]	200	200
Number of passes	6	6
Number of preheating passes	2	2

For the APS process, powder particles were transferred from an AT-1200 rotary powder feeder (Thermach Inc., Appleton, WI, USA) to the plasma torch (3MB, Oerlikon Metco, Westbury, NY, USA) by using an argon carrier gas. Detailed spray parameters are shown in Table (3-4).

Table 3-4 Air plasma spraying parameters for deposition of Ni-20Cr on flat samples.

Parameters	***Value***
Argon (primary gas) flow rate [L/min]	73
Hydrogen (secondary gas) flow rate [L/min]	4.5
Carrier gas (argon) flow rate [L/min]	9
Feed rate [g/min]	22
Plasma voltage [V]	60
Spray distance [mm]	85
Plasma gun traverse speed [m/s]	1

3.5. Coating Characterization

3.5.1. Morphology and Microstructural Characterization

Multi-layered samples of the coatings were cut using a Secotom 15 precision cutting machine (Struers, Cleveland, OH, USA) and were cold-mounted in an epoxy resin (Epofix, Struers, Cleveland, OH, USA) for microstructural characterization. A Tegramin automated grinding and polishing system (Struers, Cleveland, Ohio, USA) was used to comprehensively grind and polish the samples to get a mirror-like surface suitable for further analysis. Field emission gun scanning electron microscope (JEOL JSM-7600F, Tokyo, Japan) was employed for microstructural examinations. To prevent the accumulation of static electric charges on the non-conductive alumina coating during the examination process, samples were coated with a thin layer of gold. Image analysis software (ImagePro, Media Cybernetics, Bethesda, MD, USA) was used to measure the porosity of the deposited coatings. At least five different SEM images (n = 5) were

used to calculate an average porosity percentage for each coating. To measure the roughness of the coated samples and to acquire a 3D topography imaging a 3-D Confocal Laser Scanning Microscope (CLSM) (LEXT-OLS4000, Olympus Corporation, Japan) was used.

3.5.2. Raman Spectroscopy

The same polished samples were used to perform Raman spectroscopy at room temperature by using a Renishaw inVia spectrometer (Renishaw, Wotton-under-Edge, UK). Phase composition and crystallinity of each sample can be measured by this process. A laser wavelength of 532 nm and objective magnification of 50× was utilized to measure the excitation vibration of each alumina sample. Scanning was done from 100 to 1000 cm^{-1} wavenumber shift. All measurements were done at low excitation measurements of less than 10 mW to prevent samples from overheating. Both Raman spotting and mapping were conducted to assess small and large surface of each sample.

3.5.3. X-ray Diffraction Analysis

X-ray diffraction (XRD) measurements were carried out by using X-ray diffractometers (Bruker D8-Discovery, Bruker AXS, Madison, WI, USA, and Philips X'Pert Pro, Malvern Panalytical, Westborough, MA, USA). Crystallinity and phase purity of the fabricated alumina samples were determined with a copper anode. A graphite monochromator was used to filter K-alpha wavelength radiation (λ = 1.54056 Å). The 2θ diffraction angle was between 10° and 90° at a scanning rate of 0.02 degree/min and a dwell time of 1 second. To find the position of the peaks and to determine the phase associated to each pattern, X'Pert High Score plus (PW3212) software was utilized. Furthermore, the Rietveld technique was employed to quantitatively analyze the identified phases.

3.5.4. Alternating Current Breakdown Voltage Test

A BAUR DTA 100 C tester (BAUR GmbH, Sulz, Austria) was used to study the alternating current breakdown (ACBD) strength of the alumina layers individually and within the multi-layered heating system. All measurements were conducted in air without using an electrically insulating oil. Oil immersion of thermally sprayed samples when conducting the ACBD test is reported to exhibit significantly higher values which is mainly caused by the porous structure and moisture sensitivity of thermally sprayed coatings [86].

Measurements were based on the ASTM D149–09 (2013) standard. The coated coupons were placed between two ball-tip electrodes with a diameter of 4 mm. Based on each sample's thickness, the distance between the two electrodes was adjusted. An increasing voltage of 2 kV/s at 60 Hz frequency was applied to each specimen. The reported values were calculated from an average of 10 trials from each sample (n = 10), including alumina coating with and without the top Ni-20Cr heating element. The dielectric strength (kV/mm) was calculated from the ratio of the breakdown voltage to the coating thickness which is equivalent to an intrinsic property of a material independent of its thickness or configuration. The assembly used for measuring the breakdown voltage values is shown in Fig. 3-7.

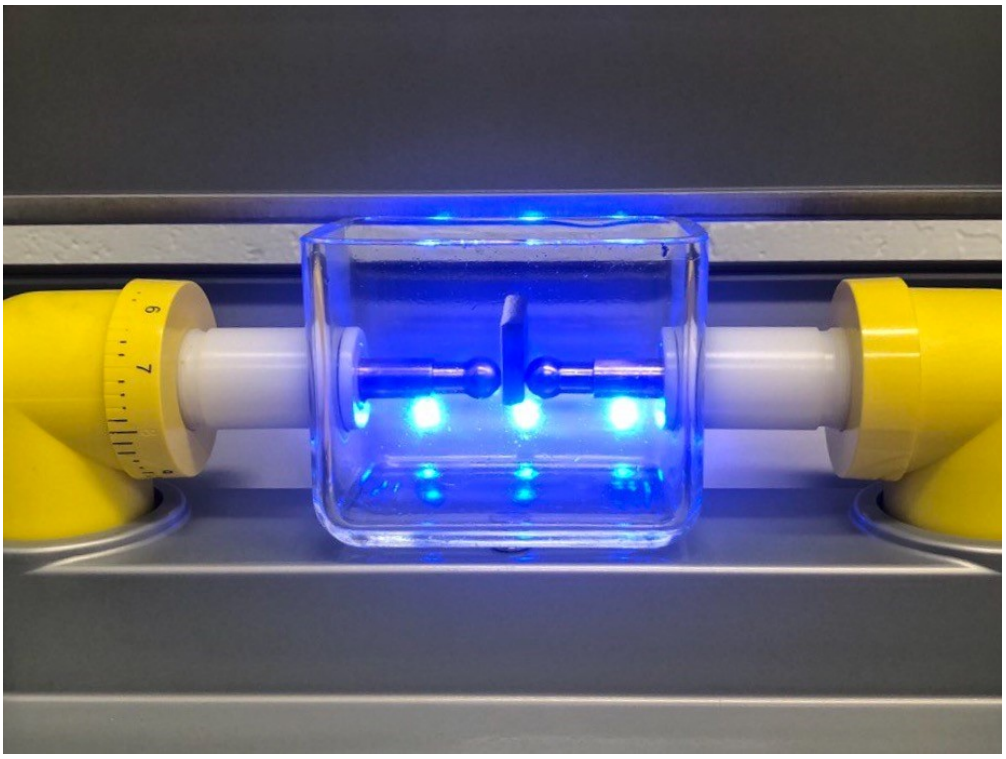

Figure 3-7 The set-up used for dielectric breakdown voltage test.

3.5.5. Adhesion Strength Test

A PosiTest™ AT Automatic Tester was manufactured by DeFelsko (AT-A, Ogdensburg, NY, USA) [107]. This device measures the required force to delaminate a specified test diameter of coating by using hydraulic pressure. Posi-Test adhesion tester conforms with international standards such as ASTM D4541, D7234, ISO 4624, and others [108]. The adhesion strength of the coated samples was equivalent to the highest tensile force that was required to remove the coating from the substrate. Failure points are observed along the weakest plane within the system that consisted of the dolly (loading fixture, stub), glue, coating layer and the substrate. In this study 20 mm aluminum dollies and the Devcon No.19770 'plastic steel' two-part epoxy (Model 19770, Aurora, OH, USA) were employed. Depending on the required pressure, dollies with diameters of

10, 14, and 50 mm could also be used. All pull tests have a resolution of 0.01 MPa (1 psi) with an accuracy of ± 1%. In this study, dollies with 10 mm diameters were employed that as reported by the manufacturer can tolerate pull-off pressures as high as 95 MPa.

The base of the dollies was grit blasted with a #80 alumina grit size to remove oxidation and contaminants and to increase the roughness for better adhesion. The glue was mixed based on the manufacturer's instructions. A thin, uniform layer of glue was applied to the base of each dolly. Then, the dollies were attached to the prepared coating test area. The samples were left at room temperature for twelve hours to reach maximum strength prior testing. The test configuration is shown in Fig. 3-8.

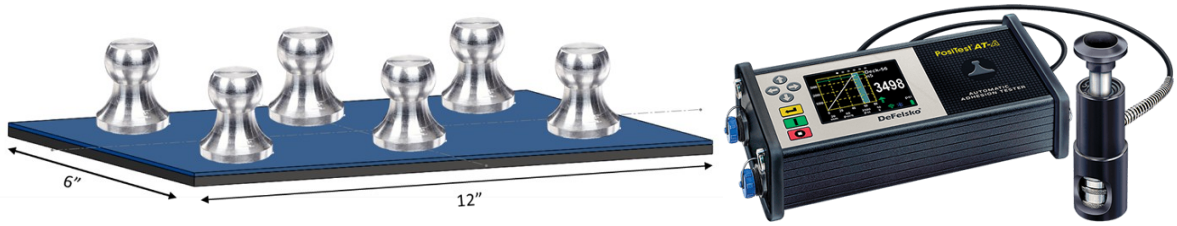

Figure 3-8 PosiTest™ AT pull-off test device and the used set up

Chapter 4. Results and Discussion

As it was mentioned in the previous chapter, multi-layered heating systems were fabricated by using several thermal spraying techniques. Alumina dielectric layer was deposited by using two processes, namely, FS and SPS. Consequently, the alumina layer was coated with Ni-20Cr by using HVOF and APS processes. Several combinations of the alumina - Ni-20Cr was used to produce the multi-layered heating systems. It should be noted that the FS-sprayed alumina and FS-sprayed Ni-20Cr coatings were all prepared at University of Alberta. That said, this chapter is divided into three main sections with the following structure: First, the produced alumina dielectric layers and the resultant phase composition, microstructure, mechanical properties, and roughness are discussed in detail. Then, different combinations of the deposited alumina layers with the Ni-20Cr heating layer is reported and their microstructure and type of mechanical failure are thoroughly discussed. At last, a comparative report of the dielectric breakdown voltage values of selected heating systems and their performance are reported. It should be mentioned that the focus of this chapter was to study the dielectric strength of alumina samples and the influence of heating element layer deposition on the dielectric alumina layer. Further information on the heating performance of the fabricated heating systems can be found in studies done by Rezvani Rad, *et al.* [63, 106].

4.1. Alumina Coatings

4.1.1. Coating Characterization

Scanning electron microscopy (SEM) images from the top surface of the FS and SPS alumina coatings which were taken in secondary electron mode are shown in Fig. 4-1. The size distribution of the alumina powder particles used in the FS process was in the range of 5 to 45 μm and could be a possible reason for the presence of open pores on the top surface of the FS alumina during the microstructural evaluation. It can be seen from the higher magnification image (1000×) that these pores are not superficial and some of them are in fact, interconnected. These open pores can be a pathway for the penetration of the top heating element which will lead to a reduction of the effective thickness of the electrically insulating layer. On the contrary, SPS alumina samples exhibited a different surface structure. Top surface of the SPS alumina can be seen in Fig. 4-1 (c) and (d). A cauliflower-like structure can be observed, which is much denser compared to the FS alumina top surface and can prevent the molten Ni-20Cr particles from penetrating in the insulating layer.

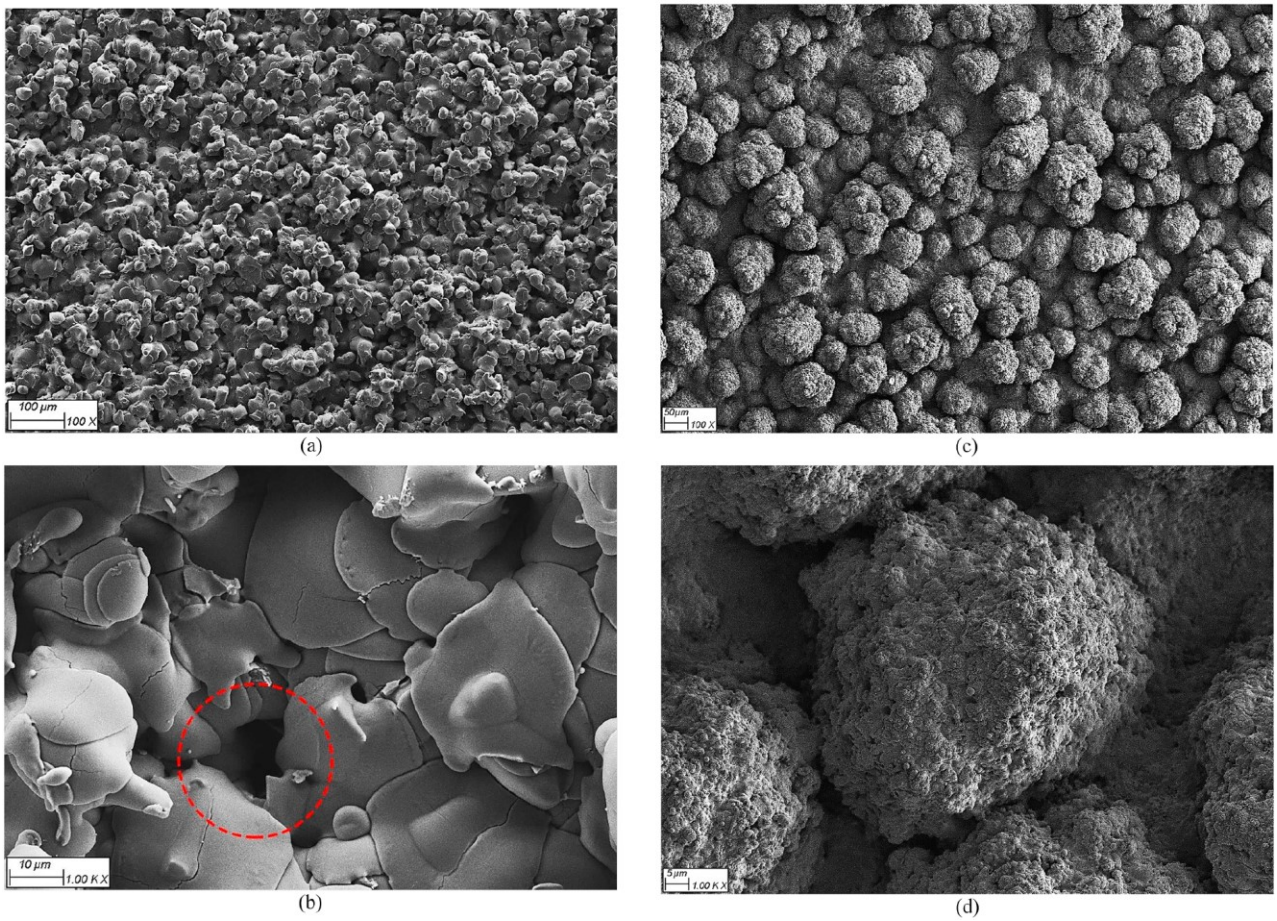

Figure 4-1 Secondary SEM images from top surface of alumina samples at 100× and 1000× magnifications; (a)-(b) FS alumina and (c)-(d) SPS alumina [106,109].

Figures 4-2 and 4-3 show the micrographs taken from the FS (1) alumina – APS Ni-20Cr and FS (2) alumina – APS Ni-20Cr coatings, respectively. The pores within the alumina coatings are represented by the darker regions. At least five different SEM images (n = 5) were utilized to calculate the average porosity of 13% for FS (1) and 21% for FS (2) alumina samples. The standard error on the mean of all porosity measurements were reported to be approximately 0.5. FS (2) contains a higher amount of porosity compared to the FS (1) sample which is believed to be due to the increase in the fuel to oxygen ratio from 0.6 for FS (1) to 0.8 for FS (2). The lower the porosity, the better the melting of particles that leads to formation of flatter splats. Non-

homogeneous dispersion of large pores was detected in both FS alumina samples. This observation could have been mainly due to the presence of particles that were either fully or partially melted upon deposition.

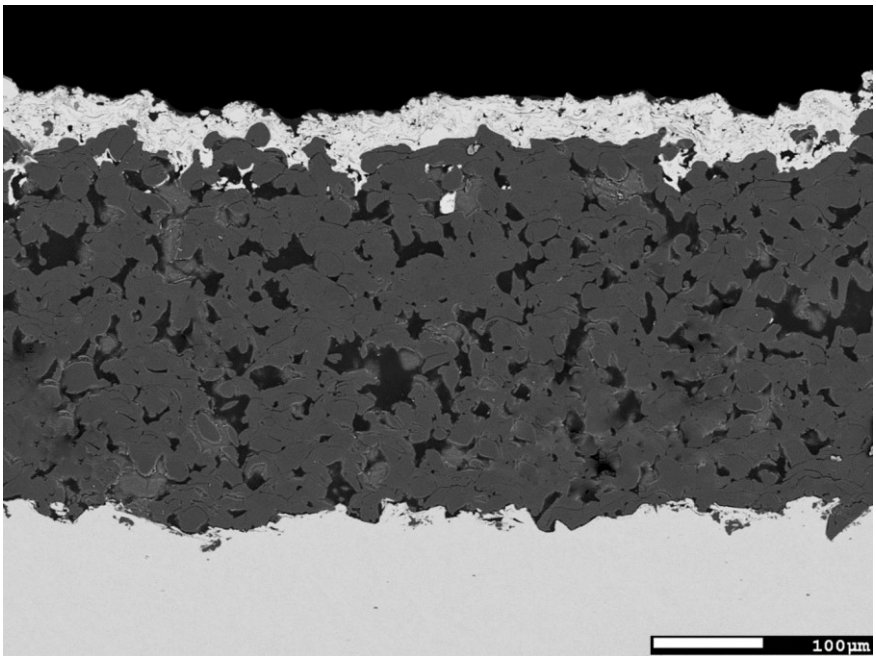

Figure 4-2 Backscattered SEM image of the cross section of the coating system composed of FS (1) alumina and APS Ni-20Cr.

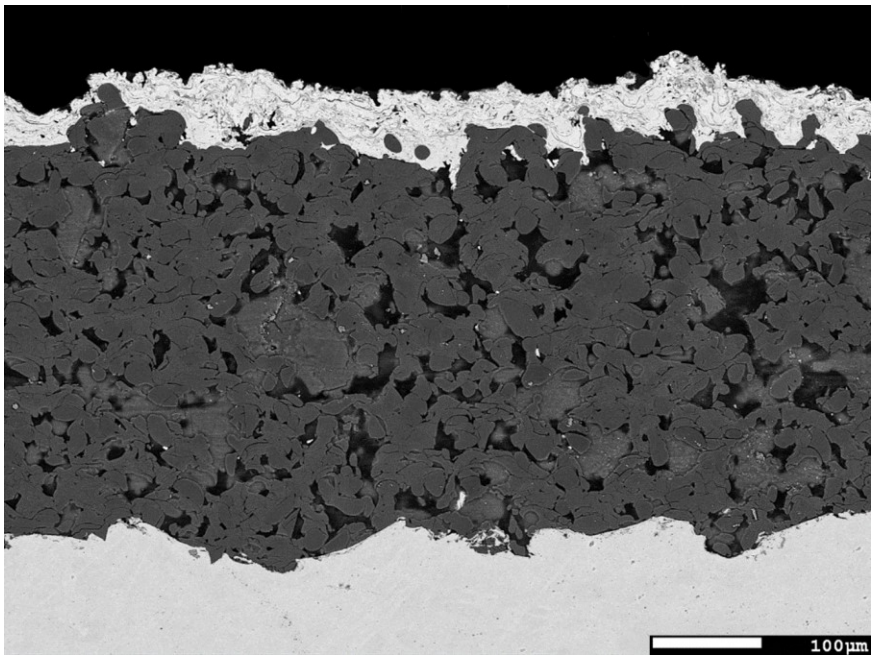

Figure 4-3 Backscattered SEM image of the cross section of the coating system composed of FS (2) alumina and APS Ni-20Cr.

Various alumina microstructures (porous, columnar-like, and dense) were achieved through utilization of the suspension plasma spraying method. The porous, dense, and columnar-like alumina microstructures that were obtained from the SPS (1), SPS (2), and SPS (3) spraying conditions can be observed in Figs. 4-4 to 4-6, respectively. A relatively low power of (69 kW) was used to fabricate SPS (1) samples with a high porosity of 25%. The SPS (3) spraying condition (90 kW) led to the formation of a dense and columnar-like alumina microstructure. Both SPS (1) and SPS (3) had the same suspension with solid content of 10 wt. % and the same stand-off distance as shown in Table 3.2. In the SPS (2) spraying condition, the highest plasma power of 111 kW and suspension with a higher solid concentration of 25 wt. % reduced the alumina porosity (10%) which was mainly due to complete melting of the alumina feedstock. In the SPS samples, even

though the amount of porosity is greater compared to the FS alumina coatings, the pores are finer and are distributed evenly in the coatings cross-sections.

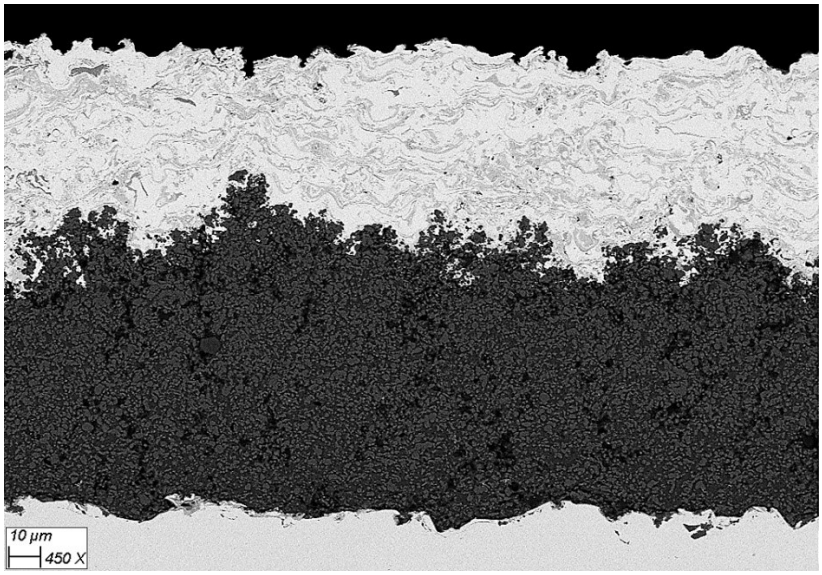

Figure 4-4 Backscattered SEM images of coating systems composed of SPS (1) alumina and HVOF Ni-20Cr with porous structures [106].

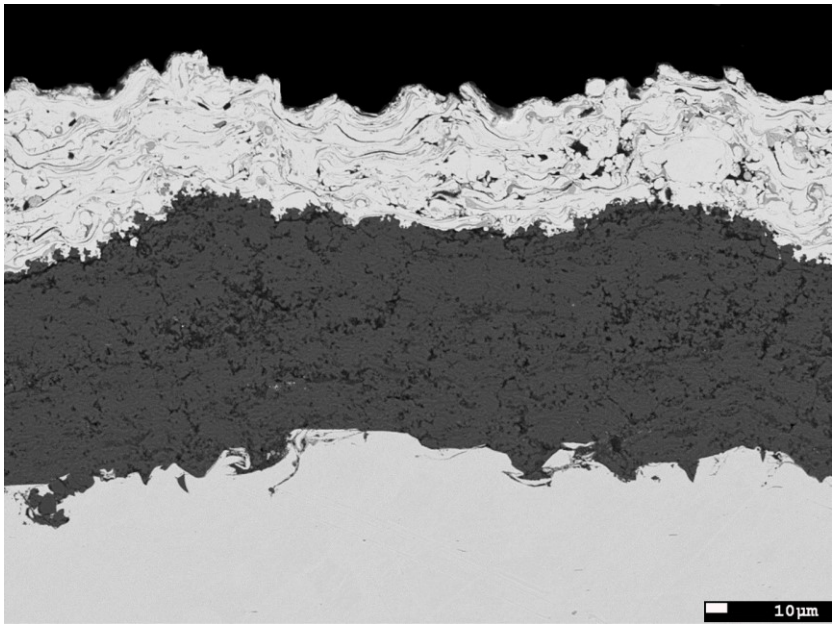

Figure 4-5 Backscattered SEM image of the cross section of the coating system composed of SPS (2) alumina and APS Ni-20Cr.

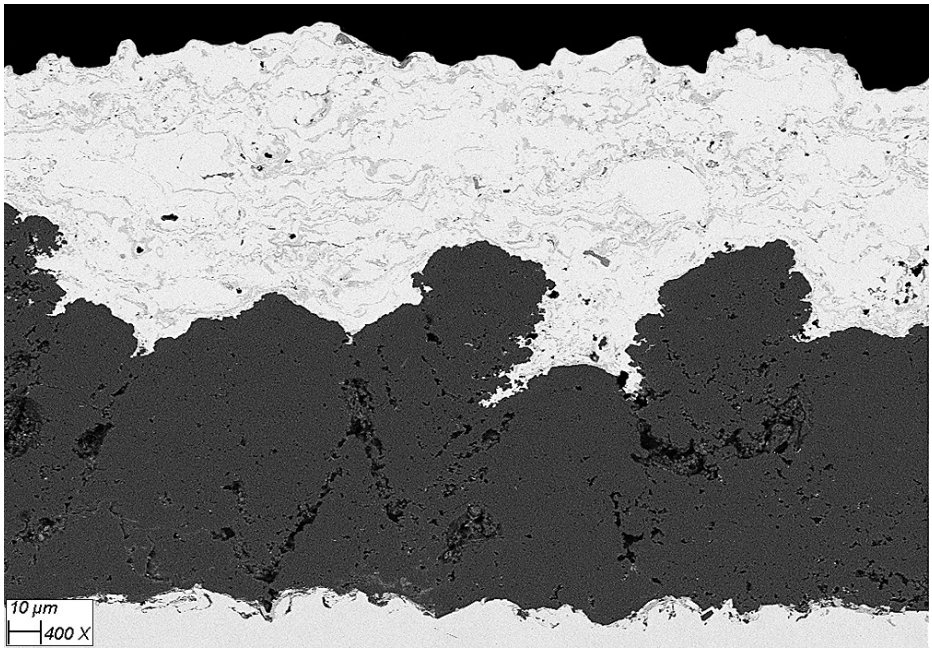

Figure 4-6 Backscattered SEM images of coating systems composed of SPS (3) alumina and HVOF Ni-20Cr with cauliflower-like structures [106].

4.1.2. Phase Composition

X-ray diffraction analysis

Phase composition of FS (1), SPS (1), SPS (2), and SPS (3) alumina coatings was analyzed by using the X-ray diffraction (XRD) analysis and their XRD patterns were compared with their initial powder feedstock (Fig. 4-7). Powders used for both FS and SPS processes were pure α-alumina. However, various proportions of α-alumina and γ-alumina were detected after the spraying process. Rietveld method was used to perform quantitative phase analysis of the deposited coatings and the obtained results are shown in Table 4-1. The content of corundum (α–Al_2O_3) in FS (1) alumina was reported to be 60%. In comparison, the content of α-alumina for the SPS-sprayed coatings varied from 30% to 70% for the dense and porous structures, respectively.

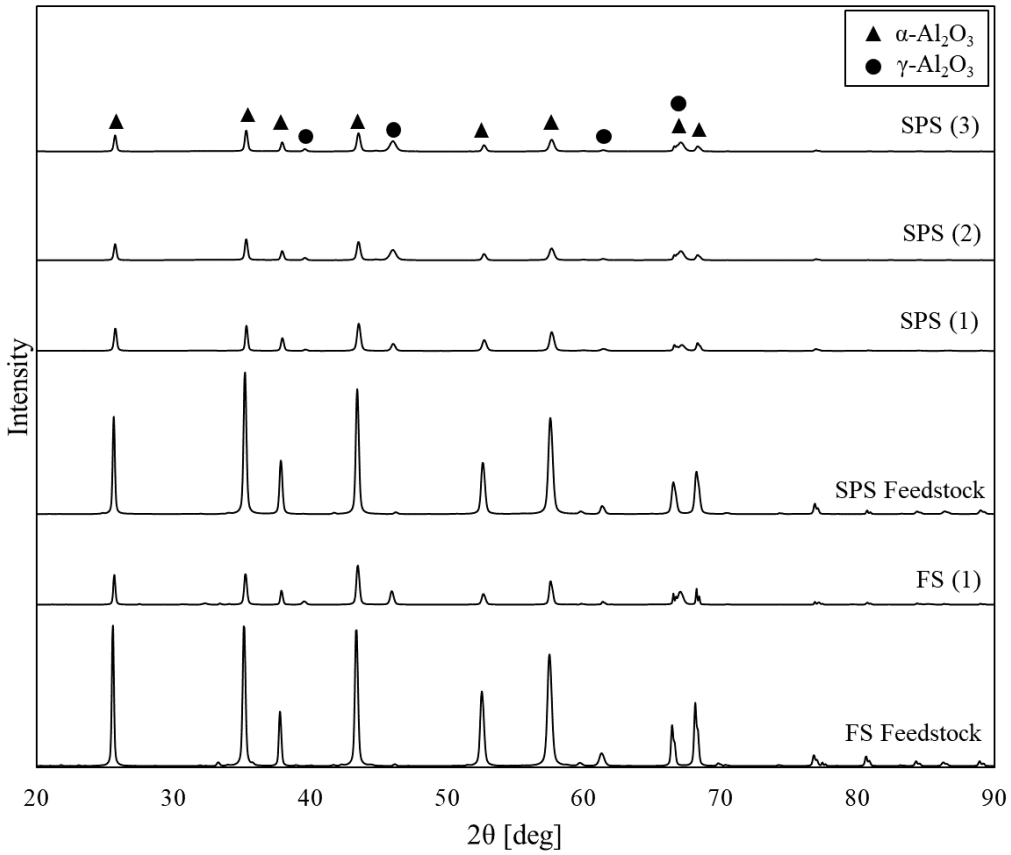

Figure 4-7 X-ray diffractograms of the as-sprayed alumina coatings.

Considering the FS alumina XRD patterns, the extent of melting of in-flight particles and their subsequent cooling rate during the solidification stage was most likely the reason for formation of different percentages of the stable alumina phase that exhibits better hygroscopic properties than the unstable gamma phase. During the FS process, particles are relatively larger compared to the submicron sized SPS feedstock. In the case of FS powder, the particles most likely go through partial melting that results in the presence of both α–Al_2O_3 and γ–Al_2O_3 phases in each particle. However, in the case of SPS, the particles are so small that they either completely melt or not melt at all.

Table 4-1 Quantitative results regarding the phase composition of feedstock powder and the deposited coatings obtained by Rietveld method [109].

Sample name	α–Al_2O_3 (%)	α–Al_2O_3 crystallite size (nm)	γ-Al_2O_3 (%)	γ–Al_2O_3 crystallite size (nm)
FS Al_2O_3 feedstock	100	160	0	--
FS (1) Al_2O_3	61	2800	39	26
SPS Al_2O_3 feedstock	100	50	0	--
SPS (1) Al_2O_3	70	56	30	13
SPS (2) Al_2O_3	51	70	49	25
SPS (3) Al_2O_3	34	47	65	12

The α-alumina phase was the major constituent phase of the SPS (1) alumina and there are three possible reasons behind this phenomenon as reported by Müller, *et al.* [91]. First, it is probable that some particles did not melt at all during the SPS process. Second, the relatively short stand-off distance value that was selected for SPS deposition (75 mm) could also have had an influence on the amount of alpha phase. During spraying the sample is constantly heated and the cooling rates are much slower, therefore the formation of the α-alumina phase is possible. Lastly, resolidification of the in-flight alumina particles with lower cooling rates has also been reported to be a possible reason for formation of α-alumina phase [91].

It is well established that the γ-Al_2O_3 is a defective spinel structure that is formed at temperatures between 400 – 700°C. γ–Al_2O_3 will convert to α–Al_2O_3 at temperatures higher than 1000°C [111]. During spraying, even though care was taken to keep the overall surface

temperature under 500°C, due to the low stand-off distance between the coating surface and the torch, the torch locally heated the surface for a short time and this can be another possible reason for transformation of gamma phase to the alpha phase in the SPS process. Especially as the coating is getting thicker, less heat transfer towards the substrate will make the surface temperature even higher. For the case of SPS (3), the chosen spraying parameters gave rise to a higher temperature for the plasma flame, thus the obtained dense microstructure was most likely due to complete melting of a higher portion of the sprayed particles. That said, cooling rate of the particles upon solidification was relatively higher that eventually resulted in 70% of γ-alumina phase in the deposited alumina coating.

The mean crystallite size of the prepared coatings and their initial feedstock was also calculated with the Rietveld analysis and is reported in Table. 4-1. The crystallite size of the FS-sprayed alumina has significantly increased compared to its powder form. One possible explanation for this observation can be the lower spraying speed in the FS process compared to the SPS process. During the FS process, when fully molten particles are impinging on the substrate the deposited splats have a higher thickness relative to the splats deposited by the SPS process that has a higher spray velocity. Therefore, the cooling rate in the FS process is much lower which will favor the grain growth in the FS alumina. Furthermore, unmelted powder particles that are heated to a temperature close to their melting point, experience heat treatment for a very short time that could also favor the grain growth.

Raman Spectroscopy

Raman scattering was carried out on FS (1), FS (2), SPS (1), and SPS (2) alumina coatings to study their chemical structure, composition, and formed phases after deposition. To consider possible effects of Ni-20Cr deposition on the phases developed in the alumina layer, the Raman

spectroscopy was conducted on the alumina layer within the multi-layered system. As previously observed in the SEM images of FS alumina samples, apart from the difference in the amount of porosity, the microstructures of both FS samples were quite similar and resulted in similar Raman spectra. That said, the data obtained from only FS (1) alumina is reported. Spot measurements were taken from each region (Fig. 4-8) and Raman mapping was also performed on an area containing both regions (Fig. 4-9). Two distinct regions are observed in the FS-sprayed samples as indicated in Fig. (4-9 (a)). Region 1 corresponds to the center of a particle and has a brighter color, and Region 2 can be related to either unmelted particles or porosity.

It was found that pores did not produce a structured Raman spectrum and only generated a fluorescent background of various intensities. It has been reported in the literature that neither gamma nor eta alumina give rise to any Raman bands [112, 113]. The only Raman band observed in Region 2 spectra was at 642 cm^{-1} that in some studies has been reported to be attributed to Fe^{+3} impurities and its fluorescence [111]. α-Al_2O_3 has several optical bands that a representation of them are given as follows: $2Al_g + 2Al_u + 3A2_g + 2A2_u + 5E_g + 4E_u$

$2Al_g + 5E_g$ are the Raman active modes, $2A2_u + 4E_u$ are IR active modes, and $2Al_u + 3A2_g$ represent neither Raman nor IR modes [114]. α-Al_2O_3 gives rise to seven Raman active phonon modes at frequencies of 378, 418, 432, 451, 578, 645 and 751 cm^{-1} [115]. Raman bands with peaks at approximately 378, 432, 451, 578, and 751 cm^{-1} are assigned to E_g (external), and 418, 645 cm^{-1} peaks are associated with the Al_g modes [116]. By comparing the spectra of Regions 1 – 2, one can conclude that the initial α-Al_2O_3 (corundum) is retained at the center of each particle and as we get closer to the dark regions, the intensity of the peaks decreases which can be related to hollow pores within the material or formation of γ-Al_2O_3 at the edges of each particle where it is

partially melted. The fact that the gamma phase does not give rise to any Raman bands has made it difficult to distinguish between gamma phase and porosity.

Raman mapping was conducted based on the 415 cm^{-1} Raman band, which is mainly present in the corundum spectra. Regions where this phase is present is demonstrated in red. By comparing the original image (Fig. 4-9 (a)) with the Raman map image, it can be observed that the intensity of the red color has decreased in some regions that have been indicated by the arrows. These regions are still in the light regions but the intensity of the α-Al_2O_3 is relatively weak. Consequently, the areas that have been indicated with the arrows can most likely be related to γ-Al_2O3. This assertion is also confirmed by the difference in density of both alumina phases. γ-Al_2O_3 monoclinic phase has the density of 3.56 g cm^{-3}, while α-Al_2O_3 hexagonal phase has a higher density of 3.98 g cm^{-3} [117]. Higher density of the alpha phase may be the reason for brighter regions.

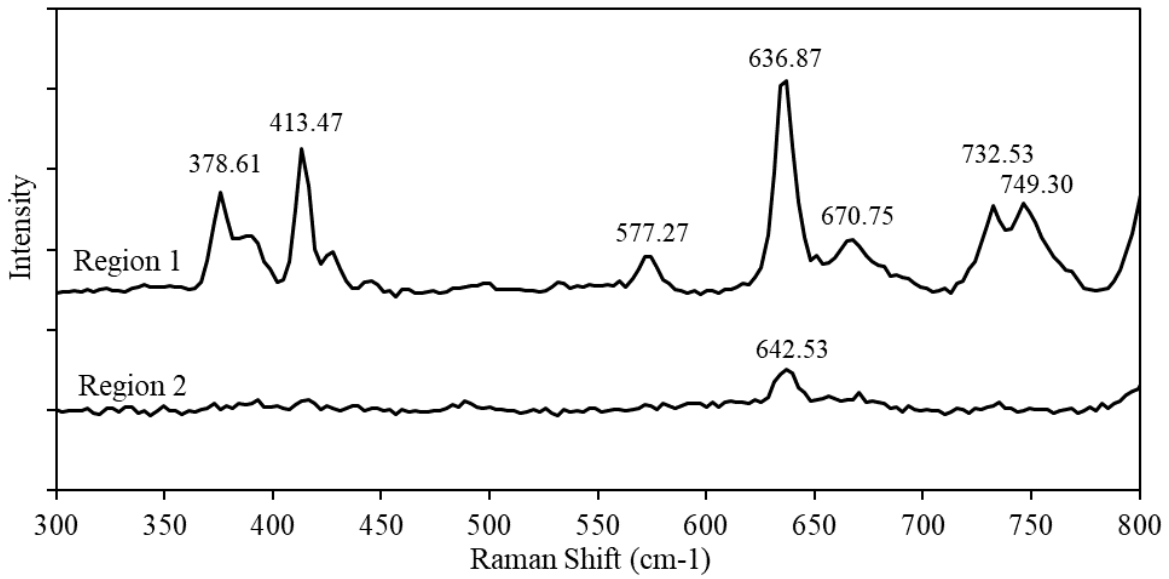

Figure 4-8 Raman spectra of FS (1) alumina recorded at two different regions as indicated in Fig. (a).

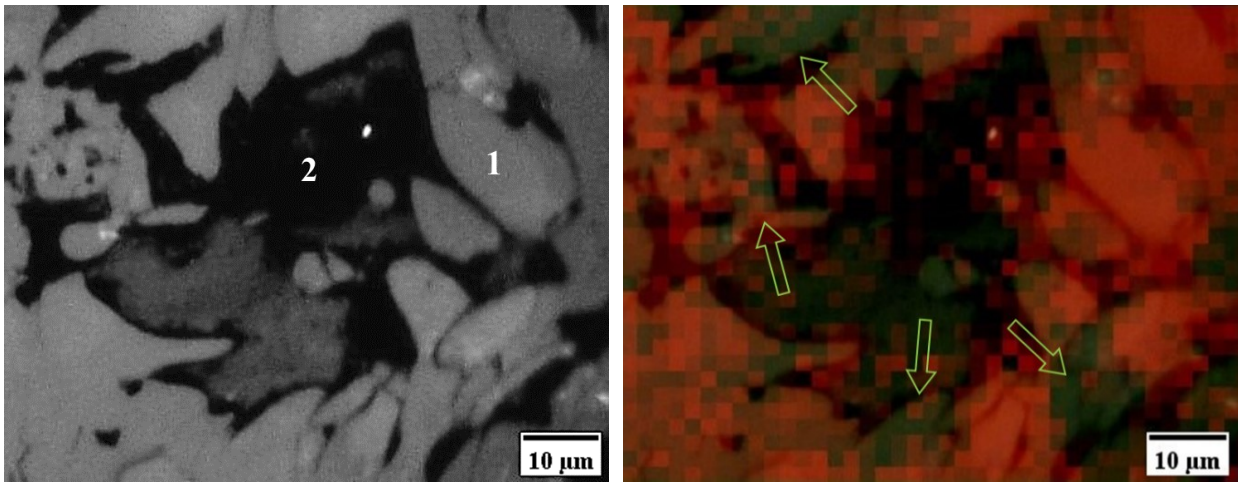

(a) (b)

Figure 4-9 Representative (a) Raman mapping of FS (1) alumina showing the selected area, (b) distribution of α-Al_2O_3.

As previously shown in SEM images of SPS (1) and SPS (2) alumina samples, both coatings consisted of two main regions: (1) the melted particles (bright regions) and (2) porosity or unmelted particles (dark regions). As observed in Fig. 4-10, Raman spectra of SPS (1) gave rise to the Raman bands that are associated with the alpha phase. On the other hand, SPS (2) Raman spectra did not show any peaks at all which is most likely because of the high percentage of the gamma phase. Several spots were measured to get the Raman spectra from both bright and dark regions, but no significant difference was observed in each spectrum. The Raman spectroscopy device had the spatial resolution 1 µm and spectral resolution 0.5 - 1.0 cm^{-1}. It seems that the resolution of the device was not high enough to be able to discriminate between different spots.

It can be observed from SPS (1) spectra, that a higher portion of the particles were not melted and has let to retention of the alpha alumina within the coating. Given the obtained Raman spectra, it is believed that the co-existence of both phases in both regions in SPS (1) alumina is possible. It can be seen in the SPS (2) alumina Raman spectra that the denser microstructure

transformed the initial alpha alumina to gamma alumina. This observation is also in line with the XRD results.

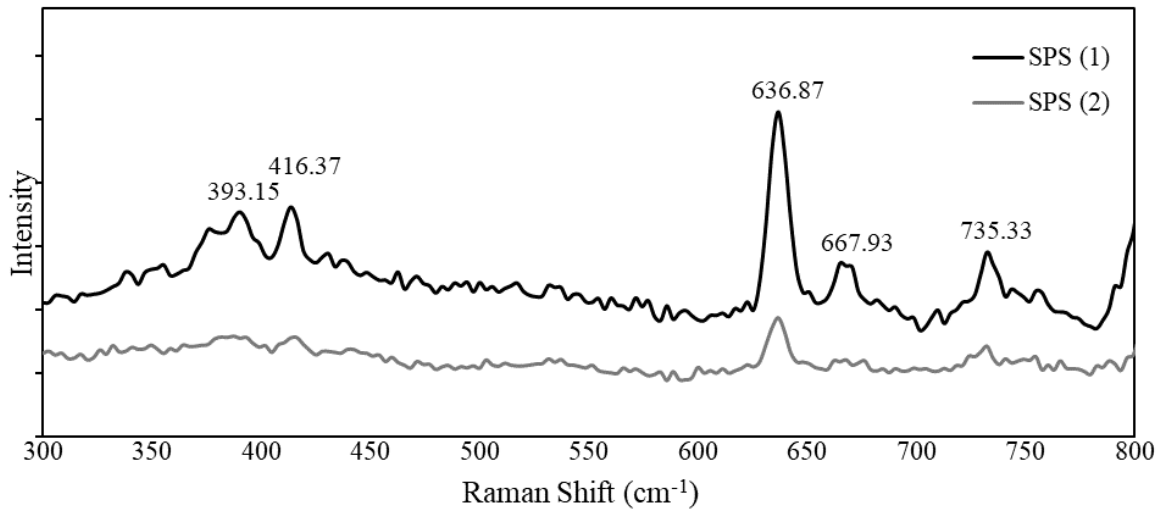

Figure 4-10 Raman spectra of SPS (1) and SPS (2) alumina recorded at dark and bright regions.

4.1.3. Adhesion Strength

Adhesion strength tests were conducted on large plates coated with FS (1), SPS (1), and SPS (3) spraying conditions. A small droplet of the mixed glue was applied at the center of the bottom surface of each grit blasted dolly (Fig. 4-11). As it is indicated, at least six measurements were taken from each plate. The dollies were placed at certain locations to minimize their impact on one another during pull test. The obtained data from all performed adhesion tests are reported in Fig. 4-12. The error bars indicate the standard deviation that measures the variation of the adhesion strength values from their mean value.

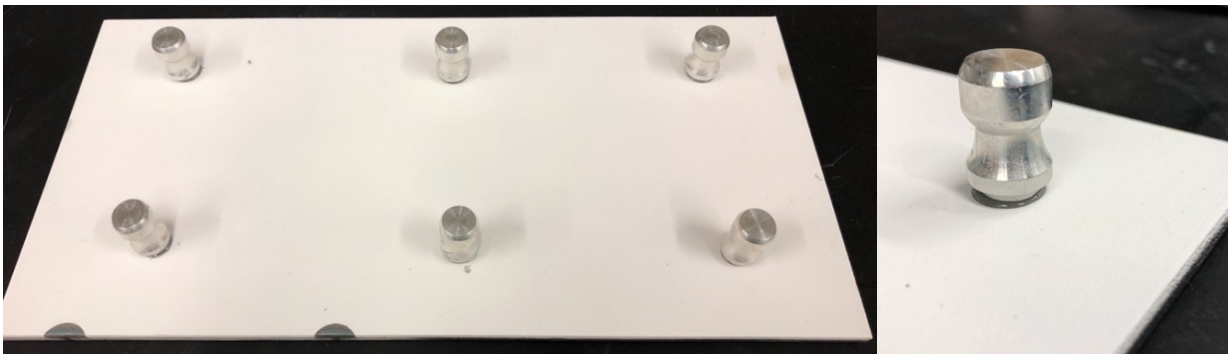

Figure 4-11 Adhesion strength pull-test set-up

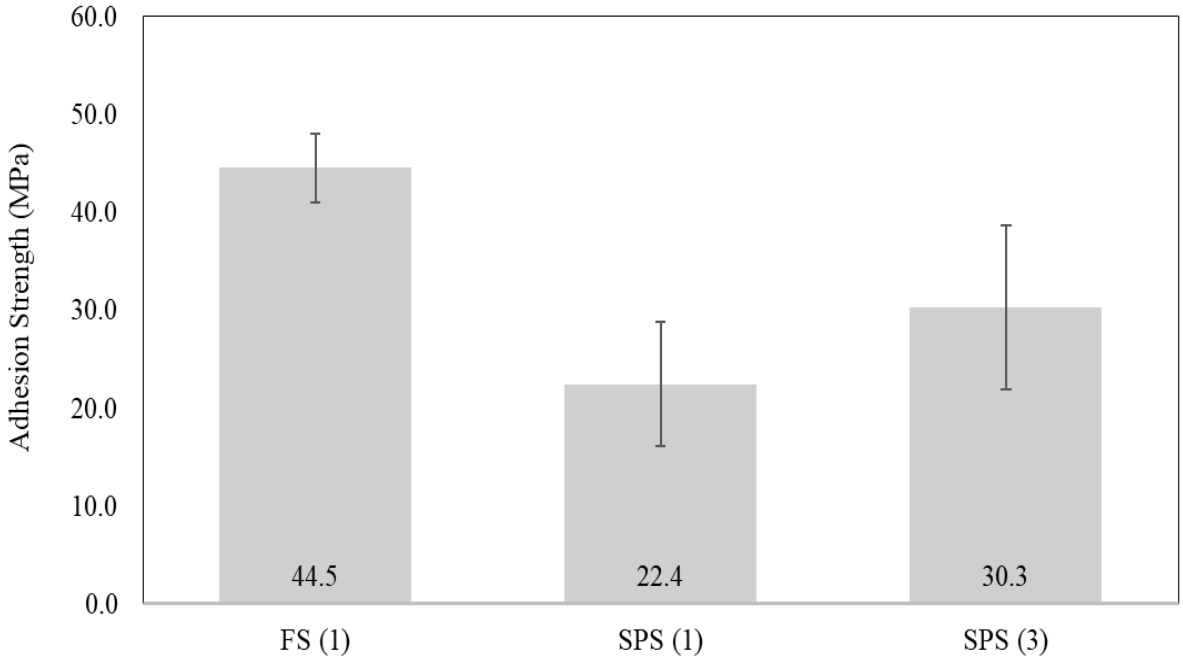

Figure 4-12 Adhesion strength as a function of thermal spray deposition method

The FS (1) alumina resulted in the highest adhesion strength of 44.5 MPa. As observed in Fig (4-13 (a)), after testing, the failure seemed to be from the glue. The dollies got completely detached from the glue and after testing, the layer of glue was remaining on the sample. Regarding the SPS samples, inconsistent failure types (both cohesive failure in the coating and adhesive failure at the glue) were observed which can be related to the cauliflower-like surface of SPS

samples and uneven distribution of the glue between the dolly and the SPS-sprayed alumina samples. SPS (1) alumina with the highest amount of porosity exhibited the lowest adhesion strength among the other two samples. The SPS (3) alumina that had a dense structure with deep valleys between each column resulted in the highest standard deviation. This assertion is also confirmed by the roughness values that were measured from confocal microscopy (Fig. 4-14). The SPS (3) alumina had the highest roughness values which could be a possible reason for variation in the collected data.

(a) (b)

Figure 4-13 Different types of failure after conducting the adhesion strength tests. (a) FS (1) alumina, (b) SPS (1) alumina.

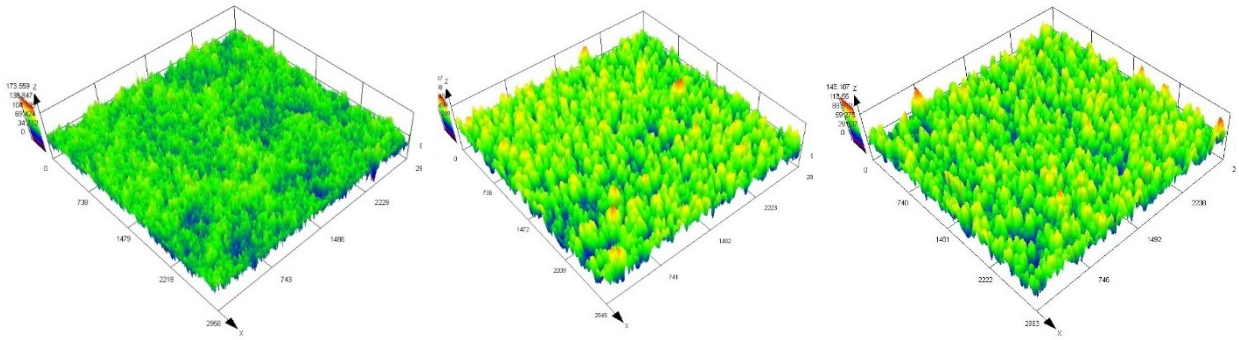

FS (1) R_a= 10.6 ± 0.2 µm **SPS (1)** R_a= 9.4 ± 0.3 µm **SPS (3)** R_a= 12.7 ± 0.3 µm

Figure 4-14 Roughness values obtained from confocal microscopy.

4.2. Alumina Layer and the Ni-20Cr Heating Element Layer

4.2.1. FS Al_2O_3 – FS Ni-20Cr

As it can be seen in the cross-sectional image of the FS coating system (Fig. 4-15), the FS Ni-20Cr layer penetrated the flame-sprayed insulating layer. This occurrence was most likely due to the presence of relatively large open pores at the top surface of the deposited FS alumina coating. Therefore, the alumina coating layer needs to have a minimum thickness to ensure that the molten Ni-20Cr droplets do not penetrate the underneath layers and cause a short circuit between the heating element and the conductive steel substrate. Both alumina and Ni-20Cr layer in this image were deposited by the FS process at University of Alberta. Further details on this coating system can be found in the study conducted by Rezvani Rad, *et al.* [106].

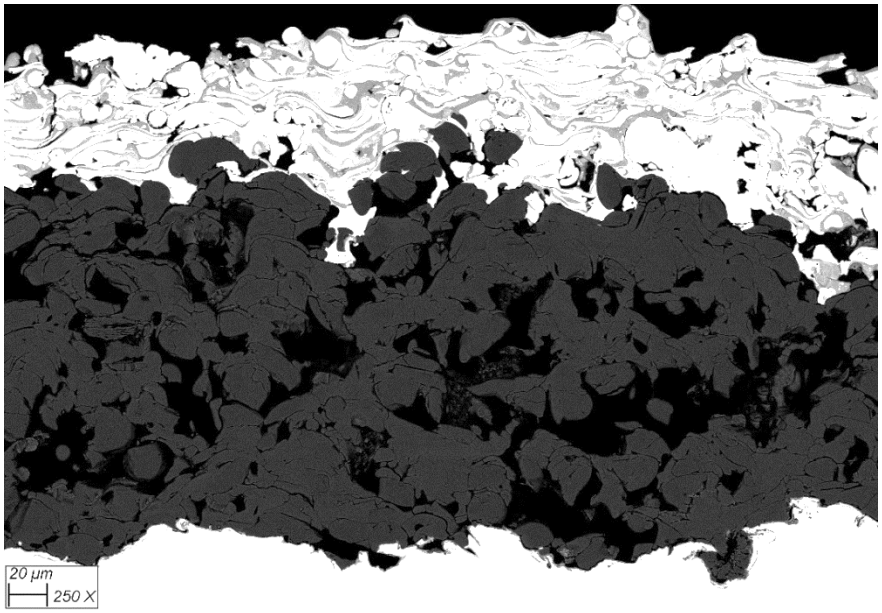

Figure 4-15 Backscattered SEM image of the cross section of the coating system composed of FS alumina and FS Ni-20Cr [106].

The alumina layer employed in a resistive heating system may be prone to mechanical failures due to accumulation of thermal residual stresses at the interfaces with the heating element and the substrate. It is well-established that the brittleness of alumina is one of the most important factors that can limit the usage of this material in engineering applications [110]. The FS (1)-sprayed Al_2O_3 coated with FS Ni-20Cr is shown in Fig. 4-16. As it was also observed in Fig. 4-15, Ni-20Cr has penetrated into the insulating layer and is considered a serious disadvantage from an electrical viewpoint; however, it can be beneficial from a mechanical perspective as it provides interlocking between each coating.

It can be seen in Fig. 4-16 that some minor cracks were present in the as-sprayed FS coating system. The cracks were mainly at the interface of the FS alumina layer and the heating element. In addition, several cracks were also observed within the FS alumina layer that were likely formed

due to the presence of the adjacent pores. However, these cracks did not cause any delamination within the system and all layers were fully adherent to one another.

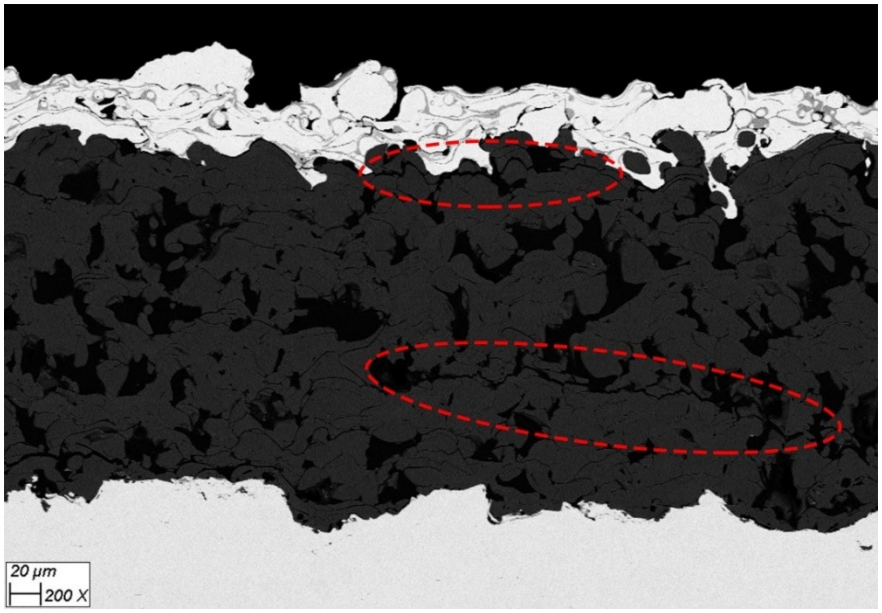

Figure 4-16 Backscattered SEM image of the cross section of the coating system composed of FS alumina and the heating element layer [109].

4.2.2. SPS Al_2O_3 – HVOF Ni-20Cr

The conductive Ni-20Cr coating was deposited by the HVOF process and has resulted in a much denser and more uniform coating compared to the Ni-20Cr coatings deposited by FS. Figure 4-17 shows the microstructure and EDS mapping of the HVOF-sprayed Ni-20Cr coatings. The selected set of spraying parameters for HVOF spraying resulted in different oxide contents. The gray regions observed in Fig. 4-17 (a) and (b), correspond to oxygen-rich regions that were produced during spraying. This was due to the different flame temperature, oxygen content, and portion of powder particles that went through phase transition inside the plume during the deposition process.

It was observed that for the case of HVOF (2) where the ratio of oxygen to propylene was 4.7 (stoichiometric ratio) the generated oxide content was less compared to the HVOF (1) set of parameters in which the oxygen to propylene ratio was 3.5. Higher temperature of the flame in the HVOF (1) condition could have been the main reason that resulted in a higher portion of melting in the in-flight powder particles and have increased the interaction between the molten particles and the air inside the plume during the spraying process.

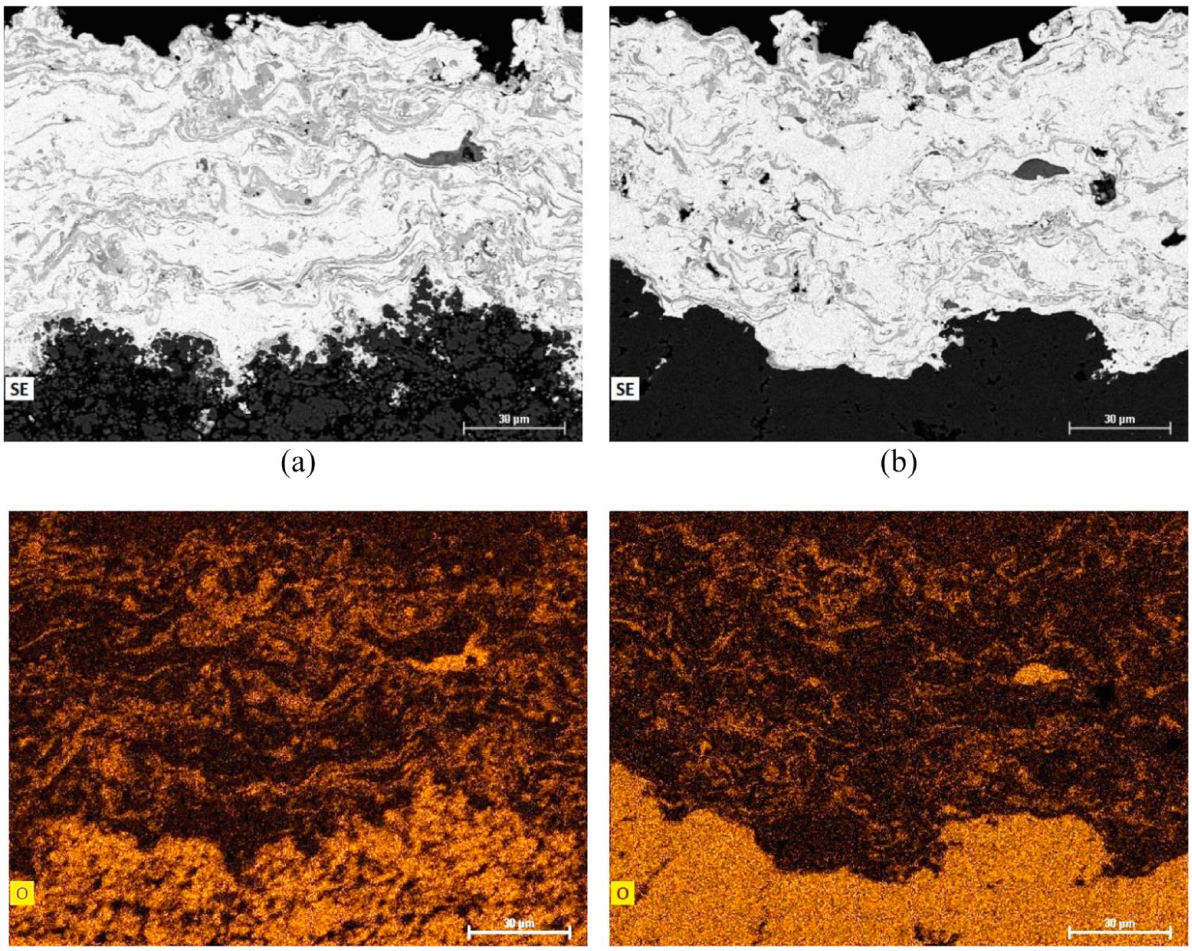

Figure 4-17 (a)-(b) SEM images from HVOF (1) and HVOF (2) Ni-20Cr, and (c)-(d) corresponding EDS mapping images of oxygen [106].

The cross-sectional microstructure of SPS (1) alumina is shown in Fig. 4-18. It can be observed from this image that due to the high porosity of the SPS (1) alumina, several cracks have initiated within the alumina layer, close to the interface of alumina with the Ni-20Cr layer. Imperfect cohesion of the SPS (1) alumina is indicated by the continuous crack grown along the interface of the heating element and the alumina layer. Compared to SPS (1), the alumina layer deposited with the SPS (3) spraying condition resulted in a dense and fully molten microstructure and the adhesion between the alumina layer and the heating element was acceptable (Fig. 4-19). However, minor cracks were detected within the alumina layer that primarily initiated from the gaps between the cauliflower-like columns. In the HVOF process, combustion gasses are accelerated in a jet to supersonic values which could be a possible reason behind the observed mechanical failures in the SPS alumina – HVOF Ni-20Cr coating systems. In order to minimize these challenges, air plasma spraying (APS) was utilized to deposit the heating element layer onto the alumina layer. `

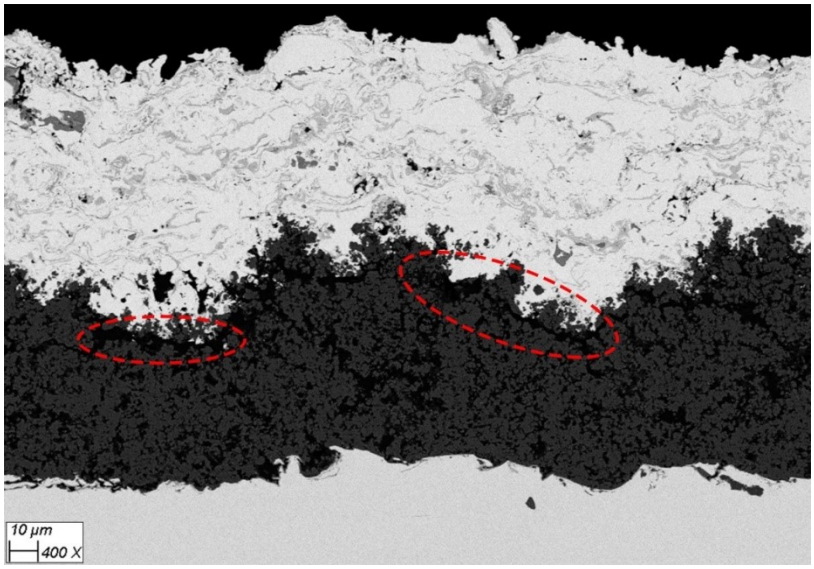

Figure 4-18 Backscattered SEM images of coating systems composed of the heating element layer and SPS (1) with a porous structure [109].

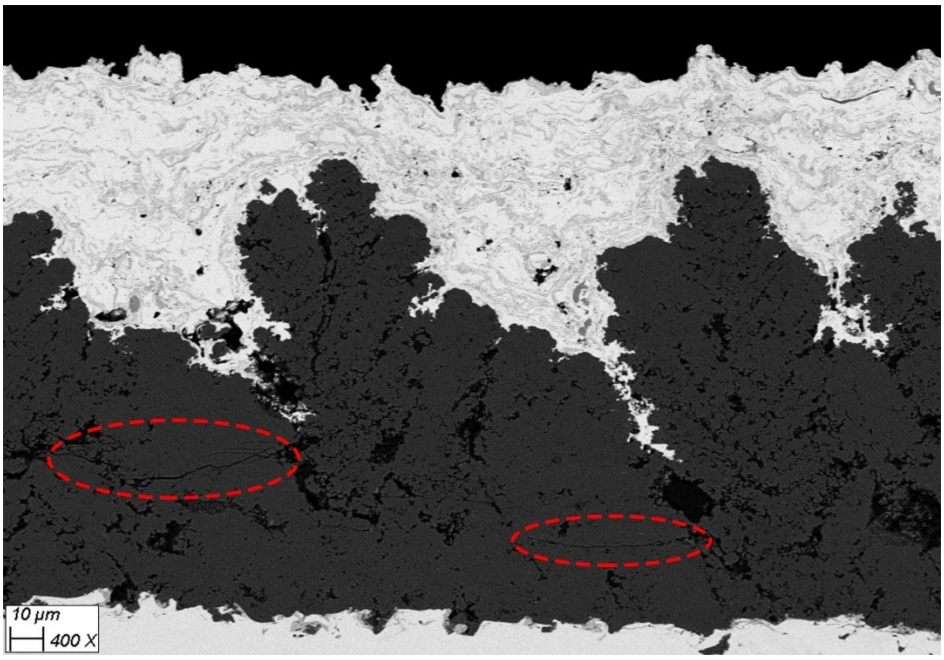

Figure 4-19 Backscattered SEM images of coating systems composed of the heating element layer and SPS (3) with a dense structure [109].

4.2.3. FS Al_2O_3 – APS Ni-20Cr

Figure 4-20 represents the interface between FS (2) alumina and the APS-sprayed heating layer. Similar to the FS (1) Al_2O_3 - w/FS Ni-20Cr system, open pores at the top surface of the alumina coating resulted in penetration of the Ni-20Cr layer into the interconnected pores within the dielectric coating. More penetration was observed in the FS (2) alumina with a higher amount of porosity. It should be noted that even though few minor cracks were present within the alumina layer and the alumina-Ni-20Cr interface, no delamination was observed between the deposited layers.

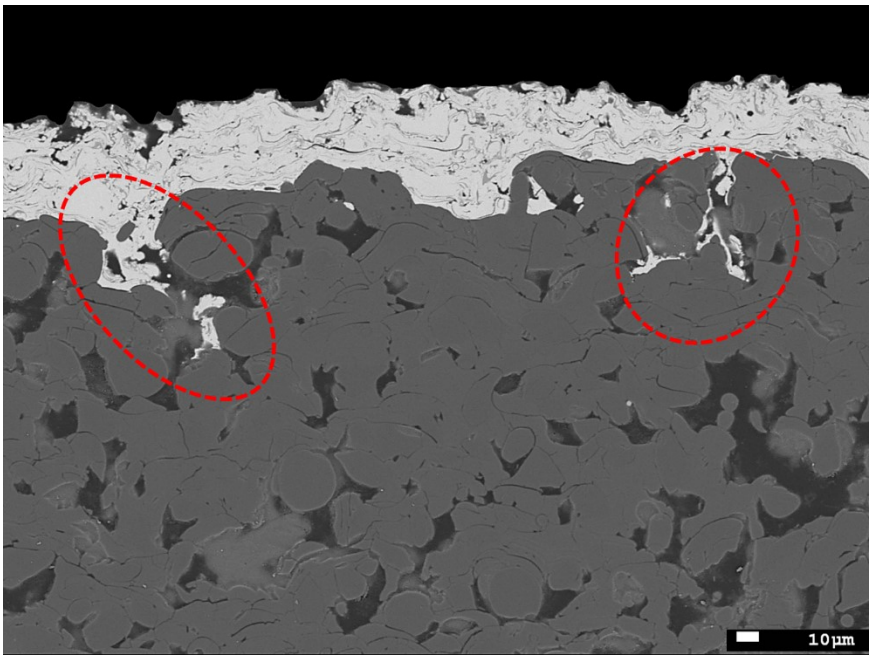

Figure 4-20 Backscattered SEM image of the cross section of the coating system composed of FS (2) alumina and APS Ni-20Cr and the penetration of the top layer into the alumina layer.

4.2.4. SPS Al_2O_3 – APS Ni-20Cr

Figure 4-21(a) represents the microstructure obtained from SPS (1) alumina – APS Ni-20Cr cross section. The porous structure of the SPS (1) alumina resulted in a poor cohesion which is evidenced by the formation of cracks near the alumina-Ni-20Cr interface (Fig. 4-21 (a)). APS-sprayed Ni-20Cr did not fully adhere to the SPS (1) alumina. This detachment could be because of two main reasons. First, the porous nature of the SPS (1) alumina that leads to a microstructure with low toughness; second, the presence of resolidified particles at the surface of the alumina layer as shown in Fig. (4-21 (b)). Conversely, this detachment was not observed in the SPS (2) alumina – Ni-20Cr heating systems (Fig. 4-5).

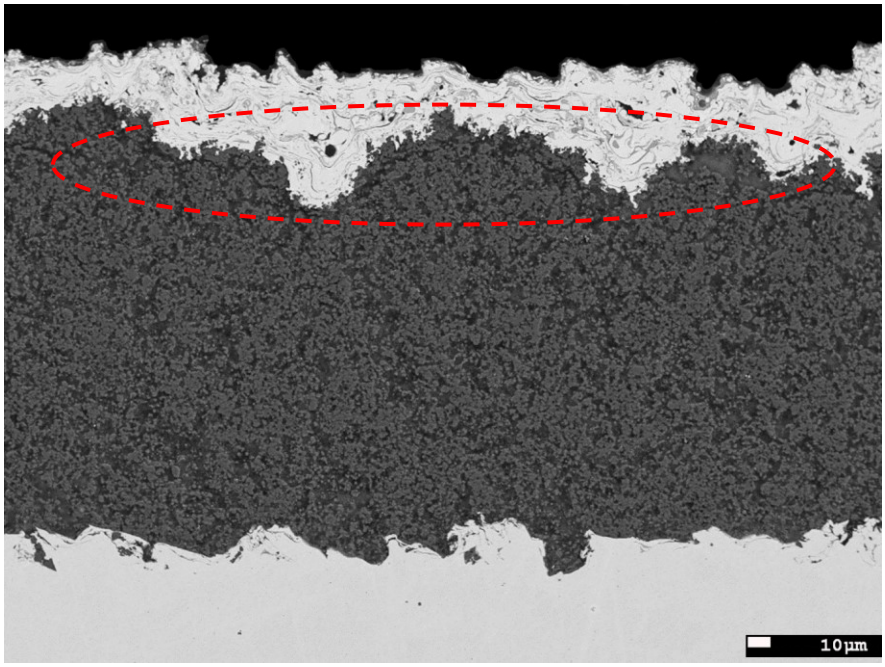

(a)

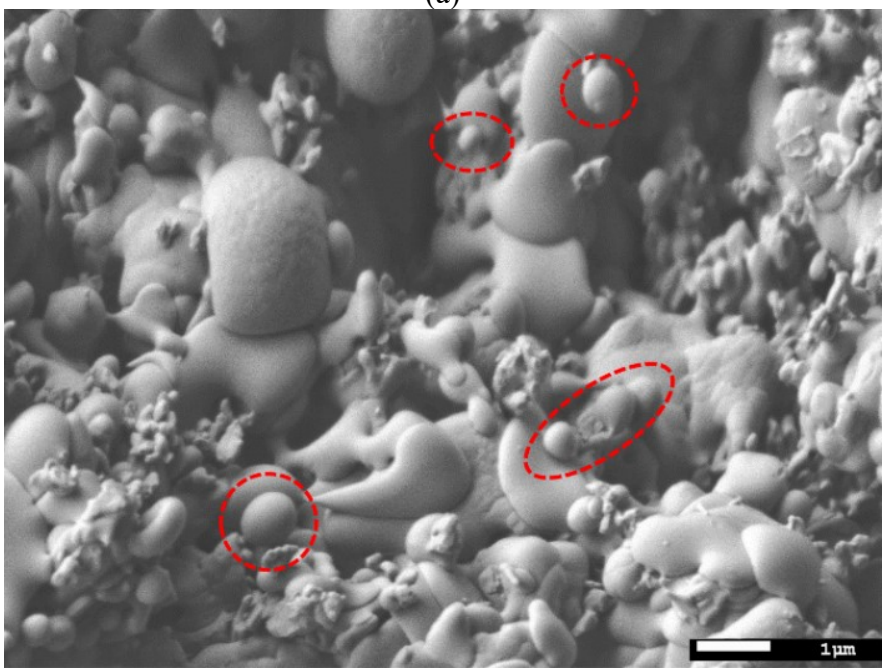

(b)

Figure 4-21 (a) Backscattered SEM image of SPS (1) alumina – APS Ni-20Cr, and (b) secondary SEM image of the top view of the SPS (1) alumina.

4.3. Alternating Current Breakdown Voltage Failure

Breakdown dielectric strength (BDS) of the alumina coatings without the top Ni-20Cr layer is reported in Fig. 4-22. SPS (2) had the maximum BDS of 11.6 V_{ac}/µm, while FS (1) had the lowest value of 4.6 V_{ac}/µm. It is well known that the microstructural characteristics of a coating, such as porosity and cracks play a major role in the breakdown voltage values. Presence of cracks and pores can lead to ionization of entrapped gas in high electric fields, which results in an increase in current flow and heating in certain parts of the coating. This phenomenon could be followed by further cracking and catastrophic incidents [118]. The higher BDS observed in SPS (2) sample is most likely due to its low amount porosity compared to the FS samples which leads to lower amount of ionization.

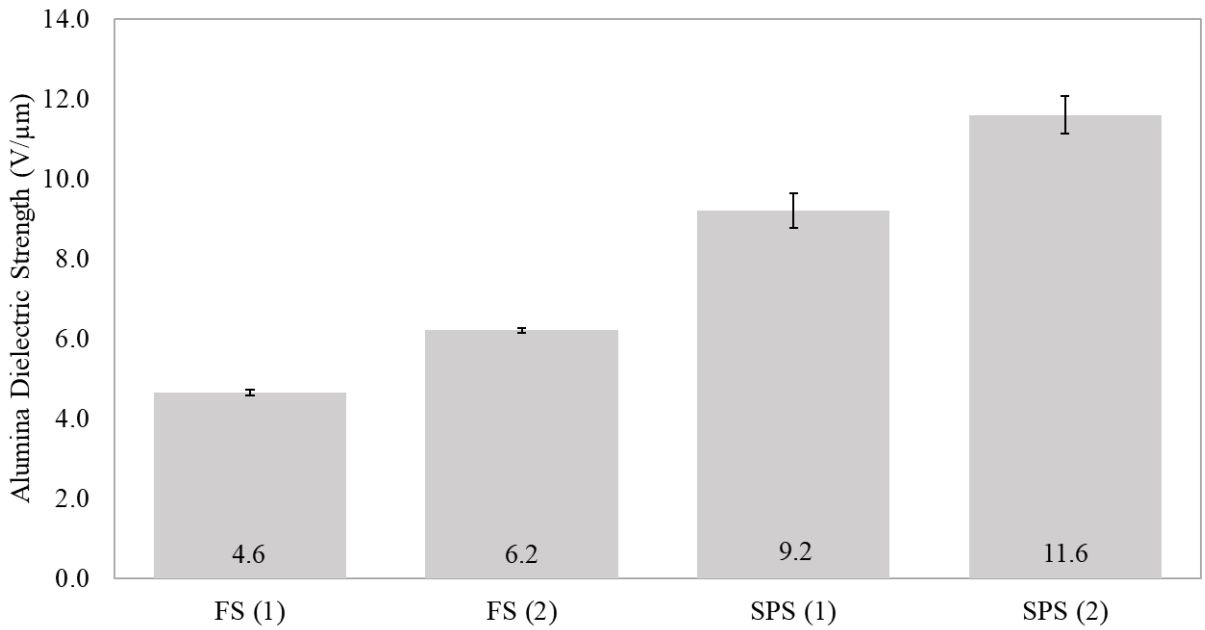

Figure 4-22 Dielectric strength of the alumina coatings without the top Ni-20Cr layer (n = 10).

Considering the dielectric strength values obtained for both FS samples, it should be noted that even though the amount of porosity in FS (1) is higher than FS (2), porosity is not the only factor affecting the dielectric strength values. Phases formed during spraying, the amount of crystalline and amorphous phases distributed throughout the coating are among many other parameters that play a determining role in the final dielectric strength of the alumina coatings.

Dielectric breakdown strength of alumina coatings has been reported in several studies [89,95,96,119–121]. The alternating current (AC) breakdown strength of alumina coating produced by using high velocity oxy-fuel spraying (HVOF) and air plasma spraying (APS), was stated to be 29.2 $V_{ac}/\mu m$ [122] and 13.5-16.5 $V_{ac}/\mu m$ [123], respectively. In both studies the BDS values were obtained in a dry testing condition and the use of insulating oil was prevented. It is well established that numerous parameters affect the final dielectric strength values of alumina coatings and the effect of porosity on the BDS value is not always straightforward. However, when comparing the microstructure of alumina coatings obtained from different spraying processes (HVOF, APS, FS, and SPS); the alumina coating deposited with the HVOF process had the lowest amount of porosity and exhibited the highest BDS value.

Figure 4-23 shows the dielectric strength of the multi-layered heating systems with different alumina dielectric layers. The dielectric strength values shown in Fig. 4-23 are much lower than those presented in Fig. 4-22. This is mainly due to the electrical tipping effect and the penetration of the top Ni-20Cr layer into the alumina layer, reducing its effective thickness. For instance, although FS (2) had a higher amount of alumina dielectric strength compared to FS (1), due to its higher porosity and more penetration of the top heating element into the alumina layer, its overall dielectric strength in the multi-layered heating system was lower. This phenomenon is

indicated where the two FS alumina samples have opposite dielectric behaviors depending on their configuration.

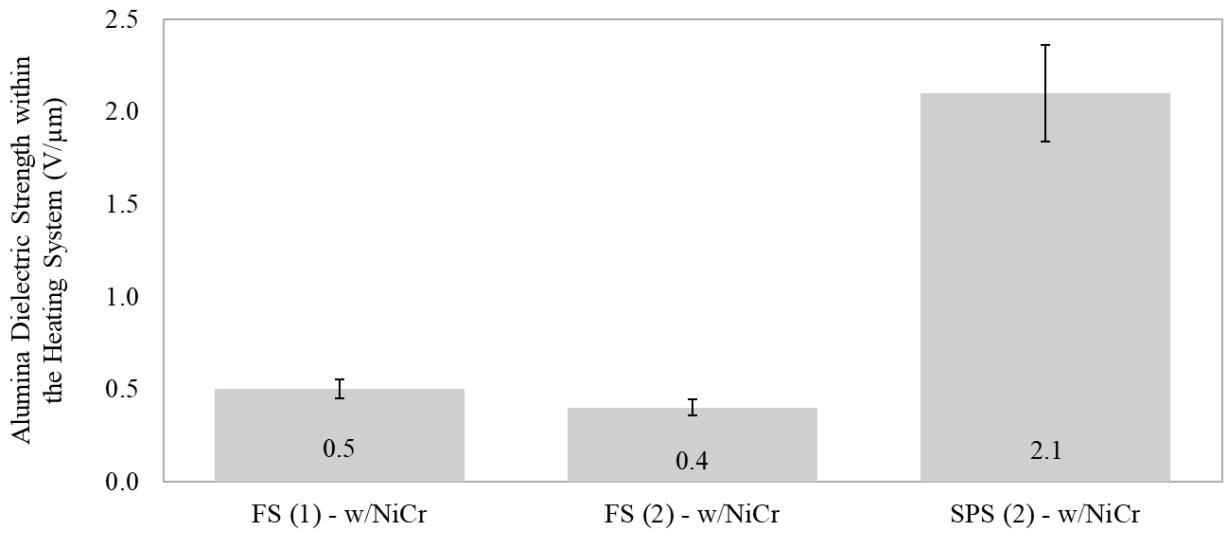

Figure 4-23 Dielectric strength of multi-layered heating systems with different types of alumina as its intermediary dielectric layer.

Measuring the effective thickness of the alumina layer after the deposition of the conductive heating element was not a non-trivial task because the degree of penetration of the top Ni-20Cr into the alumina layer cannot be predicted for the whole coating system. Having said that, a mean value was taken from the Ni-20Cr diffusion lengths into the dielectric layer observed in the SEM images. The mean value was then deducted from the initial reported alumina thickness to obtain the actual effective thickness as precise as possible.

It should be noted that the SPS (2) Al_2O_3 – APS Ni-20Cr with a lower thickness compared to the other two deposited coating systems, exhibited a higher dielectric strength of 2.1 V_{ac}/µm which could mainly be due to its microstructural configuration. The detailed values measured from the alternating current breakdown voltage test, their corresponding dielectric strength values based on coating thickness, and the standard error are presented in Table 4-2. It should be noted that one

possible reason to the higher deviation in breakdown data obtained for the SPS alumina coatings is its lower thickness compared to the FS alumina.

Table 4-2 Measured breakdown voltage values and their corresponding dielectric strengths.

Sample Name	Breakdown Voltage (V_{ac})	Ave. Thickness (μm)	Dielectric Strength (V_{ac}/μm)	Standard Error
FS (1) Al_2O_3	1500	325	4.6	0.08
FS (2) Al_2O_3	2260	364	6.2	0.06
SPS (1) Al_2O_3	1480	160	9.2	0.43
SPS (2) Al_2O_3	1020	87	11.6	0.47
FS (1) Al_2O_3 - w/Ni-20Cr	145	308	0.5	0.05
FS (2) Al_2O_3 - w/Ni-20Cr	118	310	0.4	0.04
SPS (2) Al_2O_3 - w/Ni-20Cr	163	77	2.1	0.26

Chapter 5. Conclusions and Future Work

5.1. Conclusions

In this study, flame spraying and suspension plasma spraying processes were employed to fabricate several alumina dielectric layers. The microstructure characteristics of the prepared samples were investigated by using scanning electron microscopy (SEM) and energy-dispersive X-ray spectroscopy (EDX). The phase composition and adhesion strength of the obtained coatings were examined by X-ray diffraction (XRD) analysis, Raman spectroscopy, and PosiTest pull test. The fabricated alumina layers were then coated with a Ni-20Cr heating layer by using high velocity oxy-fuel and air plasma spraying processes to form a multi-layered heating system. The alternating breakdown voltage test was performed on the produced single-layered alumina samples and the heating systems to compare the dielectric strength values of the alumina coatings.

In FS-sprayed alumina, relatively large pores were observed that were unevenly dispersed throughout the coatings. These open pores were not superficial and were also observed in the cross-sectional images. After the deposition of the Ni-20Cr heating layer, penetration of the top layer into these open pores decreased the effective thickness of the dielectric layer. This phenomenon was considered beneficial from a mechanical perspective as it strengthened the interlocking between the alumina dielectric layer and the heating element. SPS alumina samples exhibited

various microstructures, namely, dense, cauliflower-like, and porous. Unlike the FS process, the porosity observed within the SPS-sprayed alumina samples was uniformly distributed through the coating. Penetration of the top heating layer into the alumina layer was not observed. Furthermore, adhesion tensile strength values of the FS alumina samples were reported to be in the order of ~40 MPa, while the average value reported for the SPS alumina was ~25 MPa.

During the FS process, about 40% of the initial alpha phase of the alumina powder feedstock was transformed into the unstable gamma phase. During the FS process particles mainly go through partial melting that leads to the phase transformation in the outer parts of the particle. It was reported that 60% of the initial alpha phase was retained at the center of most particles. Depending on the SPS spraying conditions, different phase combinations were observed. In the porous SPS-sprayed alumina, the highest amount of stable alpha alumina was observed which was most like due to the presence of unmelted particles or resolified particles during the SPS process. In the dense SPS-sprayed alumina structure, about 70% of the initial powder phase was converted to gamma phase that complete melting of the powder particles could be one possible reason for this statement.

Dielectric breakdown voltage values of the single-layered alumina layers were significantly higher compared to that of the alumina layer within the multi-layered heating system. This observation was reported to be mainly due to the penetration of the top heating element that could have affected the efficiency of the dielectric layer. Many parameters seemed to have influenced the reported dielectric strength values including size of pores and the amount of complete porosity.

Overall, considering the above-mentioned findings, both FS- and SPS-sprayed alumina coatings seemed to have their own advantages. FS-sprayed alumina exhibited a better adhesion strength compared to the SPS-sprayed alumina. On the contrary, SPS-sprayed alumina had a better performance in terms of dielectric properties. From the obtained dielectric breakdown voltage values, it can be concluded that the microstructure of the dielectric layer plays a crucial role on the breakdown voltage values. One of the main challenges associated with the deposition of the Ni-20Cr coating onto the FS alumina was the penetration of the heating layer into the insulating layer. The degree of penetration of the heating layer into the alumina layer was a lot less in the SPS alumina – Ni-20Cr systems proving that SPS alumina did not have open pores as deep as the FS alumina.

Moreover, the feasibility of producing cauliflower-like microstructures by using the SPS process was indicated in this study. Even though further mechanical testing is required to determine the superior strain tolerance of this type of microstructure, given the cauliflower-like nature of the SPS alumina layer, a more strain tolerant behavior is expected that would be favorable to the reliability of heating system.

5.2. Future Works

This research has contributed to the design and fabrication of multi-layered coating-based heating systems. However, further investigations are required to obtain a fully functional and economically optimized heating system. Further research in this area can be extended in the following areas:

- The brittle nature of the alumina dielectric layer has made its application with the heating system challenging. It is recommended to measure the mechanical properties of the alumina samples by

performing pull test and four-point bending test to examine the behavior of the deposited coatings exposed to different types of stress.

- As it was shown in the fourth chapter, suspension plasma spraying can result in several microstructures. It is well-known that the possibility of acquiring a columnar structure is one of the greatest advantages of the SPS process among other thermal spraying methods. This type of microstructure is strain tolerant and can be beneficial for application where the material is exposed to tensile and compression stresses. To obtain this advantageous microstructure, it is recommended to expand the microstructure analysis and to further experiment other spraying techniques, spraying conditions, and suspension concentrations.

- As it was reported in the second chapter, dielectric strength of a material is significantly influenced by measurement conditions (humidity, temperature, etc.), sample size, and flaws within the ceramic. It is recommended to study the effect of these parameters on the dielectric properties of thermally sprayed alumina samples to obtain a better understanding of the electrical reliability of the fabricated samples during application.

- The economic feasibility and improved performance of the developed coating system are two important factors that determine whether the system is suitable for large-scale industrial applications or not. Therefore, it is recommended to improve and optimize the fabrication process in such a way to reduce the labor costs, material waste, and production time as much as possible. In a similar study done by Rezvani Rad, *et al.* [124] the economic feasibility of using thermal-sprayed heating systems for temperature control in steel pipes was investigated.

- Conducting a detailed life cycle analysis (LCA) is necessary to take into consideration all the environment and technical factors of the fabrication process. LCA is known to be a powerful tool that can evaluate and quantify the environmental and technical impacts of the process.

Chapter 6. References

[1] J.R. Davis, Introduction to Thermal Spray Processing, as published in Handbook of Thermal Spray Technology, p 3-13, ASM International and the Thermal Spray Society. (2004).

[2] R.C. Tucker Jr, ASM Handbook, Volume 5A, Thermal Spray Technology, Plastics Industry. 335 (2013) 336.

[3] R.C.T. Jr, Thermal Spray Coatings, 13.

[4] R.E. Melchers, The effect of corrosion on the structural reliability of steel offshore structures, Corrosion Science. 47 (2005) 2391–2410. https://doi.org/10.1016/j.corsci.2005.04.004.

[5] J. Kameda, T.E. Bloomer, Y. Sugita, A. Ito, S. Sakurai, High temperature environmental attack and mechanical degradation of coatings in gas turbine blades, Materials Science and Engineering: A. 229 (1997) 42–54. https://doi.org/10.1016/S0921-5093(97)00003-8.

[6] D. Tejero-Martin, M. Rezvani Rad, A. McDonald, T. Hussain, Beyond Traditional Coatings: A Review on Thermal-Sprayed Functional and Smart Coatings, J Therm Spray Tech. 28 (2019) 598–644. https://doi.org/10.1007/s11666-019-00857-1.

[7] S.F. Bonabi, F. Ashrafizadeh, A. Sanati, S.M. Nahvi, Structure and Corrosion Behavior of Arc-Sprayed Zn-Al Coatings on Ductile Iron Substrate, J Therm Spray Tech. 27 (2018) 524–537. https://doi.org/10.1007/s11666-018-0694-2.

[8] V. Bolleddu, V. Racherla, P.P. Bandyopadhyay, Characterization of air plasma-sprayed yttria-stabilized zirconia coatings deposited with nitrogen, Int J Adv Manuf Technol. 90 (2017) 3437–3449. https://doi.org/10.1007/s00170-016-9613-1.

[9] M. Aghasibeig, Engineered Thermally Sprayed Electrodes for Hydrogen Production by Alkaline Water Electrolysis, phd, Concordia University, 2015. https://spectrum.library.concordia.ca/980789/ (accessed April 13, 2020).

[10] C.R. Lima, N.F. de Souza, F. Camargo, Study of wear and corrosion performance of thermal sprayed engineering polymers, Surface and Coatings Technology. 220 (2013) 140–143.

[11] P. Fauchais, A. Vardelle, H. Jazi, Advanced Plasma Spray Applications, Adv. Plasma Spray Appl., InTech. (2012) 149–188.

[12] G. Mauer, M.O. Jarligo, D.E. Mack, R. Vaßen, Plasma-sprayed thermal barrier coatings: new materials, processing issues, and solutions, Journal of Thermal Spray Technology. 22 (2013) 646–658.

[13] L. Sun, C.C. Berndt, K.A. Gross, A. Kucuk, Material fundamentals and clinical performance of plasma-sprayed hydroxyapatite coatings: A review, Journal of Biomedical Materials Research: An Official Journal of The Society for Biomaterials, The Japanese Society for Biomaterials, and The Australian Society for Biomaterials and the Korean Society for Biomaterials. 58 (2001) 570–592.

[14] S. Sampath, Thermal spray applications in electronics and sensors: past, present, and future, Journal of Thermal Spray Technology. 19 (2010) 921–949.

[15] S. Wilson, S. Metco, Abradable Thermal Spray Applications and Technology, ASM Handbook. 5 (2013) 287–295.

[16] S. Armada, R. Schmid, H. Johnsen, N. Espallargas, 8 - Functionalized thermal spray coatings, in: N. Espallargas (Ed.), Future Development of Thermal Spray Coatings, Woodhead Publishing, 2015: pp. 207–228. https://doi.org/10.1016/B978-0-85709-769-9.00008-7.

[17] M.F. Montemor, Functional and smart coatings for corrosion protection: A review of recent advances, Surface and Coatings Technology. 258 (2014) 17–37. https://doi.org/10.1016/j.surfcoat.2014.06.031.

[18] K. Yakut, B. Sahin, The effects of vortex characteristics on performance of coiled wire turbulators used for heat transfer augmentation, Applied Thermal Engineering. 24 (2004) 2427–2438. https://doi.org/10.1016/j.applthermaleng.2004.03.008.

[19] J.-M. Lamarre, P. Marcoux, M. Perrault, R.C. Abbott, J.-G. Legoux, Performance Analysis and Modeling of Thermally Sprayed Resistive Heaters, J Therm Spray Tech. 22 (2013) 947–953. https://doi.org/10.1007/s11666-013-9946-3.

[20] M. Prudenziati, Development and the implementation of high-temperature reliable heaters in plasma spray technology, 2008. https://doi.org/10.1007/s11666-008-9164-6.

[21] A. Lopera-Valle, A. McDonald, Application of flame-sprayed coatings as heating elements for polymer-based composite structures, Journal of Thermal Spray Technology. 24 (2015) 1289–1301.

[22] M. Floristán, A. Killinger, R.G.-K.E. Materials, undefined 2013, Overview on developed functional plasma sprayed coatings on glass and glass ceramic substrates, Trans Tech Publ. https://www.scientific.net/KEM.533.115.

[23] A. von Meier, Electric Power Systems: A Conceptual Introduction, John Wiley & Sons, 2006.

[24] Y.V. Deshmukh, Industrial Heating: Principles, Techniques, Materials, Applications, and Design, CRC Press, 2005.

[25] M.L. Nayyar, HEAT-TRACING OF PIPING SYSTEMS, McGraw-Hill Education: New York, Chicago, San Francisco, Athens, London, Madrid, Mexico City, Milan, New Delhi, Singapore, Sydney, Toronto, 2000. /content/book/9780070471061/chapter/chapter17 (accessed May 16, 2020).

[26] Panel discussion on electrical heat tracing - IEEE Conference Publication, . https://ieeexplore.ieee.org/abstract/document/787437 (accessed May 16, 2020).

[27] V.F. Petrenko, C.R. Sullivan, V. Kozlyuk, Variable-resistance conductors (VRC) for power-line de-icing, Cold Regions Science and Technology. 65 (2011) 23–28. https://doi.org/10.1016/j.coldregions.2010.06.003.

[28] A.G. Mohammed, G. Ozgur, E. Sevkat, Electrical resistance heating for deicing and snow melting applications: Experimental study, Cold Regions Science and Technology. 160 (2019) 128–138. https://doi.org/10.1016/j.coldregions.2019.02.004.

[29] O. Parent, A. Ilinca, Anti-icing and de-icing techniques for wind turbines: Critical review, Cold Regions Science and Technology. 65 (2011) 88–96. https://doi.org/10.1016/j.coldregions.2010.01.005.

[30] C. Mayer, A. Ilinca, G. Fortin, J. Perron, Wind tunnel study of electro-thermal de-icing of wind turbine blades, International Journal of Offshore and Polar Engineering. 17 (2007).

[31] H.F. Younis, R.S. Dahbura, J.H.V. Lienhard, Thin Film Resistance Heaters for High Heat Flux Jet-Array Cooling Experiments, ASME-PUBLICATIONS-HTD. 353 (1997) 127–134.

[32] D. Michels, J. Hadeler, J.H. Lienhard, High-heat-flux resistance heaters from vps and hvof thermal spraying, Experimental Heat Transfer. 11 (1998) 341–359. https://doi.org/10.1080/08916159808946570.

[33] A. Killinger, R. Gadow, Thermally sprayed coating composites for film heating devices, in: Advances in Science and Technology, Trans Tech Publ, 2006: pp. 1230–1239.

[34] M. Floristán, R. Fontarnau, A.K.-S. \ldots, Coatings, undefined 2010, Development of electrically conductive plasma sprayed coatings on glass ceramic substrates, Elsevier. https://www.sciencedirect.com/science/article/pii/S025789721000397X.

[35] P. Fauchais, M. Vardelle, A. Vardelle, L. Bianchi, Plasma spray: study of the coating generation, Ceramics International. 22 (1996) 295–303.

[36] P. Fauchais, Understanding plasma spraying, Journal of Physics D: Applied Physics. 37 (2004) R86.

[37] P.L. Fauchais, J.V. Heberlein, M.I. Boulos, Thermal spray fundamentals: from powder to part, Springer Science & Business Media, 2014.

[38] N. Sharifi, Developing Superhydrophobic Coatings for Mitigating Aircraft Icing using Plasma Spray Processes, phd, Concordia University, 2018. https://spectrum.library.concordia.ca/983636/ (accessed May 17, 2020).

[39] P. Fauchais, R. Etchart-Salas, V. Rat, J.F. Coudert, N. Caron, K. Wittmann-Ténèze, Parameters controlling liquid plasma spraying: Solutions, sols, or suspensions, 2008. https://doi.org/10.1007/s11666-007-9152-2.

[40] P. Fauchais, R. Etchart-Salas, C. Delbos, M. Tognonvi, V. Rat, J.-F. Coudert, T. Chartier, Suspension and solution plasma spraying of finely structured layers: potential application to SOFCs, Journal of Physics D: Applied Physics. 40 (2007) 2394.

[41] L. Pawlowski, Suspension and solution thermal spray coatings, Surface and Coatings Technology. 203 (2009) 2807–2829. https://doi.org/10.1016/j.surfcoat.2009.03.005.

[42] K. VanEvery, M.J.M. Krane, R.W. Trice, H. Wang, W. Porter, M. Besser, D. Sordelet, J. Ilavsky, J. Almer, Column Formation in Suspension Plasma-Sprayed Coatings and Resultant Thermal Properties, J Therm Spray Tech. 20 (2011) 817–828. https://doi.org/10.1007/s11666-011-9632-2.

[43] T. Strangman, D. Raybould, A. Jameel, W. Baker, Damage mechanisms, life prediction, and development of EB-PVD thermal barrier coatings for turbine airfoils, Surface and Coatings Technology. 202 (2007) 658–664. https://doi.org/10.1016/j.surfcoat.2007.06.067.

[44] X. Chen, T. Ohnuki, S. Kuroda, M. Gizynski, H. Araki, H. Murakami, M. Watanabe, Y. Sakka, Columnar and DVC-structured thermal barrier coatings deposited by suspension plasma spray: high-temperature stability and their corrosion resistance to the molten salt, Ceramics International. 42 (2016) 16822–16832. https://doi.org/10.1016/j.ceramint.2016.07.174.

[45] N. Curry, K. VanEvery, T. Snyder, J. Susnjar, S. Bjorklund, Performance testing of suspension plasma sprayed thermal barrier coatings produced with varied suspension parameters, Coatings. 5 (2015) 338–356.

[46] L. Pawlowski, The science and engineering of thermal spray coatings, John Wiley & Sons, 2008.

[47] S. Siegmann, C. Abert, 100 years of thermal spray: About the inventor Max Ulrich Schoop, Surface and Coatings Technology. 220 (2013) 3–13. https://doi.org/10.1016/j.surfcoat.2012.10.034.

[48] K.E. Schneider, V. Belashchenko, M. Dratwinski, S. Siegmann, A. Zagorski, Thermal spraying for power generation components, John Wiley & Sons, 2006.

[49] M. Oksa, E. Turunen, T. Suhonen, T. Varis, S.-P. Hannula, Optimization and characterization of high velocity oxy-fuel sprayed coatings: techniques, materials, and applications, Coatings. 1 (2011) 17–52.

[50] K.M. Smith Jr, M.P. Van Bree, J.F. Grzetic, Analysis and testing of freezing phenomena in piping systems, in: ASME International Mechanical Engineering Congress and Exposition, 2008: pp. 123–128.

[51] D.B. Edwards, K.M. Smith Jr, D.E. Duvall, J.F. Grzetic, Analysis and Testing of Freezing Phenomena in Plastic Piping Systems, in: ASME International Mechanical Engineering Congress and Exposition, 2009: pp. 201–206.

[52] E. Vine, E. Mills, A. Chen, Energy-efficiency and renewable energy options for risk management and insurance loss reduction, Energy. 25 (2000) 131–147. https://doi.org/10.1016/S0360-5442(99)00068-7.

[53] A. Carrns, Avoiding Costly Home Damage From Winter's Cold, The New York Times. (2014).

[54] J.R. Gordon, An investigation into freezing and bursting water pipes in residential construction, Building Research Council. School of Architecture. College of Fine, 1996.

[55] D.H. Harris, R.J. Janowiecki, C.E. Semler, M.C. Willson, J.T. Cheng, Polycrystalline Ferrite Films for Microwave Applications Deposited by Arc-Plasma, Journal of Applied Physics. 41 (1970) 1348–1349.

[56] R.T. Smyth, J.C. Anderson, Production of resistors by arc plasma spraying, Active and Passive Electronic Components. 2 (1975) 135–145.

[57] S. Sampath, H. Herman, A. Patel, R. Gambino, R. Greenlaw, E. Tormey, Thermal spray techniques for fabrication of meso-electronics and sensors, MRS Online Proceedings Library Archive. 624 (2000).

[58] E. Russegger, Method for the production of an electrically conductive resistive layer and heating and/or cooling device, US7361869B2, 2008. https://patents.google.com/patent/US7361869B2/en (accessed July 16, 2020).

[59] E. Brook-Levinson, V. Manov, Y. Margolin, E. Adar, Y. Sorkine, V. Volchkov, Electrical heating elements and method for producing same, US6596960B1, 2003. https://patents.google.com/patent/US6596960B1/en (accessed July 16, 2020).

[60] T. Tong, J. Li, Q. Chen, J.P. Longtin, S. Tankiewicz, S. Sampath, Ultrafast laser micromachining of thermal sprayed coatings for microheaters: design, fabrication and characterization, Sensors and Actuators A: Physical. 114 (2004) 102–111.

[61] M. Prudenziati, G. Cirri, P. Dal Bo, Novel high-temperature reliable heaters in plasma spray technology, Journal of Thermal Spray Technology. 15 (2006) 329–331.

[62] A. Lopera-Valle, A. McDonald, Flame-sprayed coatings as de-icing elements for fiber-reinforced polymer composite structures: Modeling and experimentation, International Journal of Heat and Mass Transfer. 97 (2016) 56–65.

[63] M. Rezvani Rad, A. McDonald, Development of a Thermal-Sprayed Coating System to Mitigate Ice Accumulation and Freezing Damage in Carbon Steel Pipes, Thermal Spray 2018: Proceedings of the International Thermal Spray Conference, Orlando, FL, USA, 2018, p 635-642.
.

[64] H. Jang, D.N. Seidman, K.L. Merkle, The chemical composition of a metal/ceramic interface on an atomic scale: The Cu/MgO interface, Interface Science. 1 (1993) 61–75.

[65] M. Barsoum, Fundamentals of ceramics, CRC press, 2019.

[66] D.W. Richerson, Modern Ceramic Engineering: Properties, Processing, and Use in Design, Third Edition, CRC Press, 2005.

[67] W.D. Kingery, Introduction to ceramics, (1976).

[68] C.B. Carter, M.G. Norton, Ceramic materials: science and engineering, Springer, 2007.

[69] Oxide Ceramics: Structure, Technology, and Applications, in: Classic and Advanced Ceramics, John Wiley & Sons, Ltd, 2010: pp. 175–252. https://doi.org/10.1002/9783527630172.ch7.

[70] C. Sikalidis, Advances in Ceramics: Synthesis and Characterization, Processing and Specific Applications, BoD – Books on Demand, 2011.

[71] N. Salah, Z.H. Khan, S.S. Habib, Nanoparticles of Al2O3: Cr as a sensitive thermoluminescent material for high exposures of gamma rays irradiations, Nuclear Instruments and Methods in Physics Research Section B: Beam Interactions with Materials and Atoms. 269 (2011) 401–404.

[72] C. Sallé, F. Ferey, P. Grosseau, B. Guilhot, P. Iacconi, M. Benabdesselam, G. Fantozzi, Detection of foreign phases in doped a-alumina powders by thermoluminescence, Journal of Thermal Analysis and Calorimetry. 73 (2003) 25–33.

[73] W.H. Gitzen, Alumina as a ceramic material, (1970). http://inis.iaea.org/Search/search.aspx?orig_q=RN:1002574 (accessed May 9, 2020).

[74] Diamond impregnated tools-uses and production - Search results - Pascal and Francis Bibliographic Databases, .https://pascal-francis.inist.fr/vibad/index.php?action=getRecordDetail&idt=3826115 (accessed May 9, 2020).

[75] Manufacture and properties of ceramic cutting tools: a review: Materials Science and Technology: Vol 3, No 11, (accessed May 9, 2020).

[76] P. Bowen, C. Carry, D. Luxembourg, H. Hofmann, Colloidal processing and sintering of nanosized transition aluminas, Powder Technology. 157 (2005) 100–107. https://doi.org/10.1016/j.powtec.2005.05.015.

[77] K. Wefers, C. Misra, Oxides and hydroxides of aluminum. alcoa technical paper No. 19, Alum. Co. Am. 92 (1987).

[78] Y. Yoshizawa, K. Hirao, S. Kanzaki, Fabrication of low cost fine-grained alumina powders by seeding for high performance sintered bodies, Journal of the European Ceramic Society. 24 (2004) 325–330. https://doi.org/10.1016/S0955-2219(03)00226-7.

[79] P. Boch, J.-C. Nièpce, Ceramic Materials: Processes, Properties, and Applications, John Wiley & Sons, 2010.

[80] P. Fulay, J.-K. Lee, Electronic, Magnetic, and Optical Materials, CRC Press, 2016.

[81] X. Hao, Dielectric Ceramics and Films for Electrical Energy Storage, in: Ferroelectric Materials for Energy Applications, John Wiley & Sons, Ltd, 2018: pp. 119–168. https://doi.org/10.1002/9783527807505.ch5.

[82] A. Zeb, S.J. Milne, Stability of High-Temperature Dielectric Properties for (1 − x)Ba0.8Ca0.2TiO3–xBi(Mg0.5Ti0.5)O3 Ceramics, Journal of the American Ceramic Society. 96 (2013) 2887–2892. https://doi.org/10.1111/jace.12412.

[83] R.N.P. Choudhary, S.K. Patri, Dielectric Materials: Introduction, Research and Applications, 129.

[84] R.C. Buchanan, Ceramic Materials for Electronics, Third Edition, CRC Press, 2004.

[85] A.A. Abdel-Samad, A.M.M. El-Bahloul, E. Lugscheider, S.A. Rassoul, Comparative study on thermally sprayed alumina based ceramic coatings, Journal of Materials Science. 35 (2000) 3127–3130. https://doi.org/10.1023/A:1004824104162.

[86] M. Niittymäki, K. Lahti, T. Suhonen, J. Metsäjoki, Dielectric Breakdown Strength of Thermally Sprayed Ceramic Coatings: Effects of Different Test Arrangements, Journal of Thermal Spray Technology. 24 (2015) 542–551. https://doi.org/10.1007/s11666-014-0211-1.

[87] J. Lamarre, C. Cojocaru, J.L.-P. of the I. Thermal, undefined 2014, On the dielectric behavior of annealed plasma sprayed forsterite and alumina coatings.

[88] R. Luo, P. Li, H. Wei, H. Chen, K.Y.-C. International, undefined 2018, Structure and electrical insulation characteristics of plasma-sprayed alumina coatings under pressure, Elsevier. . https://www.sciencedirect.com/science/article/pii/S0272884217329243.

[89] F.L. Toma, S. Scheitz, L.M. Berger, V. Sauchuk, M. Kusnezoff, S. Thiele, Comparative study of the electrical properties and characteristics of thermally sprayed alumina and spinel coatings, in: Journal of Thermal Spray Technology, 2011: pp. 195–204. https://doi.org/10.1007/s11666-010-9580-2.

[90] T. Tesar, R. Musalek, J. Medricky, J. Kotlan, F. Lukac, Z. Pala, P. Ctibor, T. Chraska, S. Houdkova, V. Rimal, N. Curry, Development of suspension plasma sprayed alumina coatings with high enthalpy plasma torch, Surface and Coatings Technology. 325 (2017) 277–288. https://doi.org/10.1016/j.surfcoat.2017.06.039.

[91] P. Müller, A. Killinger, R. Gadow, Comparison Between High-Velocity Suspension Flame Spraying and Suspension Plasma Spraying of Alumina, J Therm Spray Tech. 21 (2012) 1120–1127. https://doi.org/10.1007/s11666-012-9783-9.

[92] B.-D. Yan, S. Meilink, G. Warren, P. Wynblatt, Water adsorption and surface conductivity measurements on alpha-alumina substrates, IEEE Transactions on Components, Hybrids, and Manufacturing Technology. 10 (1987) 247–251.

[93] F.L. Toma, L.M. Berger, S. Scheitz, S. Langner, C. Rödel, A. Potthoff, V. Sauchuk, M. Kusnezoff, Comparison of the microstructural characteristics and electrical properties of thermally sprayed Al 2O 3 coatings from aqueous suspensions and feedstock powders, in: Journal of Thermal Spray Technology, Springer, 2012: pp. 480–488. https://doi.org/10.1007/s11666-012-9761-2.

[94] C.C. Stahr, S. Saaro, L.-M. Berger, J. Dubský, K. Neufuss, M. Herrmann, Dependence of the Stabilization of α-Alumina on the Spray Process, J Therm Spray Tech. 16 (2007) 822–830. https://doi.org/10.1007/s11666-007-9107-7.

[95] L. Pawlowski, The relationship between structure and dielectric properties in plasma-sprayed alumina coatings, Surface and Coatings Technology. 35 (1988) 285–298. https://doi.org/10.1016/0257-8972(88)90042-4.

[96] M. Niittymaki, K. Lahti, T. Suhonen, J. Metsajoki, Effect of temperature and humidity on dielectric properties of thermally sprayed alumina coatings, IEEE Transactions on Dielectrics and Electrical Insulation. 25 (2018) 908–918. https://doi.org/10.1109/TDEI.2018.006892.

[97] X. Lu, J. Yang, X. Li, F. Sun, F. Wang, Y. Chao, Effects of phase transformation on properties of alumina ceramic membrane: A new assessment based on quantitative X-ray diffraction (QXRD), Chemical Engineering Science. 199 (2019) 349–358. https://doi.org/10.1016/j.ces.2018.12.054.

[98] R. McPherson, Formation of metastable phases in flame- and plasma-prepared alumina, Journal of Materials Science. 8 (1973) 851–858. https://doi.org/10.1007/BF02397914.

[99] J. Kotlan, R.C. Seshadri, S. Sampath, P. Ctibor, Z. Pala, R. Musalek, On the dielectric strengths of atmospheric plasma sprayed Al2O3, Y2O3, ZrO2–7% Y2O3 and (Ba,Sr)TiO3 coatings, Ceramics International. 41 (2015) 11169–11176. https://doi.org/10.1016/j.ceramint.2015.05.066.

[100] N. Branland, E. Meillot, P. Fauchais, A. Vardelle, F. Gitzhofer, M. Boulos, Relationships between microstructure and electrical properties of RF and DC plasma-sprayed titania coatings, 2006. https://doi.org/10.1361/105996306X92596.

[101] M. Plummer, The formation of metastable aluminas at high temperatures, Journal of Applied Chemistry. 8 (1958) 35–44.

[102] J. Gao, X. Xiong, Y. Gao, The effect of the α/γ phase on the dielectric properties of plasma sprayed Al2O3 coatings, Journal of Materials Science: Materials in Electronics. 28 (2017) 12015–12020. https://doi.org/10.1007/s10854-017-7011-6.

[103] P. Fauchais, M. Fukumoto, A. Vardelle, M. Vardelle, Knowledge Concerning Splat Formation: An Invited Review, . https://doi.org/10.1361/10599630419670.

[104] Praxair Surface Technologies Inc., Powder Solutions Catalog, Indianapolis, 2014, p. 17. (accessed June 8, 2020).

[105] Oerlikon Metco, Material Product Data Sheet: DSMTS-0005.6 – Aluminum Oxide Thermal Spray Powders, Oerlikon Metco, Westbury, 2017, p. 1. (accessed June 8, 2020).

[106] M. Rezvani Rad, M. Mohammadian Bajgiran, C. Moreau, A. McDonald, Fabrication of thermally sprayed coating systems for mitigation of ice accumulation in carbon steel pipes and prevention of pipe bursting, Surface and Coatings Technology. 397 (2020) 126013. https://doi.org/10.1016/j.surfcoat.2020.126013.

[107] PosiTest Manual Adhesion Tester by DeFelsko, DEFELSKO Inspection Instruments. . https://www.defelsko.com/positest-at (accessed July 3, 2020).

[108] Adhesion Testers - PosiTest AT Series | DeFelsko, . https://www.defelsko.com/positest (accessed June 28, 2020).

[109] M.M. Bajgiran, C. Moreau, M.R. Rad, A. Mcdonald, On Reliability of Thermally-Sprayed Alumina Dielectric Layers in a Multi- layered Coating-based Heating System, in: Proceedings of the Canadian Society for Mechanical Engineering International Congress 2018, June 2-5, 2019 London, ON, Canada, 2019: pp. 1–7.

[110] P. Auerkari, Mechanical and physical properties of engineering alumina ceramics, Technical Research Centre of Finland Espoo, 1996.

[111] A. Aminzadeh, H. Sarikhani-fard, Raman spectroscopic study of Ni/Al2O3 catalyst, Spectrochimica Acta Part A: Molecular and Biomolecular Spectroscopy. 55 (1999) 1421–1425. https://doi.org/10.1016/S1386-1425(98)00312-6.

[112] A. Mortensen, D.H. Christensen, O.F. Nielsen, E. Pedersen, Raman spectra of amorphous Al2O3 and Al2O3/MoO3 obtained by visible and infrared excitation, Journal of Raman Spectroscopy. 22 (1991) 47–49. https://doi.org/10.1002/jrs.1250220109.

[113] S. Cava, S.M. Tebcherani, I.A. Souza, S.A. Pianaro, C.A. Paskocimas, E. Longo, J.A. Varela, Structural characterization of phase transition of Al 2 O 3 nanopowders obtained by polymeric precursor method, Materials Chemistry and Physics. 103 (2007) 394–399. https://doi.org/10.1016/j.matchemphys.2007.02.046.

[114] S. Vural, Ö. Sari, Synthesis and characterization of SDS assistant α-alumina structures and investigation of the effect of the calcination time on the morphology, Colloid Polym Sci. 297 (2019) 107–114. https://doi.org/10.1007/s00396-018-4442-4.

[115] S.P.S. Porto, R.S. Krishnan, Raman effect of corundum, The Journal of Chemical Physics. 47 (1967) 1009–1012. https://doi.org/10.1063/1.1711980.

[116] G. Pezzotti, W. Zhu, Resolving stress tensor components in space from polarized Raman spectra: polycrystalline alumina, Physical Chemistry Chemical Physics. 17 (2015) 2608–2627. https://doi.org/10.1039/C4CP04244A.

[117] S. Lamouri, M. Hamidouche, N. Bouaouadja, H. Belhouchet, V. Garnier, G. Fantozzi, J.F. Trelkat, Control of the γ-alumina to α-alumina phase transformation for an optimized alumina densification, Boletín de La Sociedad Española de Cerámica y Vidrio. 56 (2017) 47–54. https://doi.org/10.1016/j.bsecv.2016.10.001.

[118] H. Kim, T. Troczynski, Thick alumina dielectric films on aluminum through chemically bonded composite sol-gel, Ceramics International. 33 (2007) 333–336. https://doi.org/10.1016/j.ceramint.2005.09.019.

[119] M. Niittymaki, K. Lahti, T. Suhonen, J. Metsajoki, Electric field dependency of dielectric behavior of thermally sprayed ceramic coatings, in: Proceedings of the IEEE International Conference on Properties and Applications of Dielectric Materials, Institute of Electrical and Electronics Engineers Inc., 2015: pp. 500–503. https://doi.org/10.1109/ICPADM.2015.7295318.

[120] M. Niittymaki, K. Lahti, T. Suhonen, J. Metsajoki, DC conduction and breakdown behavior of thermally sprayed ceramic coatings, IEEE Transactions on Dielectrics and Electrical Insulation. 24 (2017) 499–510. https://doi.org/10.1109/TDEI.2016.006156.

[121] J. Kitamura, H. Ibe, F. Yuasa, H. Mizuno, Plasma sprayed coatings of high-purity ceramics for semiconductor and flat-panel-display production equipment, Journal of Thermal Spray Technology. 17 (2008) 878–886.

[122] M. Niittymäki, K. Lahti, T. Suhonen, J. Metsäjoki, Dielectric Breakdown Strength of Thermally Sprayed Ceramic Coatings: Effects of Different Test Arrangements, Journal of Thermal Spray Technology. 24 (2015) 542–551. https://doi.org/10.1007/s11666-014-0211-1.

[123] J. Kotlan, R.C. Seshadri, S. Sampath, P. Ctibor, Z. Pala, R. Musalek, On the dielectric strengths of atmospheric plasma sprayed Al2O3, Y2O3, ZrO2–7% Y2O3 and (Ba,Sr)TiO3 coatings, Ceramics International. 41 (2015) 11169–11176. https://doi.org/10.1016/j.ceramint.2015.05.066.

[124] M. Rezvani Rad, Techno-Economic Assessment of Coating-Based Resistive Heating Systems versus Conventional Heat Tracers, in: Asm, 2019. https://asm.confex.com/asm/itsc19/webprogram/Paper47224.html (accessed August 2, 2020).